Construction of a cryo-super-resolution microscope to guide *in situ* structure analysis

by

Jakob Vorlaufer

August, 2025

A thesis submitted to the
Graduate School
of the
Institute of Science and Technology Austria
in partial fulfillment of the requirements
for the degree of
Doctor of Philosophy

Committee in charge:
Georgios Katsaros, Chair
Johann G. Danzl
Florian K. M. Schur
Joerg Bewersdorf

The thesis of Jakob Vorlaufer, titled *Construction of a cryo-super-resolution microscope to guide in situ structure analysis*, is approved by:

Supervisor: Johann Danzl, ISTA, Klosterneuburg, Austria

Signature: _____

Committee Member: Florian Schur, ISTA, Klosterneuburg, Austria

Signature: _____

Committee Member: Joerg Bewersdorf, Yale School of Medicine, New Haven, Conneticut, USA

Signature: _____

Defense Chair: Georgios Katsaros, ISTA, Klosterneuburg, Austria

Signature: _____

Signed page is on file

ISTA Thesis, ISSN: 2663-337X

I hereby declare that this thesis is my own work and that it does not contain other people's work without this being so stated; this thesis does not contain my previous work without this being stated, and the bibliography contains all the literature that I used in writing the dissertation.

I accept full responsibility for the content and factual accuracy of this work, including the data and their analysis and presentation, and the text and citation of other work.

I declare that this is a true copy of my thesis, including any final revisions, as approved by my thesis committee, and that this thesis has not been submitted for a higher degree to any other university or institution.

I certify that any republication of materials presented in this thesis has been approved by the relevant publishers and co-authors.

Signature: _____

Jakob Vorlaufer, August, 2025

Signed page is on file

Abstract

The internal structure of biomolecules and their organization in higher-order arrangements are key factors governing the working principles of biological systems. Bioimaging has successfully revealed arrangements across relevant spatial scales. For example, cryo-electron tomography has become widely used for analyzing biomolecular structures *in situ* due to its comprehensive structural visualization of near-natively preserved samples, and its capability of sub-nm resolution via averaging. However, the identification of molecules within crowded cellular environments is often hindered by low contrast. Fluorescence microscopy, on the other hand, routinely visualizes specifically labeled targets at single-molecule contrast against essentially zero background. Moreover, it provides comparatively high throughput and is amenable to multiplexing. Due to this complementarity, combining datasets from both modalities acquired on the same region via correlative light and electron microscopy can reveal novel types of information.

The spatial scale at which information can be extracted depends on imaging resolution and correlation accuracy. Since diffraction of light limits the resolution of conventional fluorescence microscopy to few hundreds of nanometers, reaching the full potential of correlative imaging requires super-resolution approaches. Performing imaging at cryogenic temperature preserves structures in a near-native state and minimizes distortions between the fluorescence and the electron microscopy datasets. Implementations of this concept have achieved correlation on the scale of cellular organelles or bacterial domains.

We have worked towards pushing correlative imaging to the single-molecule scale by improving cryo-super-resolution microscopy, and devising a refined image correlation workflow. As part of this project, I constructed a microscopy setup and adopted it for super-resolution fluorescence microscopy at room temperature and cryogenic conditions. I explored different cryo-stages and acquisition strategies. Specifically, I developed a new scheme for correcting sample drift, thus increasing mechanical stability during microscopy acquisitions.

Acknowledgments

I thank Johann Danzl welcoming me to his research group when I was a Bachelor student without prior experimental experience, and providing me with the support that allowed me to develop into an independently operating scientist. I grew through the responsibilities he entrusted me with at an early stage of my PhD, and knowing that he valued my opinion made me more confident in my own judgements. He also supported my professional development, and encouraged me to explore networking opportunities. Collaboratively writing a research article and peer-reviewing manuscripts gave me interesting insights into the scientific publishing process.

Besides being part of my thesis committee, Florian Schur is also a close collaborator. I am grateful for his insights into the cryo-electron tomography workflow, and the implications for our project as well as *in situ* structural biology as a whole. He always took the time to ensure I thoroughly understood novel topics, and at the same time he was excited to discuss my ideas. I want to thank Joerg Bewersdorf for providing important advice and supporting us at shaping the focus of my project as external member of my thesis committee.

I am thankful for highly stimulating interactions with all past and present members of the Danzl group. They got me excited about working in an interdisciplinary environment more than I had anticipated in the beginning. I still find it inspiring how people of different backgrounds can contribute their skills to enrich each other's perspective in thinking about profound topics. Thanks go to Caroline Kreuzinger for organizational support and providing cake on many occasions, as well as critically proofreading the sample preparation protocols of this thesis. Thank you to Ivan Krylov for taking over parts of the project with a great level of excitement and a proactive, organized attitude, as well as critically proofreading the section of this thesis describing operation of the cryostat.

Marek Šuplata's work of developing the core hardware control software was an integral part of my thesis project. I was always impressed how he solved all of the issues I raised, sometimes at unexpected speed, in the process teaching me how to structure software development. I am highly grateful to Wiebke Jahr for showing me the ins and outs of developing microscopes when I joined the Danzl group without prior experience, patiently explaining concepts and demonstrating hands-on procedures in the optics lab, thus helping me grow into an independent researcher. She also developed the software controlling my setup's spatial light modulator. Furthermore, I want to thank Nikolai Semenov for programming the graphical user interface for the active stabilization module, and Andreas Wartak for interesting discussions on optics development.

For sample preparation, I received expert support from many colleagues in the Danzl and Schur labs, notably Caroline Kreuzinger, Nathalie Agudelo Dueñas, Mojtaba R. Tavakoli and Ivan Krylov for stainings performed at room temperature, and Manjunath Javoor (in particular optimizing preparation of *in vitro* polymerized actin), Bettina Zens, Andreas Thader, Ivan Krylov, Jesse Hansen and Kain van den Elsen for plunge-frozen samples. Cryo-electron microscopy data for this project were acquired by Manjunath Javoor, Bettina Zens and Matthias Percipalle. I genuinely appreciate everyone's cooperative, diligent scientific approach, often going the extra mile to help me out.

I am grateful for support from ISTA's scientific service units. Specifically, to Todor Asenov and his team at the machine shop and electronics workshop for designing bespoke components and electronic modules, always working skillfully and trying their best to meet tight deadlines. Ludek Lovicar and the entire team of the Electron Microscopy Facility went out of their way to facilitate our cryo-workflow. Readers of Chapter 3 will find many

references to equipment they lent us, and beyond that they supported our design choices with expertise in cryogenic and vacuum technology. I thank Robert Hauschild for stimulating conversations about bioimaging, and, together with the team of the Imaging and Optics Facility, lending optical appliances at low threshold. I would also like to thank all other colleagues at ISTA who supported us with equipment, reagents or expertise, thus facilitating a highly collaborative spirit at the institute.

Harald Hess at Janelia Research Campus kindly shared computer-aided design models of their modifications for adapting a vacuum cryostat for vitrified samples. Richard Lincoln from the Hell lab at the Max Planck Institute for Medical Research in Heidelberg generously provided PaX-constructs he developed. I thank Francisco Balzarotti for calling my attention to photoblueing as potential photoswitching pathway for cryo-SMLM. mEmerald-ER-3 was a gift from Michael Davidson (Addgene plasmid # 54082; http://n2t.net/addgene:54082; RRID:Addgene_54082). PaGFP-UtrCH was a gift from William Bement (Addgene plasmid # 26738; http://n2t.net/addgene:26738; RRID:Addgene_26738).

The project was supported by CZI grant DAF2021-234754 and grant DOI: https://doi.org/10.37921/812628ebpcwg from the Chan Zuckerberg Initiative DAF, an advised fund of Silicon Valley Community Foundation (funder DOI: https://doi.org/10.13039/100014989), as well as internal grants from ISTA's Equipment Investment Committee and Interdisciplinary Project Committee.

Finally, I want to wholeheartedly thank my parents for trusting me to find my way and unconditionally supporting me in pursuing my passions. When life got busy, knowing that I always have a place to come home to kept me grounded. I am also very grateful to my family and friends for supporting me through the ups and downs of a PhD, be it by talking issues through, providing advice, or simply having fun together. By raising my mood and helping me unwind, you enabled me to focus on work during busy times. I will remember not only the scientific environment at ISTA, but also the amazing people I met while working here, coffee breaks, ice cream outings, parties, common brunches, lunches and dinners, retreats, …

About the Author

Jakob Vorlaufer first joined ISTA in 2017 as an ISTern during his bachelor studies in technical physics at the Technical University of Vienna. Afterwards, he continued as intern to complete his bachelor thesis project in the Danzl group. Following an exchange semester at Queen's University in Canada, he joined ISTA's graduate school. During his PhD work in the Danzl group, Jakob constructed a cryo-super-resolution microscopy setup. In collaboration with the Schur lab, he worked towards improving imaging of cryo-preserved samples with a focus on correlation with cryo-electron microscopy. These efforts led to a publication in the journal *Biophysical Reports*, and Jakob presented his research at various conferences. He also contributed to other research projects in the lab and outreach.

List of Publications

Related to work described in this thesis:

Vorlaufer, J., Semenov, N., Kreuzinger, C., Javoor, M.G., Zens, B., Dueñas, N.A., Tavakoli, M.R., Šuplata, M., Jahr, W., Lyudchik, J., Wartak, A., Schur, F.K.M., Danzl, J.G., 2025. Image-based 3D active sample stabilization on the nanometer scale for optical microscopy. *Biophysical Reports* 5, 100211. https://doi.org/10.1016/j.bpr.2025.100211

Other contributions (not discussed in the thesis):

Gallei, M., Truckenbrodt, S., Kreuzinger, C., Inumella, S., Vistunou, V., Sommer, C., Tavakoli, M.R., Agudelo Dueñas, N., **Vorlaufer, J.**, Jahr, W., Randuch, M., Johnson, A., Benková, E., Friml, J., Danzl, J.G., 2025. Super-resolution expansion microscopy in plant roots. *The Plant Cell* 37, 4, koaf006. https://doi.org/10.1093/plcell/koaf006

Tavakoli, M.R., Lyudchik, J., Januszewski, M., Vistunou, V., Agudelo Dueñas, N., **Vorlaufer, J.**, Sommer, C., Kreuzinger, C., Oliveira, B., Cenameri, A., Novarino, G., Jain, V., Danzl, J.G., 2025. Light-microscopy-based connectomic reconstruction of mammalian brain tissue. *Nature* 642, 398–410. https://doi.org/10.1038/s41586-025-08985-1

Table of Contents

List of Figures

List of Tables

List of Abbreviations

AF	Alexa Fluor
AFP	Alexa Fluor Plus
CLEM	correlative light and electron microscopy
dSTORM	direct stochastic optical reconstruction microscopy
EM	electron microscopy
EOD	electro-optical deflector
ET	electron tomography
ER	endoplasmic reticulum
FIB	focused ion beam
FPGA	field-programmable gate array
GUI	graphical user interface
ISM	image scanning microscopy
LMS	least mean square
MINFLUX	minimal photon fluxes/maximally informative luminescence excitation
MLE	maximum likelihood estimation
PAINT	points accumulation for imaging in nanoscale topography
PALM	photo-activated localization microscopy
PSF	point spread function
RESI	resolution enhancement by sequential imaging
ROI	region of interest
RT	room temperature
SBR	signal-to-background ratio
SEM	scanning-electron microscopy
SIM	structured illumination microscopy
SLM	spatial light modulator
SMLM	single-molecule localization microscopy
SNR	signal-to-noise ratio
SOFI	super-resolution optical fluctuation imaging
SRRF	super-resolution radial fluctuations
STED	stimulated emission depletion
STORM	stochastic optical reconstruction microscopy
TEM	transmission-electron microscopy
TCP	target coordinate pattern
WF	widefield

1 Introduction

A long-standing goal in biology is to unravel the working principles behind biological systems. Ultimately, these systems are governed by the organization of their constituents across space and time. Therefore, novel biological discoveries often go hand in hand with the development of biological measurement technologies revealing previously inaccessible types of information. Bioimaging is a powerful approach for visualizing spatial arrangements. An ideal imaging instrument would simultaneously provide the exact identity, localization, structure, and copy number of all molecules present in a sample, across relevant spatial scales ranging from Ångström (physical and chemical interactions governing the structure and interaction of biomolecules) to centimeters (tissue organization up to entire organs) at sub-µs temporal resolution. However, such an instrument is far out of reach.

Since all microscopy concepts exhibit inherent strengths and drawbacks, great potential lies in the combination of different techniques. For example, fluorescence microscopy is particularly potent for visualizing specifically labeled molecules, while electron microscopy (EM) shows arrangements with comprehensive structural contrast (Section 1.2). Imaging the same region with both modalities allows for correlation of datasets, thus obtaining a richer picture of the sample. This work focuses on the development of a super-resolution cryo-fluorescence microscope suitable for correlative light and electron microscopy (CLEM).

In the introduction, I describe the concept of *in situ* structure analysis (Section 1.1), pertinent imaging technologies (Section 1.2), and how we envisioned to solve some of the existing technology gaps (Section 1.3). Subsequently, I detail the construction of the microscopy setup used for measurements at room temperature (RT; Chapter 2) and cryogenic conditions (Chapter 3). Finally, I discuss what we have learned and the outlook for further developments in the field (Chapter 4).

1.1 In situ *structural biology and visual proteomics*

The tight relationship between structure and function of biomolecules is a widely established paradigm. Accordingly, studies unraveling molecular structures have greatly contributed to our understanding of the principles governing biological systems. Traditionally, experimental procedures often investigated purified molecules in isolation. Due to the complex organization of biology, however, this reductionistic approach does not provide the full picture, and great potential lies in the investigation of biologically active units situated in their native[1] environments (Young and Villa, 2023).

On the one hand, *in situ* samples evade potential artifacts to molecular structures arising from purification. Beyond this, visualizing rich context surrounding biomolecules can be just as relevant as their structure. For example, studies have performed molecular census of active and inactive proteasomes within neurons (Asano et al., 2015), or investigated the distribution of ribosomes in different maturation states in cytosol and nucleus (Lucas et al., 2022).

[1] It should be noted that samples cannot be classified into binary categories of “isolated” and “native”. Nogales and Mahamid stated that “there is almost a continuum in the nature of the complexity of a sample” (Nogales and Mahamid, 2024). For instance, purification might isolate larger complexes or entire organelles instead of single proteins. Cell fragments or cultured cells may represent a near-native environment for some structures, but lack the rich interactions occurring in complex biological tissue. This is to say that the sample platform should always be carefully adjusted to the scientific question to be addressed, and performing appropriate control experiments wherever possible is imperative to ensuring that observed phenomena are truly biologically meaningful.

The ambitious goal of visual proteomics is to generate a comprehensive "building plan" of biological systems, i.e., unravel the working mechanisms of the molecular machines comprising them. This requires knowledge of molecule identity, structure, census and localization of all relevant constituents. Finally, the full picture has to include the dynamics of cellular processes. Merging these distinct types of information can benefit from integrated approaches, combining, for example, mass spectrometry, imaging and computational modeling (McCafferty et al., 2024). While deep learning has made impressive progress at predicting molecular structures and interactions, faithfully modeling complex systems still hinges on experimental data (Bäuerlein and Baumeister, 2021; Beck et al., 2024).

1.2 Imaging techniques for in situ *structure analysis*

Microscopy techniques differ in key parameters, such as contrast, specificity, resolution and compatible sample preparation. Cryo-electron tomography (ET; Section 1.2.2) has become widespread for *in situ* structure analysis because it provides comprehensive structural contrast of near-natively preserved samples, and allows for the visualization of structures down to sub-nm resolution via averaging. However, depending on the target, identification of molecules within crowded tomograms may be challenged by the low contrast natively produced by individual biomolecules. Fluorescence microscopy, on the other hand, enables essentially background-free visualization of fluorophores specifically attached to molecules of interest at single-molecule contrast over large fields of view. Since some variants of fluorescence microscopy are compatible with living specimens, dynamics can be investigated on the ensemble and single-molecule level. Due to this complementarity, correlating the information from both fluorescence and ET datasets via CLEM thus has the potential to combine information on the location of specific molecules and their structure. Since diffraction limits the resolution of conventional fluorescence microscopy to hundreds of nanometers, super-resolution microscopy techniques (Section 1.2.3) can increase the power of CLEM by visualizing fluorophore arrangements on a finer spatial scale. Performing all imaging steps at cryogenic temperatures minimizes distortions between datasets as well as perturbations to the sample.

1.2.1 Sample fixation

Many microscopy techniques require fixation of the sample – either because the imaging technique is incompatible with living specimens, as for EM and many high-resolution light microscopy techniques, or sample motion during extended acquisition times would lead to image artifacts. Fixing samples through the application of chemical cross-linking is a widely used approach, but can lead to distortions and damage of structures. For example, fixation artifacts in brain tissue (Korogod et al., 2015), the endoplasmic reticulum (ER) (Hoffman et al., 2020) and liquid-liquid phase separation (Irgen-Gioro et al., 2022) have been characterized. The level of damage varies for different arrangements. To an extent, fixation protocols can be optimized for preservation of certain target structures.

Compared to chemical fixation, cryo-fixation is substantially less prone to artifacts. Rapid freezing at cooling rates > 10^4 K/s leads to the formation of amorphous ice. To preserve this vitrified state and avoid the formation of ice micro-crystals, sample temperature must then be kept below 135 K at all times. Vitrification can be achieved by plunge-freezing, where, after removing excess buffer via blotting with filter paper, samples are immersed in a cryo-liquid with a high heat transfer coefficient, commonly ethane or an ethane/propane mixture. The

limited heat transfer in biological matter restricts this technique to samples below ~10 µm thickness. Larger samples up to ~200 µm thickness can be cryo-preserved by placing samples under high pressure while applying liquid nitrogen. Additionally, vitrification can be aided by the addition of so-called cryo-protectants, such as dextran or glycerol.

For plunge freezing, samples are typically grown on EM-grids, comprising a metallic mesh of squares spaced some 10s of µm, and a thin support film. Depending on the application, different materials and geometries of the support film are available. For cryo-EM, high electron transparency and mechanical stability are important considerations. Films are sometimes perforated with holes ("holey film") where electron contrast is not impeded by any additional material. Samples for high-pressure freezing are often grown or placed on thicker glass or sapphire disks withstanding high pressure, but recent workflows utilizing EM-grids have facilitated direct downstream processing for cryo-ET (Young and Villa, 2023).

For some applications, combining chemical fixation and cryo-preservation can be advantageous. For example, Fäßler *et al.* (2020) chemically stabilized actin filaments and extracted membranes, followed by plunge-freezing and cryo-ET. This allowed them to reconstruct the structure of the near-natively preserved Arp2/3 complex bound to actin branch junctions *in situ* to sub-nm resolution. For EM data acquired at RT, high-pressure freezing followed by freeze-substitution, i.e., the replacement of water with a different embedding medium (often an electron-resistant resin) at low temperature, is not completely free of artifacts, but provides superior structural preservation compared to strong chemical fixation and dehydration.

1.2.2 Cryo-electron tomography

A single transmission electron micrograph constitutes a 2D projection of the sample. This type of data is amenable to studying isolated particles exhibiting low variability, such that a large number of them, oriented along different directions, can be merged to reconstruct 3D structures by a method termed single-particle analysis. However, this approach reaches its limits for pleomorphic arrangements or complex sample types. Here, cryo-ET is typically a more apt technique. Cryo-ET reconstructs three-dimensional sample architecture by overlaying 2D EM projections of the vitrified sample acquired at different tilt angles[2].

Due to the finite interaction volume of electrons in scanning-electron microscopy (SEM), reaching sub-nm resolution in biological samples requires transmission-electron microscopy (TEM). This limits applicable sample thickness to a few hundred nanometers[3]. Studying arrangements located deep in the cell interior (as opposed to the cell periphery, which is natively thin) accordingly requires thinning. Mechanical sectioning with a diamond knife has been used for this purpose, but tends to introduce compression artifacts to vitrified matter[4]. During the last decade, thinning by milling a thin lamella with a focused ion beam (FIB) has been adopted by the *in situ* cryo-ET community. Lamellae can be milled directly into cells

[2] Due to limitations of commonly employed sample stages and the penetration depth of the electron beam, tilt angles are limited to ±70° at most. This incomplete angular sampling results in so-called "missing wedge artifacts", which can be corrected in post-processing via deconvolution or deep learning-based approaches.

[3] The mean free path of electrons accelerated to 300 kV was found to be ca. 400 nm in biological matter (Rice et al., 2018). At higher thickness, multiple scattering of electrons quickly reduces contrast. In tomography acquisitions, frames acquired at high tilt angles travel through substantially more material than indicated by the thickness without tilt. Hence, thin samples are particularly desirable.

[4] Resin-embedded samples are less affected by this. Therefore, mechanical sectioning is widely established for volume EM at room temperature.

adhering to the support film, or lifted out from milled trenches for more complex sample types.

The electron contrast of unstained biological matter is inherently weak because it is comprised of elements with low atomic numbers which accordingly have low electron densities[5]. Due to the distribution of the maximum applicable electron dose over many projections, this issue is aggravated for tomography compared to 2D cryo-EM, resulting in low signal-to-noise ratios (SNRs), which can pose a challenge for downstream processing steps.

The spatial scale at which information can be extracted in cryo-ET is typically not limited by the imaging resolution of electron microscopes, but rather by noise obscuring fine structural features. Therefore, analogous to single-particle analysis on 2D cryo-EM data, averaging can recover information at high spatial frequencies from tomograms, and reconstruct molecules at resolutions down to few Å (Tegunov et al., 2021). In an approach called sub-tomogram averaging (Briggs, 2013), volumes containing a copy of the target particle are iteratively aligned with respect to a reference. If particles exist in multiple conformations, classification can increase recovered resolution and at the same time retrieve different states from the dataset.

The unambiguous identification of particles of interest in cryo-electron tomograms is a prerequisite for sub-tomogram averaging, as well as a crucial step for addressing many visual proteomics questions. Particle picking often involves template matching (Lucas et al., 2021; Rickgauer et al., 2017), which requires *a priori* structural information, is computationally expensive and is prone to introducing bias. Recently, deep learning-based data mining has been introduced as alternative approach (de Teresa-Trueba et al., 2023; Moebel et al., 2021; Rice et al., 2023). Still, the low SNR and high complexity of *in situ* data currently restrict particle picking to amenable targets that can be identified due to their large size or based on their association with larger structures. The investigation of many biologically relevant targets based entirely on the cryo-ET signal they generate on their own thus remains out of reach.

The identification of target molecules via localization of “reporter” tags specifically attached to them is a powerful alternative concept. Tags may provide signal in a different imaging modality, such as fluorescence (see next sections), or produce sufficient contrast directly in tomograms. Different versions of such electron-dense tags have been realized which are identified based on their particular shape (Fung et al., 2023; Silvester et al., 2021) or high amplitude contrast provided by heavy elements (Clarke and Royle, 2018; Dahan et al., 2018; Wang et al., 2011). Current realizations are limited by their relatively large size (10s of nm distance from the target) and difficulty to express them *in situ* at high levels. New types of tags are being actively developed, and in the future, improved electron-dense tags might enable the analysis of a wide range of molecules *in situ*.

1.2.3 Super-resolution light microscopy

Fluorescence microscopy is a widely established method in cell biology due do its relative ease of use, high specificity and contrast, compatibility with living specimens, and suitability for multiplexing. Its adoption for structural biology has been limited since resolution

[5] Contrast can be increased by utilizing phase contrast: Only 15 % of electron-matter interaction manifests as amplitude contrast, and the remaining 85 % as phase contrast. Phase plates have been successfully employed for cryo-ET (Mahamid et al., 2016), but are cumbersome to use since phase shifts vary throughout an acquisition due to charging of the phase plate. A new approach, employing a high-intensity laser to shift the phase of electrons, has demonstrated contrast improvement for single-particle samples (Axelrod et al., 2024). Provided the initial technical challenges are solved, its adoption for *in situ* cryo-ET is an interesting prospect.

achievable with most fluorescence microscopy approaches does not reach the spatial scale at which structures are organized on the molecular level. However, this is beginning to change with new developments of nanoscale super-resolution microscopy techniques (Liu et al., 2022; Radmacher et al., 2025). At these length scales, ensuring that datasets faithfully reproduce native biological arrangements becomes more and more crucial. Besides fixation artifacts discussed in Section 1.2.1, fluorophore labeling strategies must be carefully optimized (Grimm and Lavis, 2022; Leake and Quinn, 2023). For example, the linkage error, i.e., distance between fluorophore and target (typically a few to >10 nm; Figure 1.1A), off-target binding and incomplete labeling may misrepresent structures.

Resolution is defined as the closest distance at which separate points in a sample can be distinguished in an image. Diffraction of light poses a fundamental upper[6] bound to the resolution in far-field optical microscope images, as given by the Abbe diffraction limit (Abbe, 1873):

$$d_{xy} = \frac{\lambda}{2\mathrm{NA}} \tag{1.1}$$

Here, d_{xy} denotes the resolution limit in the lateral plane[7], λ the wavelength of light, and $\mathrm{NA} = \mathrm{n}\,\sin(\alpha)$ the numerical aperture of the objective, with n being the refractive index of the immersion medium and α the collection half-angle. In practice, this results in values down to ~200-300 nm for conventional microscopy setups.

However, various imaging approaches not bound by diffraction have been developed. These so-called super-resolution microscopy techniques utilize molecular states of fluorophores attached to structures of interest to 1) distinguish between emitters and 2) establish their spatial coordinates with high precision. Prominent examples are stimulated emission depletion (STED) microscopy (Klar et al., 2000; Klar and Hell, 1999) and single-molecule localization microscopy (SMLM) (Betzig et al., 2006; Hess et al., 2006; Jungmann et al., 2010; Rust et al., 2006; Sharonov and Hochstrasser, 2006) which employ distinct approaches to solve these tasks.

1.2.3.1 Stimulated emission depletion microscopy

In STED microscopy, typically implemented on scanning microscopy platforms, a (diffraction-limited) excitation beam is overlaid with a depletion beam, which de-excites fluorophores via stimulated emission. The depletion beam exhibits a deep intensity minimum in its center, such that it acts only in the periphery of the excitation beam. Detected signal hence originates from the central region exposed to depletion intensities below the saturation intensity I_{sat}. Different beam geometries exist for resolution enhancement in the lateral plane or along the optical axis. Assuming a parabolic intensity profile around the center and exponential fluorescence suppression by STED results in a modified resolution limit (Harke et al., 2008) of

[6] The microscopy community adopted the naming convention that “high resolution” indicates a small resolved distance. Accordingly, an upper resolution bound is equivalent to a lower bound on the resolvable spatial scale.

[7] The corresponding resolution along the optical axis is given by $\frac{2\lambda}{\mathrm{NA}^2}$, thus yielding worse resolution and an increased NA-dependence.

$$d_{\mathrm{STED}} = \frac{d_0}{\sqrt{1 + I_{\mathrm{max}}/I_{\mathrm{sat}}}} \tag{1.2}$$

The improvement over the diffraction-limited resolution d_0 is thus dictated by the ratio of maximum intensity of the depletion beam I_{max} and the saturation intensity, which is set by the lifetime of the excited state and the wavelength-dependent stimulated emission cross-section. As opposed to Equation 1.1, this expression implies a technical challenge rather than a fundamental limit. While various approaches have refined STED acquisitions (Jahr et al., 2020), for typical bioimaging applications, the resolution is limited by the applicable depletion intensity to several 10s of nanometers[8]. Utilizing reversibly switchable fluorophores, instead of stimulated emission, to turn off signal in the RESOLFT approach (Grotjohann et al., 2011; Hofmann et al., 2005) reduces the saturation intensity due to the extended lifetime of the emissive state, but faces the challenge of imperfect switching contrast with currently available photoswitchable fluorophores.

1.2.3.2 Camera-based single-molecule localization microscopy

SMLM utilizes stochastic switching of fluorophores on the single-molecule level for resolution improvement. Typically operating in widefield (WF) mode, a sparse subset of active fluorophores is detected per camera frame, and yields isolated spots (Figure 1.1C). Their diffraction-limited shape, termed point spread function (PSF) of a microscope, can often be approximated as Gaussian function with standard deviation σ_{PSF}. Emitters yielding a signal of N photons can then be localized with a precision of standard deviation[9]

$$\sigma_{\mathrm{SMLM}} = \frac{\sigma_{\mathrm{PSF}}}{\sqrt{N}} \tag{1.3}$$

After some time, active fluorophores switch off and a new set gets activated. Arrangements in the sample are reconstructed by localizing fluorophores over many rounds. Various approaches have been developed to localize emitters in 3D (Lelek et al., 2021; Liu et al., 2020), for example by engineering the PSF-shape via a cylindrical lens or a spatial light modulator (SLM) in the emission path. Here, careful PSF-characterization is instrumental to reaching optimal performance and localizing fluorophores not only with high precision but also high accuracy. It has been shown that using experimentally derived PSF-models can reconstruct finer structural details than relying on theoretical models of the 3D PSF (Li et al., 2018).

Analogous to STED, Equation 1.3 does not impose a hard limit to the achievable resolution in SMLM. Collecting enough photons per emission event in principle allows for arbitrarily high localization precision, but due to the square-root dependence, nanoscale localization requires very high photon numbers. At the same time, an adequate balance of inactive to active fluorophores has to be maintained to ensure a sufficiently low probability of overlapping emitters. Moreover, on length scales below 10 nm, some approaches suffer from interactions between fluorophores which may quench fluorescence and lead to localization artifacts (Helmerich et al., 2024). Moreover, potential localization biases arising, e.g., from uncorrected sample drifts, dipole orientation effects (Enderlein et al., 2006; Engelhardt et al., 2011; Lew et al., 2013) or inhomogeneous background have to be carefully considered.

[8] This does not hold true for the MINSTED concept (Weber et al., 2021), which is discussed below.

[9] The following equation neglects background and the finite size of camera pixels. See Mortensen *et al.* (2010) for a detailed analysis and amended expression.

Localization precision in SMLM is distinct from resolution, which also requires dense sampling of structures. Resolution can be assessed via Fourier ring correlation (Nieuwenhuizen et al., 2013) or reference structures of known geometry (Jungmann et al., 2010; Steinhauer et al., 2009; Thevathasan et al., 2019).

A distinctive property setting apart different families of SMLM is the mechanism they employ for single-molecule switching (Figure 1.1B). Some fluorophores, notably a range of silicon rhodamines, spontaneously switch between different conformations, one of which emits fluorescence upon illumination with excitation light, i.e., is optically "active" – in an "on-state". The spontaneous nature of switching makes these fluorophores amenable to live-cell imaging, but at the same time limits active control over switching behavior.

A widespread SMLM approach is stochastic optical reconstruction microscopy (STORM) (Rust et al., 2006), which uses reversible blinking of fluorophores induced by excitation light. In initial implementations, activator dyes promoted photoswitching of reporters, but nowadays, the direct STORM (dSTORM) variant (Heilemann et al., 2008) using intrinsic photoswitching pathways is predominant due to the straightforward workflow. Typically, fluorophores reside in an active state before the start of an experiment and are switched off by high-intensity laser illumination. Both on- and off-switching are mediated by the excitation laser. For some fluorophores, blue or violet laser pulses applied during SMLM measurements can promote activation. Switching pathways usually involve photo-chemical reactions, but the exact mechanisms differ between fluorophores and are often not precisely known. Systematic characterizations of dyes (Dempsey et al., 2011; van de Linde et al., 2011) found far-red cyanine dyes, such as Cy5 or Alexa Fluor (AF) 647, to be particularly well suited for dSTORM, a result still largely holding true 14 years later. Their switching pathways involve a redox reaction, which is facilitated by buffers containing thiols, such as β-mercaptoethanol or mercaptoethylamine. Oxygen scavenger systems often improve performance (Dempsey et al., 2011). While synthetic dyes typically exhibit superior photophysical properties, switchable fluorescent proteins, such as Dronpa (Ando et al., 2004) and rsEGFP (Grotjohann et al., 2012, 2011), can be attractive options for imaging in living cells since they can be more easily expressed and switch in native cellular environments.

In an alternative switching approach named photo-activated localization microscopy (PALM), fluorophores are activated with blue or (ultra-)violet light, and bleach irreversibly upon illumination by excitation light (Betzig et al., 2006). This irreversible switching makes it harder to achieve sufficiently high localization densities, but can be useful for quantitative analyses. Moreover, distinct wavelengths for on- and off-switching provide additional control over the concentration of active emitters[10]. Some fluorophores are photoconvertible, which means that they can be imaged at a different wavelength prior to activation. Again, exact activation pathways vary between fluorophores, but for many fluorescent proteins, they involve conformational changes or charge transfer. Most standard photoactivatable fluorophores are fluorescent proteins, for example PAGFP (Patterson and Lippincott-Schwartz, 2002), PAmKate (Gunewardene et al., 2011), PAmCherry (Subach et al., 2009) or mMaple (McEvoy et al., 2012), but organic dyes, such as the PA-JF (Grimm et al., 2016) and PaX (Lincoln et al., 2022) families, have been developed as well.

The switching schemes discussed so far involve changes to molecular states which have to be carefully engineered to provide a large number of photons per on-event, while at the same

[10] Full optical control would entail three separate wavelengths for activation, excitation, and de-activation. This is realized for the reversibly switchable fluorescent protein Dreiklang (Brakemann et al., 2011).

time maintaining a sufficiently small fraction of simultaneously active emitters. Substantial progress has been made here, but since it is challenging to design fluorophores with bespoke properties, there are limits to the level of optical control. Improved control, and therefore improved performance, can be achieved in modern implementations of the points accumulation for imaging in nanoscale topography (PAINT) concept (Sharonov and Hochstrasser, 2006). In PAINT, freely diffusing fluorophores bind transiently to target structures. Due to the fast time-scales of diffusion, only bound molecules produce a strong signal which allows for their localization. Hence, the photon yield is determined by the product of the binding time and the photon detection rate. A particularly successful variant of PAINT is DNA-PAINT (Jungmann et al., 2010), where target molecules are labeled with short single-stranded DNA-sequences, with complementary sequences attached to fluorophores. Binding rates can be optimized by modifying the sequences (Schnitzbauer et al., 2017) which is substantially more straightforward than modifying optically switchable fluorophores to achieve desired switching properties. DNA-PAINT is also amenable to multiplexing by sequentially imaging orthogonal sequences for different targets (Jungmann et al., 2014; Schueder et al., 2024; Unterauer et al., 2024).

In the recently introduced resolution enhancement by sequential imaging (RESI) approach (Reinhardt et al., 2023), a single protein species is labeled with different DNA-sequences, which are read out in sequential PAINT measurements. Every round produces isolated clusters of localizations, arising due to repeated binding of fluorophores. For each cluster, these are averaged to generate a single estimate of the fluorophore coordinates at substantially improved precision down to ~1 Å. This approach resolved the dimeric arrangement of the Nup96-proteins in the nuclear pore complex inside cells in 3D, and studied the reorganization of CD20 membrane receptors after drug treatment on the single-molecule level.

However, more “straightforward” SMLM experiments, too, can give insights into structural arrangements within cells. For example, Mund *et al.* (2023) quantitatively analyzed deformations to the clathrin coat during endocytosis by forming pseudo-time series from 1798 clusters imaged via 3D dSTORM. Also using dSTORM, Jimenez Sabinina *et al.* (2021) formed a comprehensive model of the relative arrangements of 6 protein species in the nuclear pore complex. These nanoscale-resolution SMLM data call for new types of analysis to exploit the full potential of fluorescence-based *in situ* structure analysis (Liu et al., 2022). Some approaches might be borrowed from the cryo-ET field, potentially adapting them to account for different data properties. For example, particle averaging (Heydarian et al., 2021, 2018) is becoming more and more widespread in the super-resolution microscopy community. However, the primary aim is not increasing contrast but typically compensating for incomplete structural representation due to imperfections associated with labeling, imaging and analysis. While the resolution of fluorescence imaging is ultimately limited by the size of fluorophores and linkers, it might become a potent complementary technique to cryo-EM/ET for structural biology (see also next section).

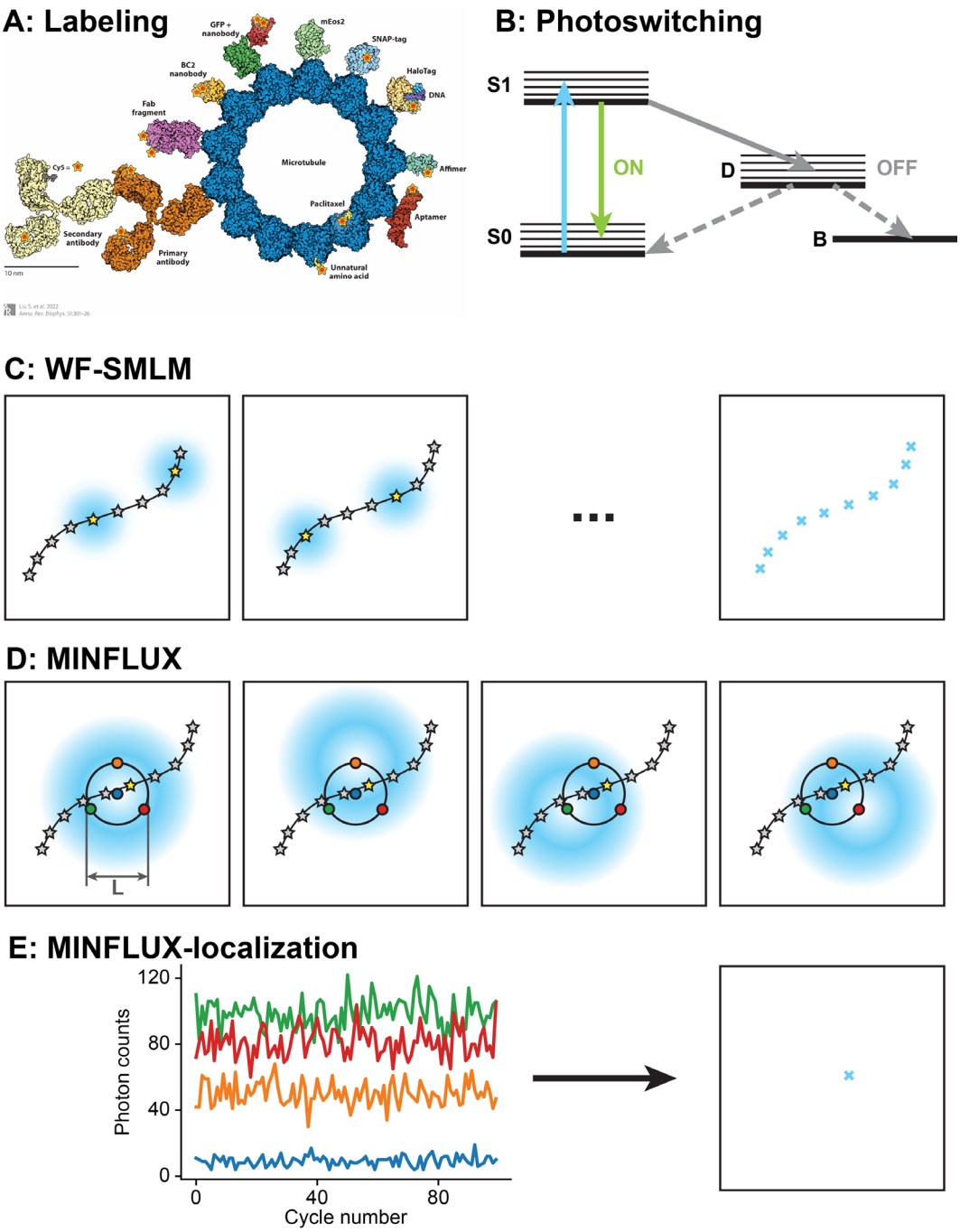

Figure 1.1: Principle of Camera-based SMLM and MINFLUX. ***A:*** *Labeling strategies for high-resolution fluorescence imaging. Relative sizes of structures were preserved in the visualization. Red stars signify fluorophores. Panel reproduced from (Liu et al., 2022) with permission from Annual Reviews.* ***B:*** *Jablonski diagram of a generic photoswitching cycle. In the active on-state, the fluorophore cycles between ground state (S0) and first excited singlet state (S1), absorbing excitation light (cyan) and emitting fluorescence (green). With some probability, it can switch off to a long-lived dark state (D), whose nature varies between fluorophores, as discussed in the main text. In reality, D can comprise a manifold of different molecular states. From there, the fluorophore might either return to the ground state, switching the fluorophore back on, or bleach irreversibly (B).* ***C:*** *Camera-based SMLM scheme. Sparse active fluorophores (yellow) are detected as diffraction-limited spots (blue "disks"). Emitters are localized (blue crosses), thus reconstructing fluorophore arrangements over many rounds.* ***D:*** *MINFLUX scheme. Localization of a single fluorophore is outlaid, with panels showing TCP-exposures. Color-coded points correspond to beam centers.* ***E:*** *Schematic MINFLUX localization. Emitter coordinates are estimated from photon count traces (simulated; colors correspond to TCP-exposures in D). See Section 2.4.1 for details on our implementation.*

1.2.3.3 MINFLUX microscopy and related concepts

In the relatively new concept of localizing emitters based on minimal photon fluxes (MINFLUX[11]) (Balzarotti et al., 2017), fluorophores are rendered distinct through single-molecule switching utilizing the same mechanisms as described in the previous section. However, rather than localizing PSFs detected on a camera chip, fluorophore coordinates are estimated through the response to a patterned excitation beam placed at a set of positions around the emitter (Figure 1.1D-E) – the target coordinate pattern (TCP). The excitation beam exhibits a deep minimum in the center, akin to the depletion beam in typical STED microscopy implementations (Section 1.2.3.1). An important consequence of localizing fluorophores by finding the coordinates of minimum rather than maximum signal is the greatly increased spatial information encoded in every detected photon ("photon efficiency"). For a parabolic beam profile, this results in the following Cramér-Rao bound (giving the theoretically achievable localization precision of an unbiased estimator) at the center of the TCP:

$$\sigma_{\mathrm{MINFLUX}}(r=0) = \frac{L}{\gamma\sqrt{N}} \tag{1.4}$$

Here, L indicates the TCP-diameter, N the number of detected photons, and γ is a parameter whose value depends on the specific TCP-geometry (Schmidt et al., 2021). Away from the center, the precision worsens[12]. This expression implies that for a given number of detected photons, precision can be improved arbitrarily by shrinking the size of the TCP, albeit at the cost of accelerated deterioration away from the center. Importantly, this is only true in the absence of background. For finite signal-to-background ratios (SBRs), the Cramér-Rao bound exhibits a local minimum for a finite value of L.

Of note, localization precision in MINFLUX scales linearly with TCP-size, but only with the square root of detected photons. This implies that during the localization process, it is more efficient to use the information from previously detected photons to refine the TCP rather than waiting for more photons. This notion has motivated the development of iterative MINFLUX (Gwosch et al., 2020), which results in an improved Cramér-Rao bound of

$$\sigma_{\mathrm{iterative}} \propto k^{k/2}\frac{L_1}{N_t^{k/2}} \tag{1.5}$$

L_1 is the TCP-diameter of the first iteration, k the number of iterations, and N_t the total number of detected photons across all iterations. In practice, the SBR limited implementations to 4 or 5 iterations (Gwosch et al., 2020; Schmidt et al., 2021). Still, nm-scale localization precision on cellular targets was achieved using a modest number of 2000 photons. Furthermore, extensions to 3D and dual-color localization were realized (Gwosch et al., 2020) and also implemented on a commercial microscope platform (Schmidt et al., 2021).

By enabling 3D super-resolved imaging on the single-molecule scale, MINFLUX has the potential to generate insights into protein arrangements and their internal structure. For example, the distribution of various proteins inside the active zone of photoreceptors was investigated by MINFLUX which led to a refined description of synaptic vesicle docking

[11] The abbreviation can also stand for Maximally INFormative LUminescence eXcitation (Balzarotti et al., 2017).

[12] For 1D localization with two beam exposures separated by L, the relation $\sigma(x) = \frac{L}{4\sqrt{N}}((2x/L)^2 + 1)$ is found analytically (Balzarotti et al., 2017). In higher dimensions, the relationship becomes anisotropic, but the general concept of reduced precision away from the center holds true.

(Grabner et al., 2022). MINFLUX also resolved different states of the PIEZO1 protein, revealing a high level of flexibility in its peripheral parts, termed blades, which had previously hampered their complete reconstruction with cryo-EM (Mulhall et al., 2023).

The realization that background fluorescence poses a challenge to MINFLUX has prompted the development of MINSTED (Weber et al., 2021) combining concepts from STED and SMLM. Analogous to conventional STED microscopy, a depletion laser generates a narrowed "effective PSF". Signal detected by circling this ePSF around a single active emitter is used for localization. Since the depletion laser typically suppresses background rather than exciting it, the SBR does not decrease upon "zooming in" on fluorophores. MINSTED has achieved Å-scale localization precision, limited by the mechanical stability of the setup (Weber et al., 2022). However, this remarkably high precision comes with increased experimental complexity and additional photophysical requirements.

It is evident that studies of static molecular arrangements can greatly facilitate biological insight. However, a complete understanding of biological processes also requires the consideration of molecular dynamics. A distinctive feature of both MINFLUX and MINSTED is the high localization speed of few 100 µs for common implementations[13]. Together with the high photon efficiency, this makes the approaches uniquely poised for single-molecule tracking. For example, stepping of the motor protein kinesin-1 was resolved at native ATP-concentrations [14] by MINFLUX (Deguchi et al., 2023; Wolff et al., 2023) and MINSTED (Scheiderer et al., 2024a), and dual-color MINFLUX uncovered that it can switch between two stepping modes (Scheiderer et al., 2024b). Another example where MINFLUX-based tracking revealed biological information is the direct observation of overlapping import and export paths in nuclear pore complexes with an exclusion zone in the center (Sau et al., 2025).

MINFLUX started out as a conceptual revolution for single-molecule localization. Since then, it has proven to be a versatile tool capable of generating novel biological insight. Since the concept is still rather new, it remains to be seen for which applications MINFLUX will become the preferred choice, and where advanced versions of camera-based SMLM will prevail.

1.2.3.4 Super-resolution microscopy at cryogenic temperature

Most modern microscopy measurements – including all of the examples presented in this section so far – are performed at RT. While holding the sample in a cryogenic environment comes with additional engineering overhead and introduces constraints to the microscope design, cryo-fluorescence imaging preserves samples in a near-native state (Section 1.2.1) and lends itself to downstream correlation with cryo-EM data (Section 1.2.4). Temperature has a substantial effect on the photophysics of commonly used fluorophores. Cooling samples typically greatly increases the photons provided before bleaching, and narrows excitation and emission spectra. For cryo-super-resolution microscopy, this simultaneously poses challenges and opportunities.

[13] Localization speed must not be confused with throughput, which is low because localization is performed sequentially. Different approaches have combined patterned excitation with parallelized readout of emitter coordinates (Cnossen et al., 2020; Gu et al., 2019; Jouchet et al., 2021; Reymond et al., 2019), but they are lacking the distinctive feature of targeting specific emitter coordinates with excitation light. Hence, these concepts produced approximately doubled localization precision compared to camera-based SMLM with the same number of photons, but their performance did not reach that of MINFLUX or MINSTED.

[14] This level of spatio-temporal resolution previously required bright nanoparticles fused to motor proteins which are substantially more perturbative than fluorescent dyes due to their large size and mass.

Holding samples below the devitrification temperature of 135 K requires dedicated cryo-stages. In open cryo-stages, samples are thermally coupled to a reservoir of liquid nitrogen, and the stages contain an opening through which the objective is inserted from the top. Since there is no window between sample and objective, the working distance of typically employed air objectives[15] must be long enough to prevent heating of the sample, or accumulation of ice condensation on the front lens. Despite the positive pressure from evaporating nitrogen, open cryo-stages can be prone to introducing ice contamination on samples as well. Additionally, flow of nitrogen gas between sample and objective might lead to image aberrations potentially interfering with super-resolution imaging. Closed cryo-stages containing a glass window between sample and objective entail options for operation under vacuum and using liquid helium to reach lower temperatures. Contamination might be less pronounced which would enable extended acquisition times. Currently available commercial vacuum cryostats are not compatible with (un)loading of vitrified samples, necessitating some modifications (Hoffman et al., 2020; Li et al., 2023, 2015; Mazal et al., 2025a), but cryostats can reach increased mechanical stability compared to commercial open cryo-stages. See Chapter 3 for a direct comparison of the performance of open and closed cryo-stages performed on our homebuilt setup.

Preserving samples in a vitrified state does not only require adequate cryo-stages but also careful consideration of microscopy acquisition schemes because light absorbed by the sample itself or surrounding components is typically converted to heat. Heating the sample locally above 135 K leads to formation of crystalline ice, and at higher intensities even melts the sample. Many super-resolution techniques commonly employ high optical intensities, such that cryogenic implementations generally have to be adapted which may affect their performance in different ways. Sample heating is a product of both optical absorption and finite heat transfer. Accordingly, sample mounting critically influences devitrification. For example, it has been shown that absorption by commonly used support films consisting of amorphous carbon is a major source of devitrification. Hence, applying metal coatings (Dahlberg et al., 2022; Last et al., 2023) or using different film materials (Last et al., 2023; Liu et al., 2015) can substantially increase the optical intensity at which devitrification sets in, but many of these options adversely affect cryo-EM acquisition on regions covered by support film. Other support materials such as sapphire disks allow for higher optical intensities (Hoffman et al., 2020), but do not allow for direct correlation to TEM without liftout. Furthermore, stage design presumably affects devitrification through the degree of provided thermal coupling. For example, convective heat transfer is obviously suppressed in vacuum, and simulations indicated that this reduced the devitrification threshold by 20 % for carbon films (Mojiri et al., 2025). Of note, while devitrification clearly hampers downstream correlation to cryo-EM data, so far to my knowledge there are no conclusive data on the implications for cryo-super-resolution imaging on its own.

Of all super-resolution approaches at cryogenic temperatures, SMLM has arguably been most widely explored. Indeed, before the adoption for bioimaging at RT, pioneering single-molecule observations were performed on samples cooled to few K (Moerner and Orrit, 1999). SMLM performance is tightly linked to fluorophore photophysics, which is highly temperature-dependent. Freezing substantially reduces the quantum yield of photobleaching

[15] Cryo-immersion objectives have been developed (Faoro et al., 2018; Faul et al., 2025; Nahmani et al., 2017; Wang et al., 2019), providing a potential route to increased resolution and reduced contamination. Moreover, dedicated cryo-objectives, distributed for example by Leica Microsystems, with a modified frontend strongly reducing thermal conductivity, achieve an NA of 0.9 at 0.3 mm working distance without immersion media.

and alters photoswitching kinetics. Dahlberg and Moerner (2021) identified two important factors impacting cryo-photophysics for super-resolution imaging: Suppressed generation of reactive oxygen species, and changed energy landscape affecting pathways for active optical control.

Many photobleaching pathways start from the first triplet state of fluorophores where they can generate reactive oxygen species via triplet-triplet annihilation [16] or electron transfer. These reactive oxygen species can induce photobleaching via a variety of reaction pathways. Low temperatures both reduce the speed of these reactions and strongly suppress diffusion of molecular oxygen. This results in reduced photobleaching, whose extent varies between fluorophores, often providing $>10^6$ photons (Dahlberg et al., 2018; Hulleman et al., 2018). It also increases the triplet state lifetimes of fluorophores.

Since triplet states are still too short-lived for common SMLM applications, additional transitions are usually required to induce photoswitching at suitable levels. Some transitions become highly unfavorable upon reducing thermal energy. For example, flexibility of molecules is generally reduced upon freezing which makes large conformational rearrangements highly unlikely. The reversibly photoswitchable fluorescent protein rsEGFP2 exhibits a fundamentally altered switching pathway at cryogenic temperature, involving two off-states with distinct photophysical properties (Mantovanelli et al., 2023). An investigation of 7 fluorescent proteins showed that some exhibited completely different switching characteristics at cryogenic temperature, and off-switching was substantially slowed down for all of them (Tuijtel et al., 2019). Slow off-switching was also reported for PAmKate (Dahlberg et al., 2018), but a more efficient switching pathway was found by testing illumination schemes involving a range of different wavelengths (Perez et al., 2024).

The altered cryo-photophysics, together with low applicable laser powers to preserve samples in their vitrified state, poses the challenge of utilizing the potentially improved localization precision at cryogenic temperatures for SMLM, while at the same time fulfilling the requirement of sufficient sparsity of active emitters. Many of the efforts in this direction combined cryo-SMLM with cryo-EM, and will be discussed in the next section. However, cryo-SMLM has also been established on its own. Labeling few (between 2 and 7) binding sites on isolated particles enabled identification of single-molecule emission events for fluorophores exhibiting a relatively high ratio of active to inactive emitters. Averaging emission events based on intensity (Weisenburger et al., 2017) or polarization (Böning et al., 2021) provided Å-scale localization precision, which, together with data processing workflows adapted from single-particle analysis for cryo-EM[17], reconstructed the arrangement of molecular complexes in 3D (Mazal et al., 2022; Weisenburger et al., 2017). A recent study moved the technique from purified particles embedded in a polymer film to membrane receptors of unroofed, vitrified cells (Mazal et al., 2025b), constituting an important step towards *in situ* investigation of protein structures with light microscopy.

As mentioned in Section 1.2.3.2, localizing fixed dipole emitters can introduce localization bias (Enderlein et al., 2006; Engelhardt et al., 2011; Lew et al., 2013). This is directly relevant for cryo-SMLM since fluorophore rotation is hindered in vitreous environment. Bias was calculated to be on the Å-scale when the NA of the objective was below 1 (Weisenburger et al., 2014). However, simulations also showed that for large defocus and high background levels, it can reach up to 50 nm (Hinterer et al., 2022). This result was corroborated

[16] O_2 is chemically inert in its triplet ground state but highly reactive in its first excited singlet state.

[17] Of note, particles not in line with expected arrangements were filtered out during processing. Hence, to an extent this approach relies on *a priori* information.

experimentally (Furubayashi et al., 2019). Various approaches have been proposed to eliminate biases, such as PSF-modulation (Hinterer et al., 2022; Hulleman et al., 2021b). A potentially more severe source of localization bias, in particular for imaging targets some distance away from the surface, is the refractive index change between plunge-frozen samples and the environment (DeRosier, 2021; Li et al., 2025). FIB-milling may help to polish the cell surface and mitigate aberrations. Index-matched cryo-immersion objectives would alleviate this issue, but suffer from increased dipole-induced localization bias due to their high NA.

While cryo-SMLM has yet to reach the localization density of state-of-the-art RT-counterparts for a wide range of application scenarios, this limitation may be – at least to a large part – due to a lack of dedicated fluorophore engineering efforts rather than fundamental limits. Over the last decades, fluorophores have been extensively optimized for application at RT, with cryogenic temperatures, in particular those provided by liquid nitrogen, being a comparatively small niche. Outcomes of ongoing developments of cryo-compatible fluorophores may be an important factor determining the direction of cryo-SMLM.

Fluctuation-based super-resolution microscopy techniques like super-resolution optical fluctuation imaging (SOFI) (Dertinger et al., 2009) and super-resolution radial fluctuations (SRRF) (Gustafsson et al., 2016) increase resolution by extracting information encoded in brightness fluctuations of fluorophores without the requirement of localizing isolated emitters. While these approaches do not reach the nanoscale resolution of state-of-the-art SMLM, relaxed photophysical constraints can be appealing for straightforward adoption at cryogenic temperature. Both cryo-SOFI (Moser et al., 2019) and cryo-SRRF (Huebinger et al., 2021; Kirchweger et al., 2023) have been implemented, reaching resolution on the order of 100-200 nm. Data quality may be improved by more stable cryo-stages and cooling with liquid helium.

Both enhanced photostability and reduced optical transition linewidths are intriguing features for cryo-STED microscopy because bleaching often limits the applicable depletion intensity, and suppressed anti-stokes excitation would enable less red-shifted depletion wavelengths, resulting in an increased stimulated emission cross-section and increased resolution for a given intensity. However, the high intensities required for high resolution in STED [18] (see Equation 1.2) pose a challenge to the adoption at cryogenic temperatures. Besides, it was found that increased triplet state lifetime led to accumulation of fluorophores in a triplet state, requiring an additional laser to depopulate it (Giske, 2007). Still, this implementation reached a resolution of roughly 130 nm. A different implementation imaging cells grown on a diamond disk with high heat conductivity did not report adverse photophysical effects[19] for the dye AF647, and attained markedly improved[20] resolution over confocal imaging (Huebinger et al., 2021). However, vitrification after STED imaging is yet to

[18] In room temperature STED acquisitions, depletion pulses reach up to GW/cm^2 peak intensity.

[19] A reason for this discrepancy may be the vacuum environment used by Giske (2007) and different sample types. Hulleman *et al.* (2021a) found dark state buildup to be promoted in vacuum and reduced upon the addition of the triplet quenching agent Trolox.

[20] The authors claim Nyquist-limited resolution of 80 nm, arguing that the Fourier transform of their STED images exceeds that of confocal at high spatial frequencies. In my opinion, this is not an adequate way to measure resolution, so I am refraining from stating an explicit number.

be thoroughly investigated[21]. Altogether, a more comprehensive characterization would be desirable to evaluate the practically achievable performance and limits of cryo-STED.

1.2.4 Correlative light and electron microscopy

As mentioned above, due to the complementarity of fluorescence and electron microscopy, combining the two techniques can be a powerful concept for visualizing samples in a more comprehensive way (de Boer et al., 2015; Hauser et al., 2017; van den Dries et al., 2022). This CLEM approach has been adopted for a wide range of applications, for example to confirm sample integrity, identify rare arrangements, or molecularly annotate EM-datasets. Depending on required imaging parameters, different microscopy techniques have been utilized – diffraction-limited or super-resolution fluorescence imaging operating at RT or cryogenic conditions. Due to the relevance for my dissertation, I focus on super-resolution cryo-CLEM here. Performing all imaging steps at cryogenic temperature allows for visualization of near-natively preserved samples and minimizes distortions between datasets. As discussed in the previous section, these low temperatures have a profound impact on super-resolution imaging, posing challenges and opportunities as the same time.

The choice of super-resolution technique depends on the motivation for applying CLEM. A promising application is the localization of structures of interest for subsequent FIB-milling (Arnold et al., 2016). Since lamellae are typically ~100-200 nm thick, this requires a resolution on this scale in 3D. Additionally, fluorescence can add molecular information to the structural context provided by cryo-ET. Super-resolution allows for correlation on finer spatial scales, identifying, for example, regions within organelles or domains. Beyond localization, fluorescent sensors can provide information on various parameters such as the local redox environment read out at cryogenic temperature (Perez et al., 2022).

Microscopy techniques like structured illumination microscopy (SIM) and image scanning microscopy (ISM) attain resolution enhancement over the Abbe limit by factors of 1.4-2 without manipulating molecular states, while being still fundamentally bound by diffraction[22]. Reduced bleaching is attractive for cryo-SIM (Phillips et al., 2020), and the technique has been correlated to cryo-X-ray microscopy (Kounatidis et al., 2020), RT-FIB-SEM (Hoffman et al., 2020) and cryo-FIB-milling (Li et al., 2023). Cryo-ISM has been widely adopted due to the ease of implementation and availability of commercial solutions. For example, Wu *et al.* (2020) used ISM integrated in a cryo-FIB-SEM in a “mill-and-view” configuration. Not relying on super-resolution imaging, Sica *et al.* (2024) used fluorescence interference effects at the sample surface to guide identification of isolated particles during FIB-milling at accuracy below the diffraction limit.

The implications of cryo-photophysics for SMLM, discussed in the previous section, have heavily affected all implementations correlating cryo-SMLM to cryo-ET data. An initial demonstration fluorescently labeled the bacterial type-6 secretion system (Chang et al., 2014). SMLM acquisition was limited by devitrification, and of the tested fluorophores the authors only found PAGFP to be sufficiently photoactivatable. Liu et al. (2015) obtained higher localization precision with the fluorescent protein Dronpa targeting TOMM20 in mitochondria by exchanging the carbon support film for formvar. This allowed for increased optical

[21] Vitrification was assessed based on the lack of regions of excluded fluorescence, from which the authors deduce the absence of ice crystals. However, conclusive analysis would require investigation of electron diffraction or other appropriate methods.

[22] Hence, depending on the exact definition of the term, they are often not classified at “super-resolution” microscopy techniques.

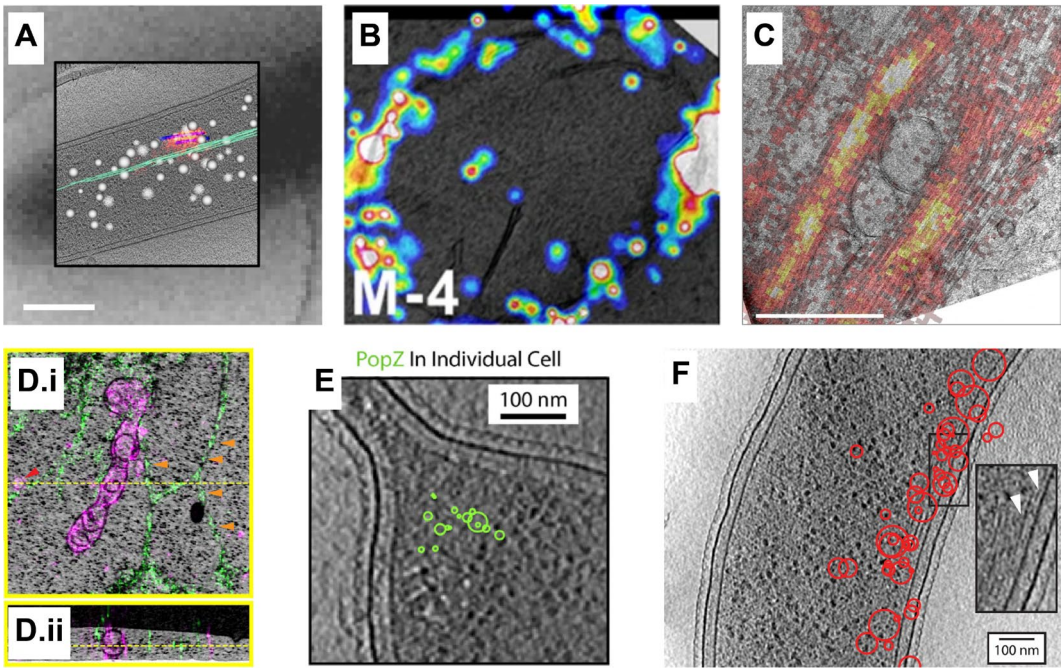

Figure 1.2: Literature examples of cryo-SMLM data correlated to FIB-SEM (D) or cryo-ET (all other panels). ***A:*** *PAGFP-VipA localized to the T6SS, expressed in* M. xanthus *bacterium. Cryo-PALM data visualized with red hot colormap. Additionally, segmented cellular structures are displayed. Scale bar: 400 nm. Reproduced Chang, Y.W., et al. Correlated cryogenic photoactivated localization microscopy and cryo-electron tomography. Nature Methods 11, 737–739 (2014). https://doi.org/10.1038/nmeth.2961 with permission from Springer Nature.* ***B:*** *Dronpa-TOMM20 localized to the outer mitochondrial membrane in HEK293 cell. Panel shows a single vitrified section on formvar film. Reproduced from (Liu et al., 2015) under CC BY 4.0 license.* ***C:*** *rsEGFP2-MAP2 targeting microtubules in U2OS cell. Scale bar: 1 µm. Reproduced from (Tuijtel et al., 2019) under CC BY 4.0 license.* ***D:*** *mEmerald-ER3 (ER lumen, green) and JF525-TOMM20 (outer mitochondrial membrane, magenta) in COS-7 cell. Red arrows indicate TOMM20-positive vesicles and orange arrows ER varicosities. Cryo-SMLM was performed in 3D; D.i shows xy view and D.ii xz. Panel reprinted from Hoffman, D.P. et al., Science, 17 Jan 2020, Vol 367, Issue 6475, pp. 1436-1439, DOI: 10.1126/science.aaz5357 with permission from AAAS.* ***E:*** *PAmKate-PopZ, expressed in* C. crescentus *bacterium. Due to slow off-switching, few localizations were obtained within viable acquisition times. Panel reproduced from (Dahlberg et al., 2020) under CC BY-NC-ND 4.0 license.* ***F:*** *PAmKate-CreS, expressed in* C. crescentus *bacterium. Coating support grids with silver and applying a modified illumination scheme resulted in an increased localization rate compared to E. Panel reproduced from (Perez et al., 2024) under CC BY-NC-ND 4.0 license.*

intensity, albeit at the cost of reduced contrast of cryo-EM data. Out of 7 tested fluorescent proteins, Tuijtel *et al.* (2019) found rsEGFP2 and rsFastLime to be most amenable to cryo-SMLM due to their comparatively fast off-switching kinetics[23], and visualized bundles of microtubules. In a follow-up study, they evaluated the effect of different support grids (Last et al., 2023). Dahlberg *et al.* (2020, 2018) demonstrated high localization precision of cryo-SMLM, localizing the fluorescent protein PAmKate tagging different bacterial proteins. However, due to slow off-switching, the localization density was low. The same team later improved on this by utilizing metallic support films (Dahlberg et al., 2022) and different off-switching pathways (Perez et al., 2024), but so far correlation remained at the level of bacterial domains. Some of the highest cryo-super-resolution data quality on cellular structures was attained by Hoffman *et al.* (2020), whose workflow on high-pressure frozen cells entailed dual-color SMLM in a vacuum cryostat cooled with liquid helium, acquiring for a full day. Using a sapphire disk as sample carrier allowed for increased optical intensity. Cryo-

[23] Switching was still substantially slowed down compared to room temperature.

SMLM reconstructions of the ER and mitochondria were correlated to FIB-SEM data acquired after freeze-substitution. This made imaging less sensitive to potential ice contamination and devitrification, but freeze-substitution deformed samples which reduced correlation accuracy.

Accurately overlaying the fluorescence and the EM dataset is a central step in all CLEM workflows. Together with the optical resolution, the registration accuracy determines the spatial scale at which correlative information can be read out. Registration typically utilizes features providing high contrast in both modalities, for example beads (Chang et al., 2014; Liu et al., 2015; Tuijtel et al., 2019) or holes in the support film (Dahlberg et al., 2020). Due to the small field of view of high-resolution cryo-ET, registration is often performed in two steps: Fluorescence to low-magnification cryo-EM, followed by low- to high-magnification cryo-EM datasets. In theory, 3 points are enough to determine an affine transformation between datasets, but using 4 or more was shown to substantially increase registration accuracy (Arnold et al., 2016). However, for 6 correlation points, this study still reported errors of several 10s of nm, with some outliers showing substantially worse correlation. Errors might be in part due to non-linear deformations arising, e.g., from sample handling, optical aberrations or interaction of the sample with the electron beam. Since cells do not avidly take up typical fiducial markers[24], correlation points tend to be some distance away from target structures for *in situ* samples. Hoffman *et al.* (2020) utilized a cellular reference structure providing suitable signal in both imaging modalities as *in situ* fiducials to locally refine correlation, thus correcting non-linear distortions caused by sample treatment (see above). Resulting registration accuracy was strongly correlated with the local density of *in situ* fiducials.

1.3 Goals of this dissertation

Despite the substantial progress at imaging biological samples discussed so far, the long-standing aim of visualizing molecules embedded in their rich cellular context remains only partially solved. For some molecules, cryo-ET has provided sub-nm resolution *in situ*, but so far, particle identification within the crowded cellular environment has limited its applicability for *in situ* structure analysis. Moreover, the small field of view of high-resolution cryo-ET may render comprehensive analysis challenging. Super-resolution fluorescence microscopy, on the other hand, has recently entered resolution levels on the order of protein sizes on amenable sample types. Most of this work has been performed on chemically fixed samples which might have induced artifacts. Moreover, fluorophores were visualized largely in isolation, thus neglecting the complex environment surrounding them. Super-resolution cryo-CLEM holds great potential for combining molecular and structural information since fluorescent tags provide high contrast at a small size, can be efficiently linked to targets through versatile labeling strategies, and light microscopy covers substantially increased fields of view compared to high-magnification cryo-EM. However, technical challenges associated with cryo-super-resolution microscopy and registration of datasets have limited this approach thus far to the level of cellular organelles or bacterial domains.

[24] Fluorescently coated gold beads taken up by cells through endocytosis (Berger et al., 2021) and fluorescently labeled lipid droplets (Scher et al., 2021) have been used as fiducial markers within cells, but their distributions tend to be heterogeneous.

This has hampered the adoption of fluorescent tags for guiding *in situ* structure analysis so far. Performing molecular census or identifying sub-volumes for sub-tomogram averaging based on fluorescent signals would typically require 3D resolution and correlation accuracy below 10 nm. If successfully implemented, cryo-fluorescence-guided *in situ* structure analysis could provide a generally applicable strategy for particle picking, independent of molecular size or known association with larger structures. Since it would not require a structural template, *in situ* structures could be solved *de novo* without relying on *a priori* references, which are not always available. Moreover, fluorophores would label target molecules in a largely unbiased manner. Depending on the labeling strategy, fluorophores are displaced from the target to varying degrees, and labeling might interfere with biomolecular function. Effects on molecule structure may be modeled, and wherever possible, appropriate control experiments should be performed to ensure that observed effects are truly biologically relevant. Electron-dense tags might become complementary labels to fluorophores since they could identify particles directly in tomograms. However, they are currently limited by their large size and difficulty to express at high levels.

To enable our vision of fluorescence-guided structure analysis, we aimed to improve both cryo-super-resolution imaging and correlation. Concretely, our aims were laid out as follows: 1) construct a microscope setup compatible with camera-based SMLM and MINFLUX at cryogenic temperature, 2) find suitable fluorophores for cryo-SMLM, enabling high localization precision while providing adequate localization density, 3) optimize cryo-SMLM and cryo-MINFLUX data acquisition, 4) establish a high-accuracy cryo-CLEM workflow. Here, I describe the overall project, which constitutes a collaboration with colleagues in the Danzl and Schur labs at ISTA. My main responsibilities were constructing the setup, super-resolution data acquisition, and data analysis. Colleagues supported me by programming hardware control, preparing samples and acquiring cryo-EM data (see Acknowledgments).

1.3.1 Construction of a cryo-super-resolution microscope setup

I set up a microscope comprising modules for camera-based SMLM, MINFLUX and active sample stabilization, as detailed in Chapter 2. Constructing the instrument ourselves rather than procuring a commercial microscope provided increased flexibility, allowing to adapt to evolving scientific demands. Since not all experimental characteristics were known *a priori*, we modified the setup based on intermediate results. For example, we used an open cryo-stage at the beginning of the project, knowing that this may entail some limitations, and designed the microscope such that different cryo-stage options could be explored straightforwardly. Exchanging the cryo-stage for a sample mounting solution operating at ambient temperature did not entail notable overhead, either. RT measurements were intended for benchmarking setup performance, and directly comparing imaging parameters at RT and cryogenic conditions. Moreover, at the start of the project, very few MINFLUX-setups had existed worldwide. Therefore, we reasoned that having such an instrument available may be useful for other projects and invite collaborations beyond cryo-imaging.

1.3.2 Identification of fluorophores for high-resolution cryo-SMLM

Various fluorophores had been previously tested for cryo-SMLM, but all of them exhibited some limitations. Different studies reported contradictory outcomes (Dahlberg and Moerner, 2021), which might be attributable to different cryo-stages and sample platforms. Therefore, we investigated pertinent cryo-photophysical parameters directly on our setup. We employed test samples as close as possible to the intended application scenario. We started on

fluorophores already published to be photoswitchable at liquid nitrogen temperature, but subsequently explored novel cryo-switching mechanisms as well, for example the photoactivatable PaX-dyes (Lincoln et al., 2022), or photoblueing of organic dyes (Helmerich et al., 2021).

Due to the increased throughput over MINFLUX, initial experiments were performed using camera-based SMLM. The results should inform selection of fluorophores for cryo-MINFLUX. However, cryo-MINFLUX somewhat differs in photophysical requirements. For example, it requires less photons to reach a given localization precision, but demands increased sparsity. MINFLUX is also highly sensitive to the SBR and potentially more affected by fast brightness fluctuations within an emission event. We considered adequate cryo-photophysics characterized with camera-based SMLM a prerequisite for attempting cryo-MINFLUX due to increased experimental complexity and reduced throughput.

1.3.3 Optimizing cryo-SMLM and cryo-MINFLUX data acquisition

To an extent, camera-based SMLM and MINFLUX are complementary cryo-super-resolution techniques. Due to the parallelized localization, camera-based SMLM provides higher throughput, and it had previously been implemented at cryogenic temperatures. Hence, this modality was used for setting up the cryo-workflow and testing photophysics. At the same time, we believe MINFLUX to exhibit interesting features for the adoption at cryogenic temperature.

Enabling MINFLUX imaging on cryo-preserved samples is valuable on its own since at the nanoscale length scales resolved by MINFLUX, artifacts stemming from chemical fixation may affect molecular arrangements. From a different point of view, MINFLUX may be a suitable technique for implementing cryo-super-resolution microscopy due to the photon-efficient 3D localization, the targeted illumination being potentially less prone to devitrification, and localization via excitation patterns rather than emitted light. The last point may seem subtle, but has profound consequences. Besides affecting the response to aberrations, it eliminates, at least to first order, dependence on wavelength, dipole orientation or NA (compare Equation 1.4). Achromatic localization enables precise colocalization of structures, and the implications of localizing fixed dipoles were discussed in Section 1.2.3.4. Of course, NA affects localization through the number of detected photons $N \propto \mathrm{NA}^2$. Taking this into account results in $\sigma \propto \mathrm{NA}^{-1}$ for non-iterative MINFLUX, whereas for camera-based SMLM, the combined effect of the NA on PSF-width and detected photons yields $\sigma \propto \mathrm{NA}^{-2}$.

At the same time, MINFLUX poses elevated requirements on setup and sample for successful adoption at cryogenic temperature. Besides the increased experimental complexity, nanoscale mechanical sample stability in 3D is imperative since *post hoc* drift correction is substantially more difficult than for camera-based SMLM. While requiring fewer photons to reach a given localization precision, the large beam size of MINFLUX imposes a higher sparsity requirement, even though this might be mitigated to some extent by choosing a small pinhole size in confocal detection. As mentioned above, MINFLUX is highly sensitive to background fluorescence. Finally, both MINFLUX and cryo-SMLM are known for low throughput, so combining both may result in very small fields of view being covered within realistic experiment times.

Taken together, in our opinion these factors merit the exploration of cryo-MINFLUX once suitable fluorophores have been identified (see previous section). Even if this proves to be unfeasible or data quality does not justify the additional overhead compared to camera-based

cryo-SMLM, the direct comparison of both approaches will provide valuable insights to the cryo-super-resolution community.

1.3.3.1 Improved mechanical stability for cryo-fluorescence imaging

During initial measurements, we realized that our commercial open cryo-stage did not provide the mechanical stability required for cryo-CLEM at high resolution, in particular using cryo-MINFLUX. Therefore, we adapted a vacuum cryostat for imaging of vitrified samples (Section 3.2). We built on the design published by Hoffman *et al.* (2020), but modified it for our setting. While Hoffman and colleagues combined cryo-SMLM with freeze-substitution and FIB-SEM imaging at RT, we integrated the cryostat in a cryo-CLEM workflow.

Downstream cryo-ET imposes different requirements on samples. For example, ice contamination or devitrification even at small scales can substantially affect data quality. Moreover, EM-grids exhibit notably different optical and thermal properties than the sapphire disks used by Hoffman *et al.* (2020).

Accordingly, we carefully characterized temperature stability, mechanical stability, devitrification and ice contamination associated with imaging in the cryostat to determine its usability for super-resolution cryo-CLEM.

1.3.4 High-accuracy CLEM workflow

Since correlation accuracy limits the spatial scale of CLEM to the same extent as optical resolution, developing a refined correlation workflow is an integral aim of the project. Correlation hinges on successful cryo-SMLM data acquisition. Since this has not been fully achieved, we did not yet implement the correlation approach described here. Other members of the project team are responsible for cryo-ET acquisition, analysis and correlation, such that I hand over samples to colleagues after cryo-super-resolution data acquisition.

For refining image registration locally, our strategy hinges on using ubiquitous *in situ* fiducials, localized in 3D in both datasets. Hoffman *et al.* (2020) achieved 10s on nm correlation accuracy on their workflow entailing freeze-substitution between performing cryo-SMLM and RT-FIB-SEM. We presume that we can achieve increased accuracy when applying *in situ* fiducials in our approach, which should exhibit substantially reduced distortions by performing all imaging steps at cryogenic temperatures.

Additional to cryo-super-resolution microscopy of the target structure, this approach requires imaging of a reference structure showing pronounced features in both modalities at sufficiently high density. Ideally, we would like to achieve this by identifying two distinct fluorophores for labeling molecules of biological interest and fiducial structures (Section 1.3.2). However, in case this is unfeasible, as contingency strategy one may carefully choose distinct structures which are separable based on their shape alone.

2 Construction of an SMLM/MINFLUX Microscope

The aims of the project laid out in the introduction require a super-resolution fluorescence microscope capable of reaching nm-scale localization precision and accuracy. We decided to construct a bespoke setup rather than procuring a commercial system because this approach enabled us to tailor design choices to our needs, and granted a higher level of flexibility for integrating different techniques.

Since the focus of my work was super-resolution imaging at cryogenic temperatures, compatibility with suitable cryo-stages holding samples below the devitrification temperature was imperative to all design choices. Nevertheless, the setup is compatible with camera-based SMLM and MINFLUX imaging at RT. This allowed us to establish the workflow and evaluate various metrics, such as mechanical stability and photophysics, at both RT and cryogenic conditions. Moreover, future projects and collaborations may use this setup for camera-based SMLM or MINFLUX at RT.

This chapter describes the hardware configuration of the microscope as well as proof-of-principle camera-based SMLM and MINFLUX measurements acquired at RT. Cryo-stages and corresponding experiments are discussed in the next chapter.

2.1 Hardware

The microscope was set up on an optical table with passive pneumatic damping. Most of the optics were mounted on a precision-grade optical breadboard ("microscopy breadboard"), which rested on 37.5 mm thick stainless-steel posts placed on the optical table. This configuration allowed for a high level of flexibility at the frontend, comprising tube lens, objective and sample stage. For example, the open cryo-stages we tested required an upright configuration with the objective placed above the sample, while the most straightforward option for integrating the vacuum cryostat was to mount the objective on translation stages in a horizontal orientation (Figure B.2). This section describes the modules for camera-based SMLM (WF module), MINFLUX and active sample stabilization which are outlined in Figure 2.1. For a detailed depiction of the beam path including the part numbers see Appendix B.

2.1.1 Laser module

The excitation lasers were mounted on a breadboard separate from the microscopy breadboard. In this laser module, the beams were spectrally filtered, overlaid and modulated before being coupled into separate optical fibers for WF and MINFLUX excitation. Separating the laser heads from the microscopy breadboard increased laser safety by strongly attenuating the lasers in a contained box. Using the same lasers for WF and MINFLUX excitation was a cost- and space-efficient solution without sacrificing performance, and coupling different lasers into the same optical fiber facilitated co-alignment of different color channels.

The spectra of the excitation laser beams (emitting at 488 nm, 561 nm and 642 nm, respectively) were cleaned up by bandpass filters. Since the 561 nm and 642 nm lasers emitted substantially higher power than needed for our measurements, and their power levels could not be set to arbitrarily small values, parts of their outputs were sent to beam dumps. The dumped fractions could be adjusted by rotating $\lambda/2$ waveplates placed before polarizing beamsplitters (PBS). An acousto-optical modulator allowed for fast power

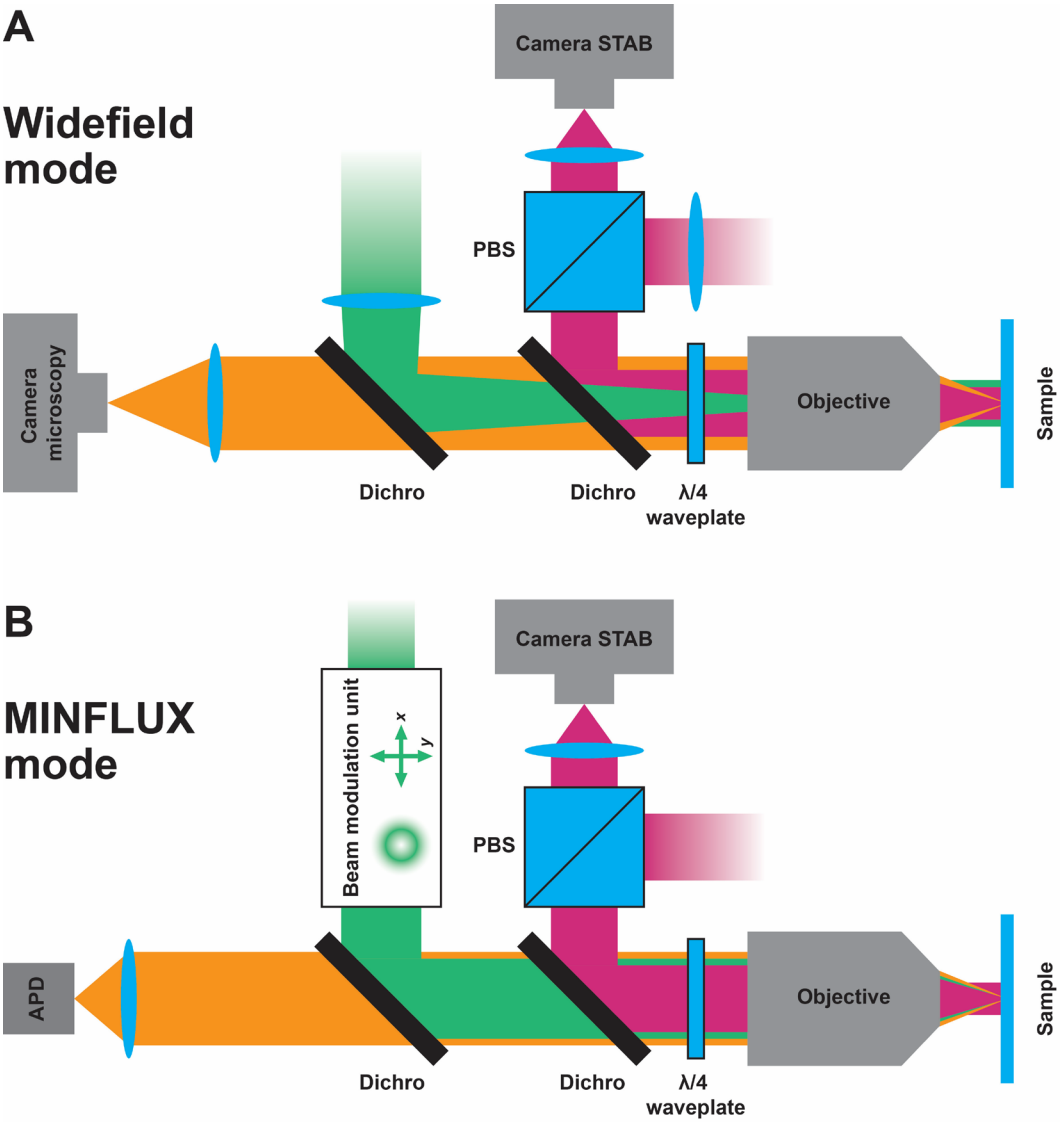

*Figure 2.1: Simplified overview of widefield and MINFLUX modules (extensive schematics of all beam paths in Figure B.1). Light for exciting fluorescence is depicted in green. Fluorescence emitted by the sample is orange. Light for active sample stabilization is magenta. The beam paths are combined via dichroic mirrors ("Dichro"). A λ/4 waveplate generates circular polarization at the sample. The sample stabilization is the same for both modes and comprises a WF imaging path with illumination and detection separated by a polarizing beamsplitter ("PBS"). Light scattered from the sample is detected by "Camera STAB". **A:** In WF mode, the entire field of view is flooded with excitation light, and signal is detected by "Camera microscopy". **B:** For MINFLUX, the "Beam modulation unit" modulates the phase of the beam such that the intensity profile features a deep minimum at the imaging plane in the sample, and the beam is displaced laterally. Signal is detected by an avalanche photodiode ("APD").*

modulation[25]. The 488 nm laser internally contained adequate modulation capabilities and was therefore routed to the fibers directly after adjusting the beam diameter. Due to space constraints, the laser head of the 561 nm laser and its attenuation unit were placed on a different breadboard and coupled into a polarization-maintaining optical fiber before being combined with the 642 nm beam.

[25] Currently, both lasers are modulated by a single acousto-optic modulator after combing the beams. Hence, for the measurements performed so far, only one laser was switched on at a time. Using separate modulators for the beams would allow for interleaved multi-color measurements.

After combining all beams via longpass dichroic mirrors, a Glan-Thompson polarizer generated linear polarization with a high extinction ratio before directing the beams to a polarization-maintaining optical fiber. Switching between respective fibers for WF and MINFLUX excitation was performed by changing the position of a motorized flip mirror. Due to substantially different excitation laser powers commonly used in camera-based SMLM and MINFLUX, I placed a neutral density filter with a nominal optical density of 2 before the MINFLUX-fiber. Additionally, fast switching between different illumination paths for MINFLUX via electro-optical modulators was planned but not fully implemented.

The 405 nm activation laser came with a fiber coupling unit attached to the laser head, so the fiber output was placed directly on the microscopy breadboard. A motorized flip mirror switched between imaging paths for WF and focused activation.

2.1.2 Widefield module

When designing the microscope, our main focus was the construction of a high-performance MINFLUX imaging path. Still, WF-imaging – specifically in conjunction with camera-based SMLM – is an important part of the setup, used for assessing the quality of stainings as well as the photophysics of fluorophores, and constituted a super-resolution imaging setup. The WF module is laid out in Figure 2.1A, Figure B.1 shows the full beam path.

After exiting the WF-fiber leading to the microscopy breadboard, the excitation laser beam for WF imaging was collimated and combined with the activation laser beam via a dichroic mirror. To generate homogeneous illumination over as large an area as possible at the sample, the beam diameter was chosen to fill the 25 mm apertures of the lenses used. After passing a lens that was positioned such that it focused the illumination at the back focal plane of the objective, the (vertically polarized) beam was reflected by a PBS[26]. The PBS combined WF with the (horizontally polarized) MINFLUX illumination path, which was transmitted. The beams were then reflected by a multipass dichroic mirror, which separated fluorescence excitation and emission light. They subsequently passed a tip/tilt piezo mirror, which remained in a static position for WF imaging, and corresponding relay optics (Section 2.1.3). A shortpass dichroic mirror overlaid the light of the active stabilization module (Section 2.1.4). A $\lambda/4$ waveplate before the objective generated circular polarized light at the sample[27]. Modeling fluorophores as dipoles, their absorption cross-section depends on the angle between the electric field of the excitation light and the dipole axis. Hence, circular polarization excites all orientations effectively.

When imaging close to the coverslip, it may be advantageous to suppress background by limiting the penetration depth of excitation light. This can be achieved by offsetting the beam from the optical axis at the back focal plane of the objective, thereby creating highly inclined illumination in the sample or total internal reflection at the coverslip. The setup was not

[26] Some of the components employed here, such as waveplates, dichroic mirrors and PBSs, were designed for collimated light. Hence, they may induce aberrations in a converging or diverging beam passing through them. However, this design criterion cannot be fulfilled simultaneously for WF illumination and light originating from a point-like emitter in the sample. Since aberrations in the emission path directly affect image quality, we opted to compromise on the side of the WF illumination. This configuration also avoided aberrations of the MINFLUX excitation, where the beam shape is critical. I did not observe notable aberrations to WF illumination either, potentially because the convergence angle was relatively small.

[27] Circular polarization is also instrumental for generating vortex beams with a deep intensity minimum. Therefore, the polarization was adjusted for the MINFLUX-path (Figure B.1). The WF excitation may deviate slightly from perfect circular polarization, but this should not have a substantial impact on imaging performance.

designed to allow for precise alignment of beam offsets, but I observed that background could still be suppressed by tilting the excitation beam via mirrors placed after the collimation lens.

The light emitted by the sample was collected by the same objective used for illumination, and shared the same beam path up to the multipass dichroic mirror, where it was transmitted. A motorized flip mirror inserted into the beam path directed the emitted light to an sCMOS camera. Optical filters blocked activation and excitation light[28] as well as near-infrared light of the active stabilization module. Using a motorized filter wheel to change between color channels proved to be helpful for changing filters without having to open the box of the setup which may induce drifts (Section 2.2).

Finally, an achromatic doublet lens focused the light onto the camera chip. The magnification was chosen such that the pixel size corresponded to 53 nm in the sample plane for the used 100x/1.45 oil objective, 60 nm for the 100x/0.75 air objective and 100 nm for the 63x/0.75 air objective with correction collar. The field of view was limited by the 25 mm aperture of the last lens before the camera to a circle with a diameter of roughly 55-60 µm at the sample for the 100x objectives and 100 µm for the 63x objective. I tested a lens with a larger aperture which increased the field of view but induced aberrations. Therefore, I decided to keep using the lens with the smaller 25 mm aperture.

For 3D localization using astigmatism, a cylindrical lens unit was inserted before the flip mirror. The unit was adapted from Power (2024), and comprised a convex and a concave cylindrical lens with equal magnitudes of focal length rotated against each other. The degree of astigmatism was set by the rotation angle.

2.1.3 MINFLUX module

To a large extent, the design of our MINFLUX module (laid out in Figure 2.1B, see Figure B.1 for full beam path) is based on the setup published by Gwosch *et al.* (2020). A major difference is our frontend, which could be equipped with a cryo-stage.

After exiting the MINFLUX-fiber leading to the microscopy breadboard, the excitation laser beam for MINFLUX imaging was collimated and passed through a “beam modulation unit”, which generated the TCP. First, an SLM generated a suitable beam shape by imprinting a spatially controllable phase shift on the wavefront. By default, we used a first-order vortex (“doughnut”) beam. Additionally, common aberrations (astigmatism, coma, spherical, trefoil) were manually pre-compensated at the SLM. A blazed grating, added to the phase pattern, separated phase-modulated from directly reflected light, eliminated artifacts originating from diffraction at the pixel-boundaries of the SLM, and allowed for fine-grained beam shifting. The SLM was controlled via a software application running on the microscope control PC written by Wiebke Jahr in the Danzl lab (https://github.com/danzllab/SLMcontrol).

Two electro-optical deflectors (EODs) displaced the beam along x and y over a small range (hundreds of nm in the sample) with fast response time (few µs)[29,30]. Since EODs are

[28] When imaging light scattered by the sample, for example gold beads, the filter was removed. Most of the light was reflected by the multipass dichroic mirror, but the transmitted fraction was still sufficiently high.

[29] Between the SLM and the first EOD, the beam was demagnified to a diameter smaller than the aperture of the EODs to prevent aberrations. Due to space constraints and the requirement for the SLM as well as both EODs to be placed in conjugate planes to the back focal plane of the objective, this was performed via two telescopes, one of which contained a concave lens.

[30] Before the first EOD, a 50:50 beamsplitter was intended to combine the beam path with another fiber output, which might be used to rapidly switch between Gaussian and phase-modulated excitation. The Gaussian beam path was not fully implemented because thus far none of our measurements required this functionality.

polarization-sensitive[31], the beam was linearly polarized before the first EOD, and a λ/2 waveplate turned the polarization by 90° between the two EODs. The beam then passed through a PBS, which overlaid it with the WF illumination (Section 2.1.2), and was reflected at a multipass dichroic mirror.

A tip/tilt piezo mirror placed conjugate to the back focal plane of the objective allowed for positioning of the beam across a larger range (tens of µm in the sample), albeit at lower speed. We used the tip/tilt mirror either to scan across the sample or to target regions of interest (ROIs) for MINFLUX measurements. Scanning over sparse, point-like emitters, such as beads immobilized on a coverslip, was useful for inspecting and adjusting the beam shape at the sample plane. Additionally, when used with a Gaussian illumination profile, this mode enabled confocal measurements. However, while the tip/tilt mirror provided excellent static stability, the scan speed was very slow compared to typical confocal systems using galvo-mirrors, and the scans exhibited some distortions[32].

A λ/4 waveplate placed before the objective generated circular polarization at the back focal plane of the objective. The polarization state was important for MINFLUX using doughnut beams since – particularly for high-NA objectives – the production of a deep intensity minimum in the beam center requires that the handedness of the polarization is the same as the helical phase pattern projected on the SLM.

Light emitted by the sample was collected by the same objective used for illumination and shared the same beam path up to the multipass dichroic mirror, where the emission was transmitted. With the motorized flip mirror in the detection moved out of the beam path, the light was then focused on a motorized pinhole wheel. Adjusting the pinhole size allowed for flexibility regarding different objectives, sample types and imaging applications. Finally, single-photon counting modules detected the signal. The setup contained two detectors with optical bandpass filters placed in front of them, separated by a longpass dichroic mirror. This configuration allowed for multi-color imaging[33].

The acquisitions were controlled by an instrument control PC, which was connected to some of the devices via serial ports. Other devices directly received or generated analog or digital signals, which were processed by an analog/digital input-output module or a field-programmable gate array (FPGA). The FPGA was programmed by Marek Šuplata in the Danzl lab in LabView, which provided an interface to a graphical user interface (GUI) written in C#[34]. The latest version contained non-iterative MINFLUX functionality with a TCP comprising 3+1 positions, as initially demonstrated by Balzarotti *et al.* (2017)[35].

[31] The polarization-sensitivity, together with high coupling losses, was why the EODs were not descanned. Due to the small deflection range, the excitation pattern still did not get offset too much from the pinhole.

[32] Speed would be increased by using a smaller mirror, and image distortions may be avoided by applying more advanced signal processing schemes.

[33] While not used here, multi-color MINFLUX using a single excitation beam and ratiometric detection would be highly suited for virtually bias-free colocalization measurements (Gwosch et al., 2020).

[34] In the GUI, most of the device settings could be adjusted, and parameters set for scanning/confocal acquisitions or MINFLUX acquisitions. The software currently allows for acquiring scanning measurements to select an ROI for subsequent MINFLUX imaging. After activating the MINFLUX mode, the software has to be restarted to acquire more scanning measurements.

[35] Extensions for iterative and three-dimensional MINFLUX (Gwosch et al., 2020) were planned but not implemented. A scheme for conditionally switching on the activation laser when no fluorophore emission was detected was devised, but final debugging and testing were not performed due to other priorities. Accordingly, it was not used.

2.1.4 Active stabilization module

The scheme described in this section was published as peer-reviewed article (Vorlaufer et al., 2025), which is reproduced in Appendix A. This section gives an overview of the implementation in our microscopy setup.

The point-scanning implementation of MINFLUX makes *post hoc* drift correction challenging. Therefore, all MINFLUX-setups published so far contained a module for active sample stabilization in 3D. However, these modules measured axial displacements via the position of an off-axis laser beam reflected at the coverslip (Balzarotti et al., 2017; Geismann et al., 2024) which would limit the applicability for cryogenic imaging. Therefore, we developed a novel, purely image-based scheme.

During stabilization measurements, "reference structures" in highly stable spatial relation to the sample were tracked to iteratively estimate and compensate displacements (Figure 2.2). Reference structures were illuminated with a near-infrared LED emitting around 940 nm to not interfere with microscopy data acquisition. LED emission was spectrally filtered and vertically polarized before being reflected at a PBS and combined with the microscopy path via a shortpass dichroic mirror after the tip/tilt mirror (Figure 2.1)[36]. Light scattered at the sample arrived at the PBS with horizontal polarization, and was hence transmitted before forming an image at the stabilization camera. This polarization-selective arrangement suppressed background originating from reflections at optical components along the beam path.

Directly before engaging the stabilization, a reference stack was acquired for every axis by moving the sample stage over a user-defined range around the setpoint (Figure 2.2A). Displacements were then estimated by comparing the latest camera frame acquired in a stabilization measurement to all frames in the respective reference stacks. In the lateral plane, this was performed via image cross-correlation. Along the optical axis, cross-correlation did not provide the desired precision, or resulted in strong cross-talks to the other axes when astigmatism was induced at the stabilization camera. Therefore, we used a different approach: The distribution of normalized pixel intensity values changed depending on the level of defocus (Figure 2.2B). Calculating the mean-squared error between the pixel intensity curves of the latest frame and all entries of the *z*-reference stack hence resulted in a dip, whose center position indicated displacements of the sample along the optical axis.

Drift correction was performed in a closed-loop configuration by iteratively estimating displacements as described above, and using this information to compensate for them by moving the piezo sample stage. We chose proportional-integral feedback with a small amount of second-order integrator (i.e., summing the summed displacements) added to effectively compensate strong, continuous drifts, arising, e.g., due to fluctuations of the laboratory temperature (see next section).

[36] This position was chosen because it covered as much as possible of the microscopy path without the active stabilization being affected by movements of the tip/tilt mirror.

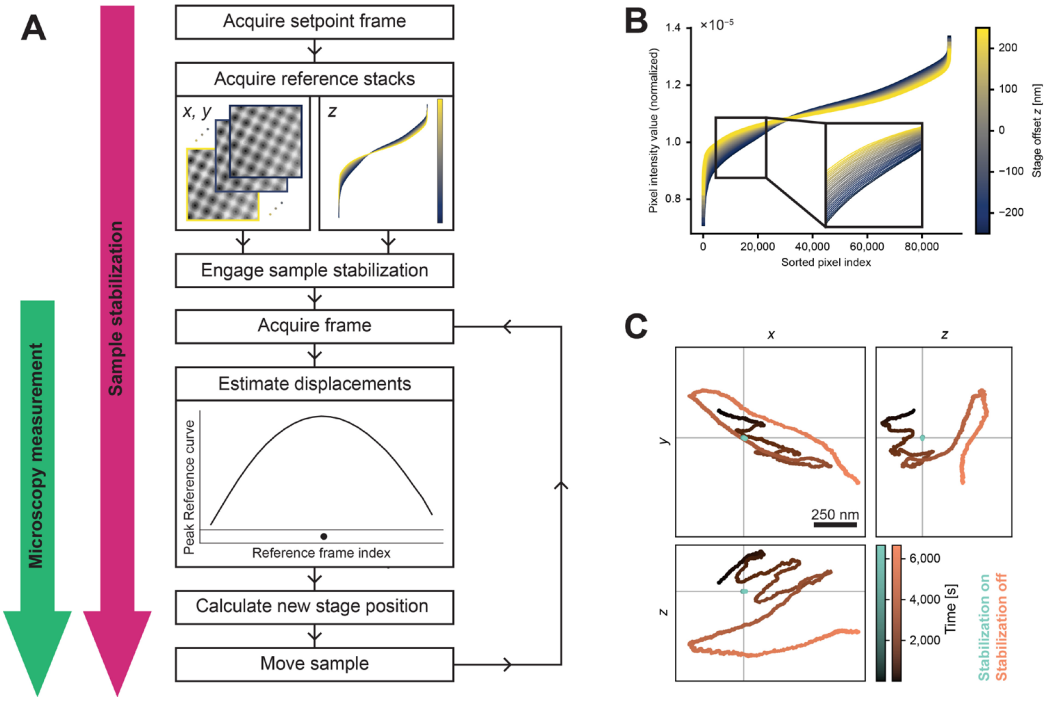

Figure 2.2: Overview of the active stabilization module. Panels and corresponding captions were reproduced from (Vorlaufer et al., 2025) under CC BY license. ***A:*** *Stabilization workflow. After choosing an ROI and acquisition of reference stacks the scheme estimates displacements in each iteration of the active feedback loop by comparing camera frames against the reference stacks and actuates on sample position. Microscopy measurements are started once feedback is engaged (indicated by arrows left of the workflow diagram).* ***B:*** *Normalized pixel intensity as a function of intensity-sorted pixel index for each frame (color coded) of the reference stack along the z direction. Enlarged view of the data in A. Curves for the individual frames of the reference stack (spaced 20 nm along z) can be discerned as separate lines in the magnified view.* ***C:*** *Position of an individual gold bead on a coverslip over time with and without sample stabilization, tracked in the microscopy path for 1 h 51 min. For stabilization of sample position, a distinct set of gold beads on the same coverslip was used in the stabilization path.*

2.2 Setup stability

The mechanical stability of microscope setups can substantially affect their imaging performance. In particular, stability becomes a crucial concern for many super-resolution microscopy approaches due to the combination of extended acquisition times and high spatial resolution. Depending on the time-scale of movements and the acquisition mode, insufficient mechanical instability can reduce the resolution or distort reconstructed arrangements. Instability can present itself as periodic variations, arising, for example, from vibrations of the laboratory building or fans of devices in proximity to the setup, or continuous drifts, for example due to temperature changes or mechanical relaxation.

I investigated mechanical vibrations using piezo-electric acceleration sensors. Vibrations at the frontend were slightly elevated compared to the optical table with a peak around 230 Hz. Adding weight to the breadboard on which the frontend was placed reduced the amplitude to the nm-scale.

To analyze the extent of sample drifts, I tracked the peak position of a gold bead immobilized on a coverslip, imaged in WF mode (Figure 2.3A). After allowing ample time (up to a full day) for mechanical relaxation and thermal equilibration, the bead position reached

a steady state where it oscillated regularly[37] with a period of approximately 40 min and an amplitude of ~1 µm.

The oscillations of the sample position were highly correlated with periodic fluctuations of the laboratory temperature (Figure 2.3A). Further investigations indicated that the oscillations were caused by the air conditioning unit, which was not designed for the temperature stability required for our experiments[38,39]. The most pragmatic solution turned out to be switching off the air conditioning in the cubicle where the setup was placed, while keeping it activated in the rest of the laboratory. Moreover, I reduced the sensitivity to fluctuations of the laboratory temperature by placing thermally insulating extruded polystyrene panels around the setup. I also reduced the thermal load on the setup by placing devices with high power consumption outside the cubicle or on elevated positions whenever possible. These measures resulted in very strong drifts directly after switching on the equipment, but within ca. 24 h, the temperature was equilibrated, and the setup was more stable than with air conditioning switched on inside the cubicle. Sample drifts were still apparent, but they were effectively corrected by the active stabilization module (Section 2.1.4). As shown in Figure 2.3B, the residual deviations of the sample position ("error signals") remained within the nm-range.

However, the active stabilization module did not cover the entire beam path. Therefore, drifts in other parts of the setup may still adversely affect performance. In MINFLUX, emitter coordinates are determined from relative distances between excitation beam and emitter. Therefore, uncorrected beam drifts lead to artifacts[40]. To evaluate beam drifts, I tracked the position of the MINFLUX excitation beam with a camera inserted in front of the tube lens (Figure 2.3C). Similar to the measurements of the sample position, oscillatory movements were apparent. The amplitude of the beam oscillations was roughly 5 µm peak to peak before the tube lens, corresponding to 45 nm in the sample plane (using the nominal demagnification of 111x). I acquired a MINFLUX measurement on a gold bead immobilized on a coverslip (Figure 2.3D). Even though the active stabilization module effectively corrected sample drifts, the reconstructed position of the bead oscillated. Since I confirmed in WF measurements that the beads were rigidly immobilized on the coverslip, it stands to reason that the observed oscillations were due to drifts of the excitation beam. Without pertinent correction schemes, these drifts would lead to inaccurate MINFLUX localization.

The level of temperature stability and associated microscope drifts varied notably between different days. While the data in Figure 2.3C-D are discouraging for high-resolution MINFLUX measurements, Figure 2.5 shows that on a different day, the stability was sufficient to obtain nanoscale resolution. This arrangement was acceptable for proof-of-principle demonstrations of MINFLUX on *a priori* known structures, but will likely limit reproducibility and hamper the utility for routine measurements. Improving thermal insulation of the setup may further reduce drifts, but it is unclear whether this alone will provide sufficient stability levels for

[37] For the measurement shown here, beads were localized only in the lateral plane, but corresponding oscillations of the focus position were apparent by eye in the raw data as well.

[38] The temperature sensitivity of the setup may be aggravated by the construction as an upright microscope placed on a breadboard not directly connected to the sample stage. This design choice allowed for cryo-imaging with commercial cryo-stages, but other arrangements may have resulted in smaller sample drifts.

[39] Together with our in-house technicians responsible for heating, ventilation and air conditioning, I undertook multiple attempts to improve the temperature stability beyond the specified precision of the air conditioning unit (±1 °C), but they were not successful.

[40] The same is true for drifts in the detection path of camera-based SMLM not covered by the active stabilization module, but these drifts can often be corrected after the acquisition.

reliable nm-scale imaging. Exchanging the air conditioning unit would entail extensive construction work in the laboratory but may ultimately be necessary to provide an environment where MINFLUX can reach its full potential. Finally, residual beam drifts could be corrected by modifying MINFLUX acquisition workflows – either in post-processing as is done in the Abberior MINFLUX, or stabilizing beam position in a closed-loop implementation.

2.3 Camera-based single-molecule localization microscopy

As mentioned above, camera-based SMLM measurements at RT were performed predominantly to characterize the setup performance and compare datasets to samples imaged with MINFLUX or at cryogenic temperatures. This is reflected in the samples shown here, with DNA-origami structures and nuclear pores being established reference structures for super-resolution microscopy, and photoactivatable dyes being potentially interesting for cryo-SMLM. The sample preparation protocols for all samples can be found in Appendix C.

DNA-origami comprise synthetic DNA-strands whose shape is determined by their sequence. Thus, they allow for the design of well-defined, bespoke structures which is attractive for benchmarking the resolving power of microscope setups. We used commercial origami-structures ("nanorods"), containing three binding sites for DNA-PAINT imager strands, separated by 40 nm each, arranged along a line. The single-molecule reconstructions (Figure 2.4A) indicated that the binding sites were clearly resolved and the distance between peaks was in line with the design specifications. Data quality might be affected by background from diffusing imager strands and residual drifts[41].

While synthetic structures are useful for benchmarking, biological samples represent a slightly different environment. For example, background may be elevated, fluorophores can bind to other biomolecules than intended, and chemical fixation might distort structures. Therefore, it is important to test imaging on biological samples. The nuclear pore complex has been established as a reference structure for SMLM because it contains distinct structural features at length scales amenable to super-resolution microscopy (Thevathasan et al., 2019). We obtained a previously established cell line, which had mEGFP fused to Nup96, expressed at endogenous levels (Thevathasan et al., 2019). Nup96 is arranged along a ring-like structure with eightfold symmetry in the nuclear pore complex. We labeled the structure with fluorophore-conjugated nanobodies binding to mEGFP to keep the offset between localized fluorophores and Nup96-proteins small. The dSTORM reconstructions (Figure 2.4B) reproduced the expected arrangement to a large extent. However, the data displayed some bright clusters, and not all rings had exactly 8 subunits. While this might reflect biological variability to some extent, it could also indicate artifacts due to the sample treatment prior to imaging, and labeling imperfections. Moreover, more fluorophores might potentially be activated by extending acquisition times and adapting the activation scheme[42].

[41] Active stabilization was enabled, but the second-order integrator (Section 2.1.4) had not been implemented at the time of this measurement. This led to sub-optimal performance and residual drifts of ca. 100 nm which were corrected *post hoc* using cross-correlation.

[42] We used activation pulses with constant intensity and duration throughout the acquisition. However, it has been shown to be advantageous to increase these parameters in the course of an SMLM measurement to counteract the decreasing number of activated fluorophores over time (Štefko et al., 2018).

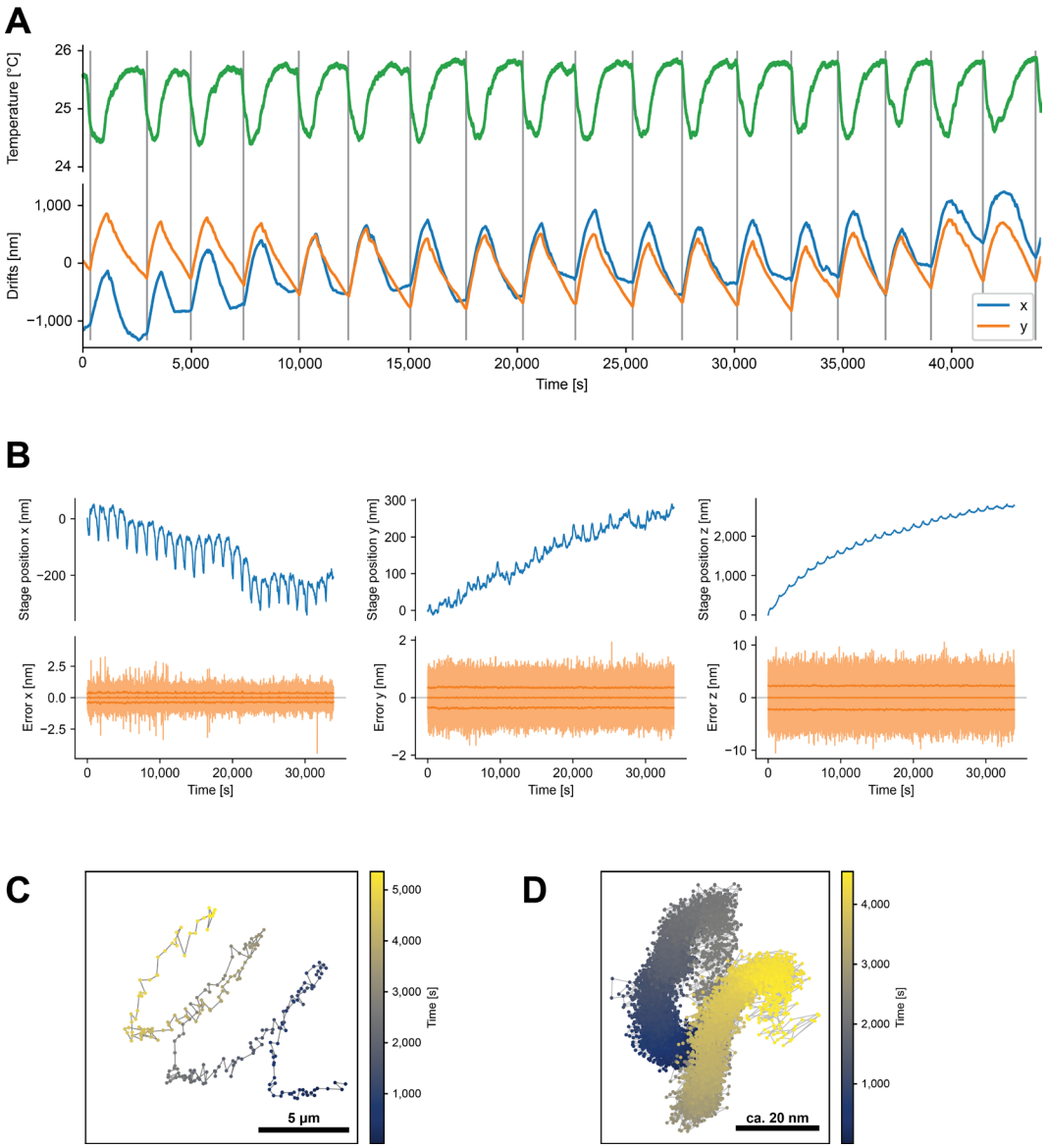

Figure 2.3: Mechanical stability of the microscope. ***A:*** *Laboratory temperature (green curve) and peak coordinates of an immobilized gold bead, tracked overnight. The temperature sensor was placed behind the sample stage. Ample time was allowed for thermal equilibration between switching on the equipment and starting data acquisition. Vertical grey lines were placed manually at time points when the y-coordinate reached a local minimum. Slight dephasing between temperature drops and sample drifts was presumably caused by imperfect synchronization between temperature sensor and camera acquisition.* ***B:*** *Active sample stabilization effectively compensated drifts in 3D. The piezo stage (blue curves) was moved such that the errors (deviations of sample position from the setpoint, orange curves) remained close to 0. The data include the equilibration phase, where drifts along the optical axis were substantial. Panels reproduced from (Vorlaufer et al., 2025) under CC BY license.* ***C:*** *Peak position of the MINFLUX excitation beam over time. Beam was detected by a camera inserted in the beam path in front of the tube lens. Beam profile was set to Gaussian at the SLM to facilitate straightforward determination of the center coordinates.* ***D:*** *MINFLUX imaging of an immobilized gold bead. A different set of gold beads on the coverslip was used to compensate sample drifts with nm-scale precision[43]. The bead was manually centered on the target coordinate pattern. Localizations may be biased since background was unknown.*

[43] At the time of this measurement, the latest version of the active stabilization scheme had not yet been developed. Hence, axial stabilization precision was worse, but this should not have affected the 2D MINFLUX measurement shown here.

Both PAINT and dSTORM rely to a large extent on spontaneous on- and off-switching of signal[44]. For some applications, increased optical control can be useful or even required. Photoactivatable fluorophores can provide increased control because the wavelength used to excite fluorescence only bleaches fluorophores and does not switch them on to a notable extent. Activation pulses of a different wavelength put new fluorophores in an emissive state once most of the previously activated fluorophores have switched off. Tuning excitation and activation intensities as well as duration and repetition rate of activation pulses provides options for optical control of fluorophore states. Since fluorescent proteins typically do not reach the photophysical performance of modern organic dyes (as discussed in Section 1.2.3.2), we tested the previously published photoactivatable dye PaX560 (Lincoln et al., 2022).

We obtained the fluorophore conjugated to phalloidin, which binds to actin filaments, from the authors. Actin filaments are a challenging yet interesting target for SMLM because they are densely distributed across many cell types and form distinct cytoskeletal structures, such as focal adhesions, stress fibers, lamellipodia and filopodia. First, I tested photoactivation at the ensemble level on a confocal microscope (Figure 2.4C). To prevent spontaneous activation by ambient light, samples were prepared under red light and shielded during imaging. ROIs were identified based on signal in the far-red channel, stemming from Alexa Fluor Plus (AFP) 647 conjugated to phalloidin, co-stained with PaX560-phalloidin. A scan with 560 nm excitation was acquired to determine the background comprising autofluorescence and pre-activated dye molecules. Subsequently, a scan with 405 nm activated the PaX560 fluorophores, which were detected during a final scan with 560 nm excitation. As expected, the signal increased strongly between the two scans with 560 nm excitation (44-fold[45] for the measurement shown here, measured as summed photon counts). The overlay with the far-red channel confirmed that the signals largely coincided, indicating that the photoactivatable dye was bound to actin filaments as expected. Slightly different intensity levels in some parts of the cell can be explained by different hydrophilicities of PaX560 and AFP647.

After confirming the photoactivation and subcellular localization of PaX560, I set out to evaluate the performance of the dye for single-molecule imaging on our homebuilt setup, using the same samples co-stained with AFP647-phalloidin and PaX560-phalloidin. Low-intensity pulses of 405 nm light activated a small subset of fluorophores, which were detected by 561 nm illumination. Since the aim of this measurement was to evaluate the general performance of PaX560, no reference structures for active stabilization were added. Hence, drifts limited the viable acquisition time, and the localization density was not high enough to observe many of the fine arrangements typically present in dense actin networks. Still, on a larger scale, the reconstruction faithfully showed structures like stress fibers, filopodia and focal adhesions at the locations indicated in the far-red channel (Figure 2.4D). Besides photoactivation, the raw data also showed an unexpectedly high level of blinking at time points when activation light was not present. Presumably, this can be attributed to photoblueing of AFP647 molecules (Helmerich et al., 2021) since a control experiment using cells stained only with AFP647-phalloidin showed comparable levels of blinking using the same spectral windows for excitation and detection. Therefore, the reconstruction in Figure 2.4D presumably comprises emission events of both PaX560 and AFP647. Further

[44] In dSTORM, activation can be facilitated via activation pulses using blue or violet light, but ultimately, the technique relies on spontaneous blinking.

[45] Since the scan before activation was dominated by noise, this is a conservative estimate.

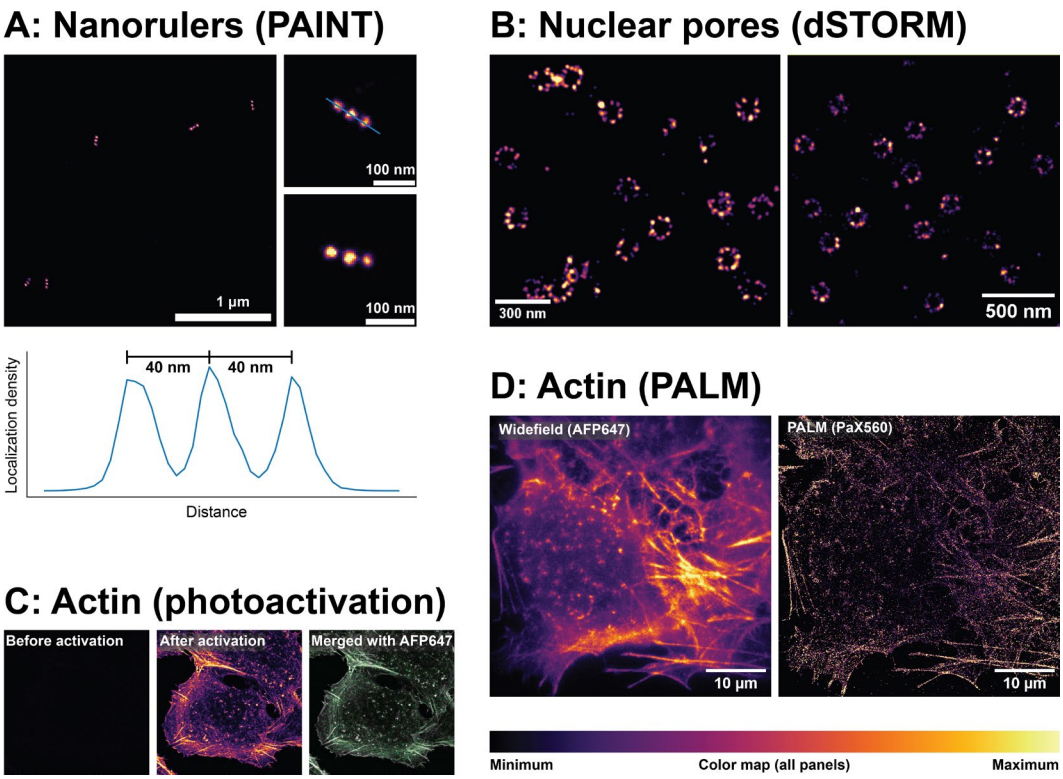

Figure 2.4: Widefield-SMLM example measurements. ***A:*** *DNA-origami nanorulers with 3 binding sites for DNA-PAINT, separated by 40 nm each, allowed for benchmarking of the microscope. Bottom: Line profile of the nanoruler shown in the top right panel.* ***B:*** *Nanobody-tagged Nup96-mEGFP showing ring-like structures with eightfold symmetry, imaged via dSTORM. The panels represent two biological replicates. Right panel reproduced from (Vorlaufer et al., 2025) under CC BY license.* ***C:*** *Confocal scans showing the photoactivation of PaX560 bound to actin filaments. Between left and central panel, a scan with 405 nm illumination activated fluorophores. Right: Overlay of the activated PaX560-phalloidin (green) with co-stained AFP647-phalloidin (magenta), showing the colocalization of the dyes.* ***D:*** *PALM measurement (right panel) of PaX560 and WF measurement of AFP647 (left panel) of the same region. As described in the main text, PALM data were presumably affected by photoblueing of AFP647 molecules. Except for the left panel in D, all color maps start at signal levels of 0.*

experiments will be needed staining only with PaX560-phalloidin [46] to comprehensively evaluate the performance of PaX560 for SMLM. Still, the insights gained so far are interesting since photoblueing itself might be a useful switching pathway for (cryo-)SMLM.

2.4 MINFLUX imaging

While one of the aims set out at the start of this project was performing MINFLUX at cryogenic temperatures, establishing a MINFLUX acquisition workflow for measurements at RT constituted a considerable effort in itself. We implemented a basic version of non-iterative 2D MINFLUX with a smaller degree of automation than, e.g., the commercial version of MINFLUX (Schmidt et al., 2021). This allowed us to generate proof-of-principle data on synthetic test samples, but increasing throughput to reasonable levels and enabling a wider range of applications will require modifications of the workflow, in particular on the side of

[46] Co-staining with other dyes would be useful to identify ROIs but might be challenging. Blue-shifted dyes could contribute to background during PALM imaging of PaX560 via anti-stokes excitation, or their excitation wavelength might pre-activate PaX560 molecules. Potentially, it would be advantageous to co-stain with a dye emitting in the same color channel and bleach it before PALM similarly to Lincoln *et al.* (2022). It might also be possible to bleach AFP647 before PALM to eliminate photoblueing during the measurements, but this would have to be carefully evaluated.

hardware control. I created a custom software package for processing MINFLUX count traces (see Section 2.4.1), adapting a modified version of the framework laid out in the Supplementary Information of Balzarotti *et al.* (2017).

Microscopy measurements typically start by identifying an ROI and placing it in the field of view. This is a trivial step for many microscopy techniques, but in our MINFLUX workflow, it turned out to be challenging for single-molecule switching samples. Bead samples, on the other hand, allowed for convenient positioning of the TCP by first identifying an isolated bead in scanning mode, then switching to MINFLUX, and moving the piezo stage or the tip/tilt mirror to a position where the count rate of the central exposure was minimized, while the other TCP positions exhibited similar intensity levels. Then, active sample stabilization could be engaged and a "technical" MINFLUX measurement started. This was useful for characterizing different properties of the MINFLUX module, such as mechanical stability (Figure 2.3D), or calibrations of the tip/tilt mirror and the EODs.

Using MINFLUX for nanoscale imaging requires fluorophores switching on and off stochastically at the single-molecule level. The same photoswitching pathways used for dSTORM have been used in previous demonstrations of MINFLUX (Balzarotti et al., 2017; Gwosch et al., 2020). Since emitters are in an emissive state before the start of a dSTORM measurement, we envisioned that we could use an analogous positioning scheme as described above for beads, then put the fluorophores in a dark state, and start MINFLUX. We tested this using DNA-origami structures, but in our hands, they bleached before we could center the TCP, and reconstructions did not look promising in either MINFLUX or camera-based SMLM.

We also tried imaging the Nup96-tagged cells described in Section 2.3 with MINFLUX, using a dSTORM-type single-molecule switching scheme. The reconstructions revealed clusters, but it remained inconclusive to which extent these represented the expected ring-like arrangements of Nup96. Since the ring diameter of approximately 108 nm (Wang et al., 2023) was not much smaller than reasonable sizes of the TCP, the precision of manual TCP-centering may have been insufficient to position an entire nuclear pore within the field of view of MINFLUX. Without iterative MINFLUX, targeting adjacent positions would require a relatively small step size to obtain continuous coverage over larger sample areas. This may lead to substantial bleaching of regions before they would reach the central region of the TCP[47]. Moreover, extended acquisition times would increase the impact of beam drifts (Section 2.2).

While it may be worthwhile to revisit this sample type once pertinent acquisition schemes have been implemented, we sought for a suitable test sample for proof-of-principle MINFLUX measurements using the current version of the setup. Out of the samples we tested, DNA-origami structures in conjunction with DNA-PAINT were most amenable. Origamis are available in sizes smaller than reasonable TCPs for non-iterative MINFLUX, and their concentration on coverslips could be easily tuned to levels where most of the time, only one origami was within the field of view of MINFLUX. Observed PAINT emission events were brighter, lasted longer, and flickered less compared to dSTORM events. These characteristics facilitated manual centering of TCPs on origamis based on the real-time observation of photon count traces, even though this was still a challenging, imprecise procedure.

We purchased origamis with binding sites for imager strands arranged in a 4x4 grid separated by 18.0 and 21.8 nm along orthogonal directions (Figure 2.5C, top left panel).

[47] In MINFLUX, average intensities are highest in the periphery of TCPs. Compared to the implementation by Gwosch *et al.* (2020), bleaching would be aggravated for our acquisitions with the current version of our setup since the lack of a working scheme for conditional activation necessitates increased excitation laser power and extended acquisition times.

Camera-based PAINT reconstructions (Figure 2.5C) reflected the expected arrangement to a large extent. Some binding sites remained dark in all observed origami-grids. Subsequent MINFLUX measurements on the same coverslip sometimes reproduced grid-like structures to some extent (Figure 2.5D), even though a lower fraction of binding sites was retrieved. At least in part, this can be attributed to imperfect centering of origamis on the TCP. However, reduced localization density of MINFLUX data has been discussed in other publications as well (Gwosch et al., 2023; Prakash and Curd, 2023). Due to the low throughput[48], it would require more effort to sample a sufficiently high number of origamis for a more comprehensive analysis of MINFLUX data quality.

A key feature of MINFLUX is the high photon efficiency, i.e., comparatively few photons are required to achieve a given localization precision. The highest possible localization precision of an unbiased position estimator is given by the Cramér-Rao bound. For the measurement parameters used here, this results in achievable standard deviations of σ_{crb} = 3.4 nm/3.0 nm (reconstructions shown in left/right column of Figure 2.5D) for N = 1000 detected photons and σ_{crb} = 1.5 nm (same for both datasets) for n = 4000 at the center of the TCP, taking the experimentally determined SBRs (around 1.2) into account. In the data, the respective clusters closest to the TCP center exhibited widths of σ_{peak} = 3.7 nm/3.9 nm (again, left/right datasets) for N = 1000 and σ_{peak} = 2.0 nm (same for both datasets) for N = 4000. Experimental values were derived from the full width at half maximum read out from line profiles of the reconstruction. The experimental precision came close to the conceptual limit, with residual deviations being attributable to offsets of the clusters from the TCP center and potentially also to beam drifts during acquisitions. Where possible, I also measured the distance between clusters and found them to be in line with the specifications of the DNA-origami grids.

In summary, we demonstrated that our setup is compatible with proof-of-principle MINFLUX acquisitions on simple test samples, where we came close to the expected localization precision. However, data quality was compromised by a comparatively low retrieval of binding sites in the reconstructions which needs further investigation. Improvements to data acquisition schemes, hardware control and sample preparation are expected to improve quality and reproducibility of reconstructions, and enable more advanced measurement settings.

2.4.1 Data analysis

MINFLUX data were processed by a self-written Python software package, which is fully documented and open source: https://github.com/danzllab/minflux-analysis. The software comprises functionality for localization, visualization and analysis. It is currently designed for the type of proof-of-principle data generated as described above, but is fully modular and object-oriented, such that it provides a suitable basis for future extensions.

In a first step, emission events were extracted from raw MINFLUX count traces (Figure 2.5A). To this end, noise was removed from count traces via low-pass filtering. Single-molecule emission events were then extracted from filtered count traces based on user-defined intensity levels (lower and upper thresholds to remove time points with either background or multiple active emitters), on-times (to remove bright but short events, arising, e.g., in PAINT from imager strands diffusing through the field of view) and ratio of counts in the central exposure (to remove localizations with excessively high counts in their central

[48] The two datasets shown here were the only usable output of a full day of measurements.

exposure; mostly useful for iterative MINFLUX (Gwosch et al., 2020)). Additionally, time points with high variability of count levels, occurring, e.g., during on- and off-switching of emitters, were removed. The resulting mask of single-molecule emission events was then applied to the raw count traces, where cycles of TCP exposures were binned into sections containing a user-defined number of photons (N)[49].

For every set of binned single-molecule photon counts, containing one photon number per TCP position, one set of fluorophore coordinates was estimated. Balzarotti *et al.* (2017) introduced position estimators based on least mean square (LMS) or maximum likelihood estimation (MLE). LMS estimation is computationally faster and more straightforward to implement, but does not include information from the central position in the TCP[50] and introduces bias for large TCP sizes. Hence, we used this estimator predominantly for setup characterization measurements and for bead samples providing a large number of photons. For super-resolution imaging of samples exhibiting single-molecule switching, we localized fluorophores via MLE (Figure 2.5B). When using a 2D TCP comprising four exposures with a doughnut beam, MLE cannot be solved analytically, and hence necessitates a numeric approach. Balzarotti *et al.* (2017) solved this via an iterative grid search. In our Python implementation, this proved to be relatively slow. It was more efficient[51] to calculate a mesh of relative beam intensities for all TCP exposures at reasonably fine spatial sampling (few Å) straight away, and designate estimated emitter coordinates as the position where the log-likelihood was highest. For adequate performance of MLE, it turned out to be crucial to model background explicitly by modifying the relative intensities before grid search, rather than subtracting background from the count traces. The software also provided the option to model the beam shape rather than assuming an ideal doughnut beam, but we could correct aberrations sufficiently well on the SLM that this did not notably improve data quality. Moreover, drifts could be corrected *post hoc* by fitting a polynomial function to the time-coded localizations for each axis. For some datasets, this made reconstructions appear visually crisper. However, it was often difficult to assess whether *post hoc* drift correction genuinely reflected the biological data or might be affected by artifacts. Therefore, I used this procedure very conservatively, and refrained from using it for the datasets discussed above.

Subsequently, localizations were visualized either as scatter plots (with options for color-coding based on position of the tip/tilt mirror or time), 2D-histograms (with option for shifting for better visualization) or as 2D Gaussian functions of user-defined width. The latter rendered single-molecule reconstructions most convincing, as judged by visual inspection. On the other hand, scatter plots were useful to evaluate density of localizations or mechanical stability, e.g., by tracking a bead as done in Figure 2.3D.

Finally, the software provided basic tools for downstream data analysis, currently focusing on non-switching bead samples. For example, mechanical stability could be analyzed based on Fourier transforms of counts or localizations, and models for attainable localization precision were tested by employing a range of photon numbers for binning.

[49] Due to the stochastic nature of photon emission, this value was rarely reached exactly. Instead, cycles were added up until the number was crossed. Using commonly employed acquisition settings, the target values were usually exceeded by less than 100 counts for single-molecule samples.

[50] This can be remedied by including an additional term, which, however, biases the estimator. In conjunction with *post hoc* unbiasing, this approach is useful for single-molecule tracking applications where fast position estimation is crucial, and few photons are detected per time step, since convergence to the Cramér-Rao bound requires fewer photons than MLE.

[51] This way, MINFLUX localization was performed within ca. 1 min on a standard laptop for the datasets shown in Figure 2.5C.

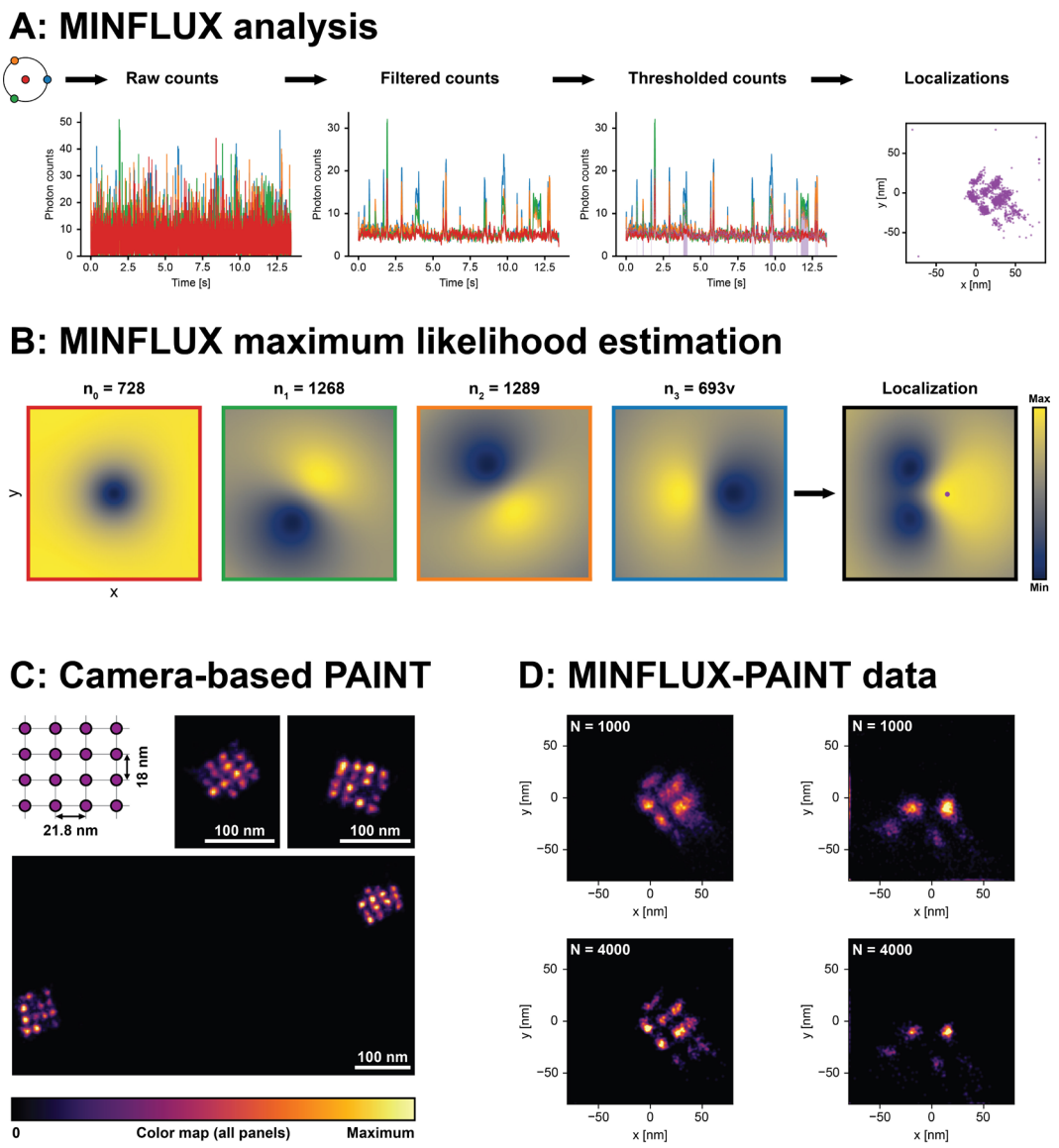

Figure 2.5: MINFLUX analysis workflow and proof-of-principle data. ***A:*** *Overview of the MINFLUX analysis workflow. Raw count traces (colors corresponding to TCP exposures shown on top left) were low-pass filtered to reduce noise, and thresholded to extract time points with single-fluorophore emission. Photons from emission events were then binned and used to localize fluorophores (data in the right panel correspond to the reconstruction shown in the lower left panel of D corresponding to ~4000 s MINFLUX acquisition time; other panels show first ~13 s of acquisition).* ***B:*** *Illustration of the MINFLUX localization process via maximum likelihood estimation. Panels represent a grid of position coordinates within the TCP. The first 4 panels show the natural logarithm of the relative optical intensities (modified to account for background) the grid positions are exposed to for the different TCP-positions (same color-coding of edges as count traces in A). Summing these values, weighed by the photon counts displayed above, yields the log-likelihood for an emitter being located at each grid position (right panel). Emitter coordinates are estimated as the position of maximum log-likelihood (purple dot).* ***C:*** *Camera-based PAINT data of DNA-origami grids featuring 4x4 binding sited spaced by 18 and 21.8 nm along orthogonal directions.* ***D:*** *MINFLUX-PAINT data of different origamis on the same coverslip as in B. Each column shows one origami with emission events binned to different photon numbers N. Coordinates are given with respect to the TCP center. For visualization, localizations were convolved with a Gaussian function with σ = 1 nm.*

3 High-Resolution Fluorescence Imaging at Cryogenic Temperatures

The implications of cooling samples to cryogenic temperatures for fluorescence microscopy, in particular super-resolution imaging, have been extensively discussed in the introduction. In brief, keeping sample temperature below 135 K allows for investigation of near-natively preserved vitrified samples, and is amenable to correlation with cryo-ET data. Reaching these low temperatures requires dedicated sample stages operated with liquid nitrogen or liquid helium as cryogen. So far, we have restricted ourselves to the former, cooling samples to > 77 K. We explored different cryo-stages, supported by straightforward reconfiguration of our microscope frontend (Figure B.2). Due to the small engineering overhead, we started cryo-imaging using a commercially available, open cryo-stage (Section 3.1). Since we found the mechanical stability to be insufficient for our needs (Section 3.1.1), we decided to adapt a closed vacuum cryostat for imaging of vitrified samples (Section 3.2). I thoroughly characterized cryostat performance, and further refinements are in progress. For all measurements described here, samples were attached to EM-grids comprising a holey carbon support film of size R2/2 (2 µm hole diameter, 2 µm space between holes), and a gold or copper mesh of various size.

3.1 Open cryo-stage

We performed initial cryo-microscopy experiments on a commercial open cryo-stage. Choosing a commercially available device was motivated by the small engineering overhead, enabling cryo-experiments at an early stage of the project. Two widely used options are the CMS196 by Linkam Scientific Instruments, and the cryo-stage distributed by Leica Microsystems as part of their cryo-CLEM setup. Due to the availability as stand-alone cryo-stage which could easily be incorporated into our homebuilt setup (compare Figure B.2A-B), we procured Linkam's CMS196. However, we also borrowed the Leica stage from a setup at ISTA's Electron Microscopy Facility to examine its mechanical stability (Section 3.1.1).

The cryo-stages notably differ in their internal makeup (Figure 3.1). In the Linkam cryo-stage, the sample is loaded directly inside the cryo-chamber of the cryo-stage to a magnetic holder[52], which is then moved to a platform thermally connected to the reservoir of liquid nitrogen. The platform is attached to motors for lateral sample positioning. On the platform, the sample is located in a cold nitrogen gas atmosphere, but grids are immersed within liquid nitrogen during loading[53]. During loading, sample access is provided by a hole in the lid. In the imaging position, the objective is inserted through the same hole. Liquid nitrogen lasting for roughly 4 h of operation is provided by an external dewar, which fills an internal dewar (every 10-20 min) transferring liquid nitrogen to the cryo-stage chamber (every 1-2 min). Refilling of the internal dewar and the cryo-chamber occurs automatically, triggered by increasing temperature. The stage also allows for transmission light microscopy using a built-in LED emitting at ~530 nm.

In the Leica cryo-stage, samples are loaded to a shuttle in a separate chamber. The shuttle is then transferred to the cryo-stage, where its receptable piece is cooled to ~78 K by cold nitrogen gas. Liquid nitrogen is actively pumped from an external dewar, and evaporates

[52] Linkam offers holders for unclipped EM-grids and auto-grids. I exclusively used auto-grids because the increased mechanical stability provided sufficient robustness for handling of grids without excessive bending.

[53] Many cryo-EM operators seek to avoid contact with liquid nitrogen due to the risk for ice contamination. However, contamination depends strongly on the properties of the cryo-chamber. Due to the chamber's small size in the Linkam stage, it stands to reason that elevating the samples above the liquid phase throughout the loading process might aggravate contamination rather than mitigating it.

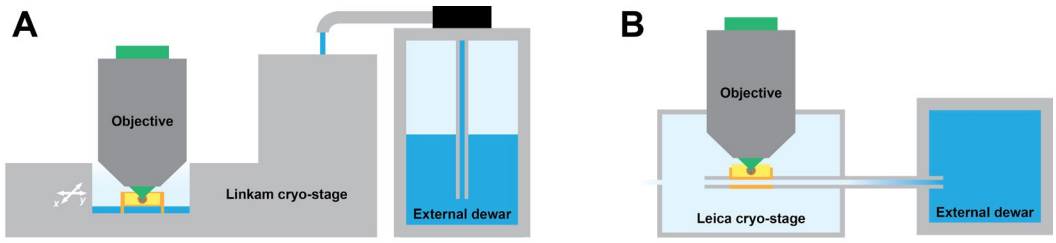

Figure 3.1: Simplified makeup of commercial cryo-stages tested. Liquid nitrogen is depicted as dark blue, cold nitrogen gas as light blue. The sample constitutes an EM-grid mounted on a yellow sample holder or shuttle. ***A:*** *In the Linkam cryo-stage, the sample is located in cold nitrogen gas atmosphere on a platform in thermal contact with a bath of liquid nitrogen in the cryo-chamber of the cryo-stage. Liquid nitrogen is provided by an internal stage dewar, which is filled automatically from an external dewar dropping liquid nitrogen through a designated opening from above.* ***B:*** *In the Leica cryo-stage, samples are loaded inside an external loading chamber (not shown) to a shuttle, which is transferred to the cryo-stage. Cooling is provided by a pipe, channeling cold nitrogen gas through a metal block in contact with the shuttle. The cryo-stage is connected to an external liquid nitrogen dewar through a hose. Nitrogen is actively pumped to the stage, where is arrives in gaseous state. A small opening allows nitrogen gas to escape to avoid buildup of pressure.*

before reaching the cryo-stage. Nitrogen gas exits the pipe within the cryo-stage, thus purging the environment of humidity and providing a cold atmosphere. In both cryo-stages, positive pressure from evaporating nitrogen prevents humidity from entering the sample environment. However, some contamination still aggregates, especially during long acquisition times typically associated with cryo-super-resolution microscopy.

3.1.1 Mechanical stability of commercial cryo-stages

Mechanical stability is essential for cryo-super-resolution microscopy due to high spatial resolution and extended acquisition times. This is particularly critical for cryo-MINFLUX, where *post hoc* drift correction is challenging. As discussed in Section 2.2, instability can arise from slow, continuous drifts, or fast, periodic vibrations, with distinct effects on super-resolution imaging approaches. Having verified that our setup is sufficiently stable to allow for sub-nm drift correction in 3D at RT (Vorlaufer et al., 2025), we thus set out to characterize mechanical stability of our cryo-stage.

We investigated the stability of our Linkam cryo-stage by tracking brightly fluorescent spots within cells[54] grown on holey carbon grids, using the setup's WF mode. The pattern of the holey carbon support film was used for active stabilization. Due to accumulation of ice contamination during measurements, active stabilization often failed after some time[55]. However, these incidents were clearly apparent in the raw data, such that the data presented here were not notably affected by ice contamination. The traces in Figure 3.2A revealed that for a large fraction of the measurement time, the sample stayed within roughly 10 nm of the average position. However, these periods were interrupted by regular excursions reaching deviations around 50 nm along x and y. These excursions were clearly correlated to refilling

[54] These samples were intended to be used for cryo-PALM experiments, imaging PAGFP attached to the F-actin binding protein utrophin (Section 3.1.2). However, all cells showed brightly fluorescent spots, presumably because cell health suffered during sample preparation. Potentially due to altered photophysics upon aggregation, no photoswitching was observed, and I tracked the fluorescent spots as markers for sample position.

[55] The measurements had been acquired before the published version of the stabilization scheme (Vorlaufer et al., 2025) was developed. Hence, axial stabilization and robustness may have not been optimal. However, the procedure for lateral stabilization was not modified, such that the conclusions presented here should not be notably affected.

of liquid nitrogen in the cryo-chamber of the stage[56]. I attempted to increase the feedback speed, but ultimately the sample moved too fast to eliminate these deviations. Refilling of the internal dewar resulted in additional pronounced drifts. These occurred on slower timescales, making them less disruptive to active drift correction, but still affected stability. Finally, occasional spikes of sample position uncorrelated to refilling of liquid nitrogen could reach amplitudes over 100 nm. Since they only appeared after cooling down the cryo-stage, they may be associated with boil-off of liquid nitrogen at or close to the sample platform. Of note, drifts along the optical axis very generally observed to be less severe than the lateral drifts shown in Figure 3.2. Overall, the attachment of the sample platform to the translation motors via two thin glass capillaries from the side did not appear to be very sturdy to perturbations caused by the cryogen. Without cooling, our Linkam cryo-stage reached nm-scale short-term stability.

We reasoned that it may be worthwhile to investigate mechanical stability of the Leica cryo-stage, mounted on our homebuilt setup, as well, since its construction differs notably from the Linkam cryo-stage in important aspects. Due to geometrical constraints, we could not attach the loading chamber to the setup while the stage was in place. Hence, before cooling, we loaded an empty EM-grid, mounted on the shuttle, to the cryo-stage. I tracked holes in the support film, while using a different set of holes for active stabilization. The results in Figure 3.2B, indicated reduced stability compared to the Linkam cryo-stage. Stability was reduced at short and long time-scales to levels that may severely hamper cryo-SMLM. Nevertheless, active stabilization eliminated long-term drifts, and short-term stability was not observably worse than without engaging it. Without cooling the stage, the stability was substantially improved, also when the hose was connected to a full liquid nitrogen dewar. We therefore attributed vibrations to the pump supplying the cryo-stage with liquid nitrogen, and explored various measures to mitigate them. Mechanically supporting the hose and switching from constant temperature to constant pump speed did not have a significant effect. Increasing the cryo-stage temperature slightly improved stability by reducing pump speed and associated vibrations, but only to $\sigma \approx 30\ \mathrm{nm}$ per axis for 133 K, which is unsatisfactory in terms of both mechanical stability and sample temperature. Finally, we tried supplying nitrogen from the gas or liquid outlets of a large nitrogen dewar (Taylor Wharton XL) instead of pumping. However, the gas outlet did not provide sufficient cooling power, and I did not manage to adjust the liquid outlet to an appropriate flow level, generating sufficient cooling but no liquid nitrogen accumulation inside the cryo-stage. Potentially, these issues could be solved by careful engineering, but we decided to focus our efforts on adapting a vacuum cryostat (Section 3.2).

Taken together, our measurements indicated that the commercial open cryo-stages we tested did not fulfill mechanical stability requirements for cryo-MINFLUX imaging. In camera-based cryo-SMLM, *post hoc* drift correction may mitigate the problem, but the limited mechanical stability might still be prohibitive for nm-scale resolution. The examined cryo-stages were designed mainly for diffraction-limited cryo-CLEM using WF, confocal or ISM, and there is only limited room for custom modifications. However, this does not mean that open cryo-stages are inherently unfit for high-resolution imaging. Other research groups are actively developing cryo-stages with enhanced stability.

[56] Accordingly, whenever I used active sample stabilization on this cryo-stage, I took care to engage it at time points allowing for sufficient time to acquire all reference stacks without being affected by refilling of liquid nitrogen.

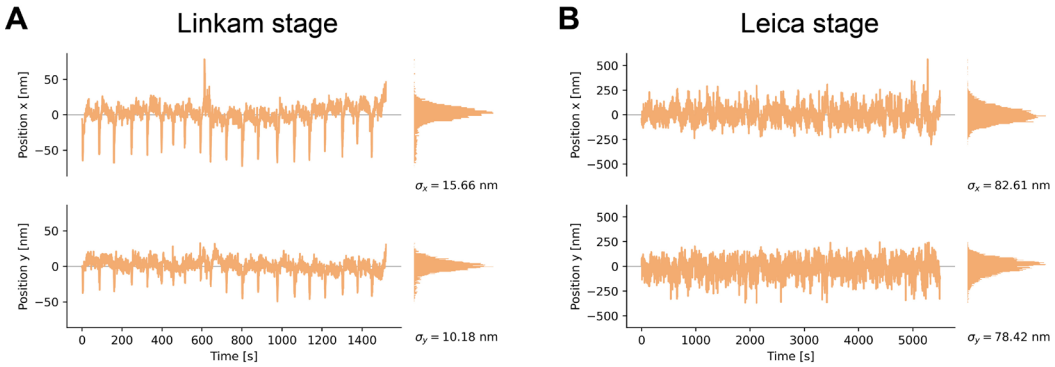

Figure 3.2: Mechanical stability of commercial open cryo-stages. In both panels, time-series traces are show on the left, and position histograms on the right-hand side for the respective axes. Standard deviation of data points within a time series is denoted as σ. ***A:*** *Traces of brightly fluorescent spots within cells imaged on the Linkam cryo-stage. Active sample stabilization compensated drifts using the pattern of the holey carbon film as reference structure. Regular excursions are correlated with refilling of liquid nitrogen. These movements were too fast to be effectively corrected by active stabilization.* ***B:*** *Position of the center of a hole in the support film of an empty EM-grid tracked on the Leica cryo-stage. A different set of holes was used for active stabilization.*

3.1.2 Testing fluorophores

We used the Linkam cryo-stage for all measurements discussed in this section. While mechanical stability remained limited as discussed in the previous section, this did not impact the high-level investigation of cryo-photophysics we performed, except for limiting measurement times before the focus was lost. Active sample stabilization is compatible with the cryo-stage, but due to accumulation of ice contamination on samples during acquisitions, it failed quite often within 1-2 h. Preliminary CLEM experiments on fluorescent beads suggested that heating the objective might reduce ice contamination. Even though this observation was based on a single sample, I adapted objective heating for later measurements, applying 1.8 W to a resistive foil heater adhering to the objective. Potentially, this also improved optical performance by preventing condensation of humidity on the objective front lens. Sample preparation protocols are described in Appendix C.

Before starting cryo-super-resolution experiments, I imaged B16 cells stained with AF488-phalloidin targeting F-actin, using WF and confocal, to ensure adequate performance of the imaging system and cryo-stage. Figure 3.3A shows example datasets, looking comparable to imaging the same sample on the Leica CLEM setup at ISTA's Electron Microscopy Facility. As expected, the maximum intensity projection of a confocal z-stack in Figure 3.3A.ii contained more pronounced filamentous structures than a single WF projection displayed in Figure 3.3A.i, or a maximum intensity projection of a corresponding WF-stack (not shown). Upon closer inspection, artifacts related to movement of the cryo-stage during acquisition of confocal scans become apparent. Without correction, these may impact downstream correlation to cryo-EM.

The first fluorophore we tested for cryo-SMLM was mEmerald, fused to ER3, transiently expressed in rat fibroblast cells (for protocol see Appendix C.5). Hoffman *et al.* (2020) showed high-quality cryo-SMLM data on this fluorescent protein at liquid nitrogen and liquid helium temperatures. However, both their sample carriers (sapphire disks) and cryo-stage (vacuum cryostat) differed from our setup. In our hands, I only observed gradually decreasing intensity within 4 h of high-intensity illumination with 488 nm, no single-molecule switching or even flickering. Increasing the optical intensity above ~40 W/cm^2 (rough estimate based on power calibration at later time point) induced melting of the ice, clearly observed in transmission

light microscopy, even when imaging in the vicinity of grid bars, which conduct heat more effectively than the carbon support film. Hence, it stands to reason that the applied intensity has led to devitrification in other datasets as well, but this was not investigated further. Pulsing the illumination (50 % duty cycle at 100 Hz) while leaving the time-averaged intensity constant did not increase the melting threshold. Restricting the illumination to roughly 10 µm diameter allowed for increased intensity, resulting in some observable intensity fluctuations. There was still a substantial background of active emitters which was removed by subtracting median pixel intensity values across the entire acquisition for every pixel. The reconstruction (Figure 3.3D) showed some features in line with typical structures in the ER, but data quality was sub-optimal and the sample was likely devitrified. I tried switching fluorescence off directly before freezing, similar to a previous study on rsEGFP2 (Tuijtel et al., 2019), but the pertinent 488 nm laser on our microscope setup did not provide enough optical power[57]. Since heating is mediated predominantly by the support film, restricting illumination entirely to grid holes might allow for increased local optical intensities and improved single-molecule switching. However, when I tested this by straightforward focusing of excitation light at the sample plane, inhomogeneous illumination profiles and background from adjacent regions impeded this strategy. Larger holes in the support film might alter cell behavior depending on the structure of interest and cell type. Milling the film away after freezing could be an attractive strategy, but comes with additional overhead. Exchanging the carbon film for a different material exhibiting increased thermal conductivity (Dahlberg et al., 2022; Last et al., 2023) may be more straightforward, but typically limits downstream cryo-ET acquisition to holes. In case single-molecule switching of mEmerald is unfeasible with the setup configuration used here, the fluorophore might lend itself to fluctuation-based imaging approaches, such as SOFI and SRRF, albeit at presumably lower resolution.

We performed cryo-SMLM using PAGFP, which was previously reported to be photoswitchable at liquid nitrogen temperature (Chang et al., 2014; Tuijtel et al., 2019), attached to the F-actin binding protein utrophin. We transfected rat fibroblast cells (for protocol see Appendix C.5) with a PAGFP-utrophin plasmid (Burkel et al., 2007). A control experiment at RT, performed on chemically fixed cells grown on coverslips, revealed a high level of activated fluorophores without the application of activation light. This might be attributable to exposure to ambient light during sample preparation. Still, PALM experiments were feasible and the reconstructed actin cytoskeleton appeared as expected. In contrast, after plunge-freezing transfected cells, no notable pre-activation was observed. However, all cells contained brightly fluorescent spots, presumably indicating that they were not in a healthy state. These spots could not be bleached using 488 nm light at intensities below the devitrification threshold. During cryo-PALM acquisitions, they remained substantially brighter than single-molecule emission events observed throughout the cells. Most cells showed photoswitching in response to 488 nm light, and 405 nm pulses promoted photoactivation. Density of activated fluorophores differed between cells, potentially due to variability of transfection. 488 nm illumination caused both on- and off-switching, albeit at substantially reduced efficiency compared to 405 nm, a qualitatively similar behavior as observed at RT. Figure 3.3B shows an example cryo-PALM dataset. Inhomogeneous background was removed via median subtraction, analogous to the mEmerald dataset described above. The distribution of localizations within the cell is somewhat in line with expectations. However, the localization

[57] I wanted to image samples during illumination which necessitated an objective with a long working distance and accordingly low magnification, thus spreading light across most of the grid. Incoherent light sources with high optical power might have been an appealing alternative, but would require some level of optimization.

density is far too low to make informed statements about quality of the staining, or reconstruct any filamentous arrangements. As proxy for the overall distribution of fluorescent signal, I overlaid localizations with the average intensity values across the acquisition. Directly imaging non-blinking fluorophores would presumably provide a more faithful representation of their distribution. We performed experiments on two biological replicates with similar results.

Cellular actin may be a challenging test target due to high background and limited control over fluorophore density. Hence, we reasoned that PAGFP-utrophin bound to *in vitro* polymerized actin filaments might provide a more amenable platform for testing cryo-photophysics at the single-molecule level (for protocol see Appendix C.6). Most importantly, it should allow for straightforward tuning of fluorophore density by adjusting the concentration of actin filaments applied to EM-grids. Directly applying polymerized actin to grids resulted in filamentous arrangements appreciable in fluorescence imaging, but their density was clearly too high for compatibility for cryo-EM without thinning. Hence, we adjusted filament concentration by spinning them down with a centrifuge and varying the amount of buffer applied to the resulting pellet. Moreover, we confirmed that PAGFP-utrophin was bound to actin filaments in the pellet via gel electrophoresis[58]. AFP647-phalloidin, applied to polymerized filaments after PAGFP-utrophin incubation and centrifugation, served as brightly fluorescent control. However, while there was some correlation between the actin concentration in buffer applied to EM-grids and measured fluorescence (in terms of both WF-signal in the far-red imaging channel and localization density in the green channel), this relationship was highly non-linear, and greatly differed between grids or even regions on the same grid. We failed to find a concentration where fluorescence intensity was repeatably adequate, presumably in part due to variability associated with the plunge-freezing process.

One of the more successful attempts at setting up a cryo-SMLM measurement on this sample platform is shown in Figure 3.3C. Here, single-molecule emission events were clearly apparent above the background fluorescence on the support film which was still notable but clearly weaker than inside cells. It seemed that emission events were somewhat dimmer on the support film[59]. Similar observations have been reported for rsEGFP2 and rsFastLime (Tuijtel et al., 2019). The WF-fluorescence signal in the far-red channel (Figure 3.3C.ii) revealed that some grid holes were filled, while others remained empty. This made it hard to choose appropriate activation parameters. As can be seen in the raw data, by the end of the acquisition, a large number of active emitters had accumulated within filled holes, hindering SMLM in these regions. At different locations, only very sparse emission events were detected, even though the far-red signal indicated the presence of F-actin. Altogether, we did not reconstruct actin filaments in cryo-SMLM on *in vitro* samples.

We performed rough-scale CLEM to investigate the relationship between filament density visualized by cryo-EM and fluorescent signal (Figure 3.3C.iii-iv). Despite the high level of ice contamination, a dense arrangement of filaments was clearly apparent. Regions with

[58] Gels contained two stripes for PAGFP-utrophin, instead of expected single stripes. This might be an artifact of the purification process. We did not investigate it further.

[59] Some of the fluorophores might be located behind the support film, which would absorb a fraction of excitation and emission light. However, this should result in two populations of bright and dim emission events which was not apparent. The support film might also dim fluorescence via quenching or other interactions. Further investigations would be necessary to draw conclusions about the nature of this effect.

comparatively low far-red fluorescence, where no single-molecule localizations were retrieved, actually contained a substantial number of filaments. On regions exhibiting high signal and some clusters of localizations, strong bundling of filaments[60] was observed in cryo-EM datasets.

Preliminary control experiments, applying *in vitro* polymerized actin filaments to coverslips followed by fluorescence imaging at RT, showed more pronounced structures in WF, and, as expected, substantially higher levels of photoswitching. However, due to the limited resolution, it is not straightforward to assess whether a structure appearing as filament in WF or SMLM measurements is a single filament or a bundled arrangement.

Taken together, these data indicated a very low photoactivation efficiency of PAGFP in our hands at liquid nitrogen temperature. Arguably, reconstructing actin filaments was a more demanding task than some of the published super-resolution cryo-CLEM test targets. Therefore, it was challenging to reliably assess whether our data were in line with expectations for this fluorophore or there are flaws in our workflow. Thus, these experiments also illustrated the limitations of *in vitro* polymerized actin filaments as sample platform for cryo-SMLM. On plunge-frozen EM-grids, they did not provide the level of reproducibility or control over filament density we had hoped for. Affinity grids might enable a more controlled distribution of adherent actin filaments. Potentially, an adapted version of photo-micropatterning (Toro-Nahuelpan et al., 2020) could generate bespoke structures allowing for a more informed assessment of cryo-SMLM data quality. Besides the sample, the most fundamental issue was the relatively short acquisition time, limited by accumulation of ice contamination. Presumably, this prevented the activation of most of the fluorophores in the sample. Hence, we exchanged our open cryo-stage for a vacuum cryostat (Section 3.2), rather than modifying sample preparation.

Finally, we tested the photoactivatable dye PaX560 (Lincoln et al., 2022), generously provided by Richard Lincoln from the Hell lab at the Max Planck Institute for Medical Research in Heidelberg. Generally, synthetic dyes exhibit superior photophysical properties over fluorescent proteins. Compared to spontaneous blinking, photoactivatable dyes may provide additional optical control by tuning activation intensity, pulse length and repetition rate. We co-stained B16 cells with PaX560-phalloidin for cryo-PALM imaging and AFP647-phalloidin as diffraction-limited control, adapting the protocol previously used for RT measurements (Appendix C.3) for EM-grids. Again, staining was performed under red light, and samples were shielded as much as possible from ambient light during staining and imaging. In WF, cells looked substantially healthier than previous experiments, transiently expressing fluorophores (compare Figure 3.3E and B). Single-molecule switching events were comparable to PAGFP-utrophin samples, potentially somewhat brighter and more frequent. Again, the localization density was far away from a comprehensive visualization of F-actin distribution. Clusters outside the cells might be associated with off-target binding of fluorophores. However, as for all experiments described in this section, I chose a rather low threshold for detecting emission events in order to ensure localization of as many emitters as possible. It is possible that this might have resulted in false positive detections.

[60] Due to the low SNR and ice contamination, filaments appear rather subtle. However, upon closer inspection – to the trained eye already at first sight – they emerge more clearly.

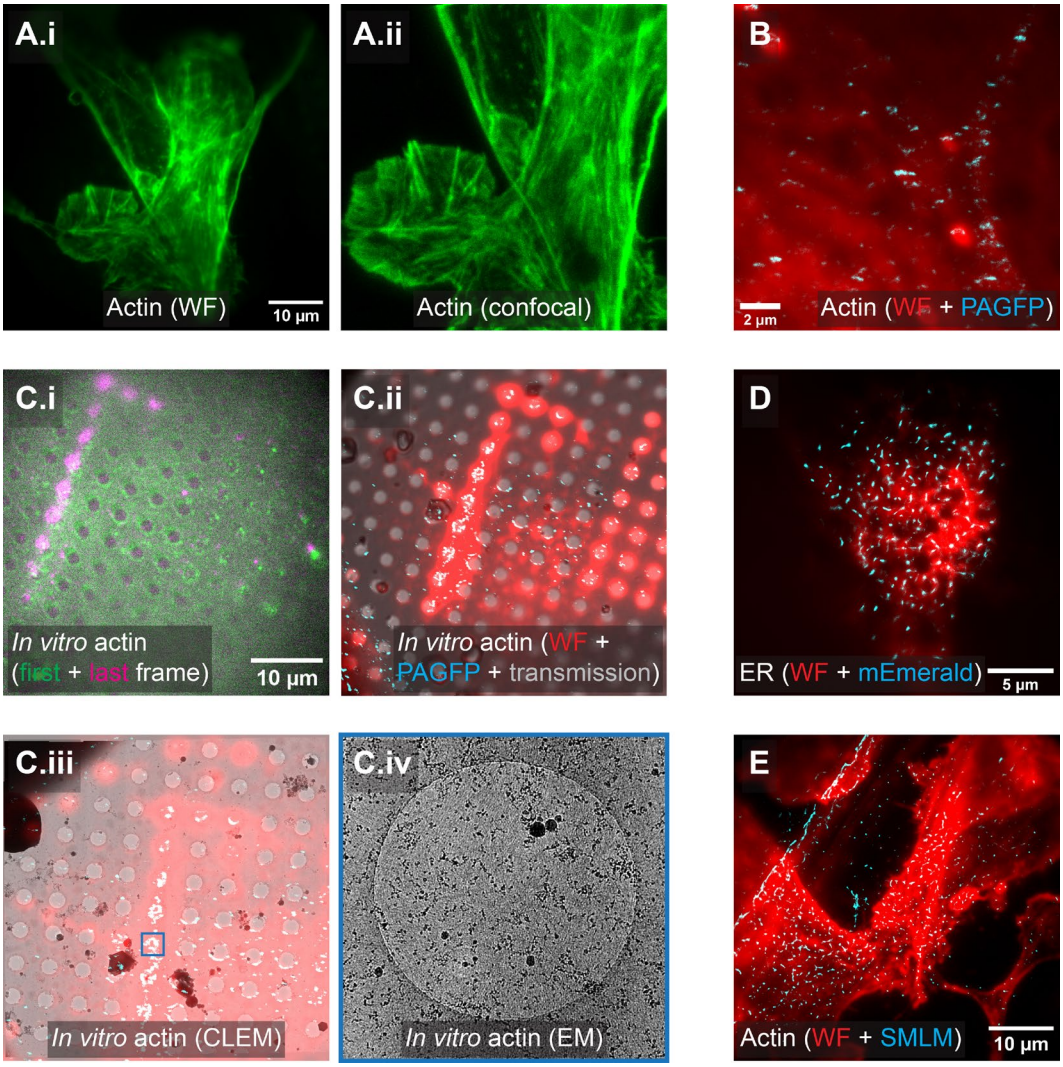

Figure 3.3: Example datasets using the Linkam cryo-stage, all acquired at liquid nitrogen temperature. ***A:*** *WF image (A.i) and maximum-intensity projection of a confocal z-stack (A.ii) of the same B16 cell, stained with AF488-phalloidin. The confocal scan was flipped horizontally to align the orientation with the WF image.* ***B:*** *Rat fibroblast cell transiently expressing PAGFP-utrophin. Overlay of PAGFP-localizations (cyan) and average pixel intensity values throughout the acquisition (red).* ***C:*** In vitro *polymerized actin, binding PAGFP-utrophin (green imaging channel) and AFP647-phalloidin (far-red channel). C.i: Overlay of first (green) and last frame (magenta) of a cryo-PALM acquisition. Shifts between bright spots appearing in both frames can be attributed to lateral drifts. Due to focus drift during the acquisition, background from the support film is defocused in the last frame and hence appears lower. Pronounced photoactivation inside grid holes in the top left corner is correlated to fluorescence in far-red channel (compare panel C.ii). C.ii: Overlay of WF-image acquired in the far-red channel visualizing AFP647-phalloidin (red), cryo-PALM reconstruction of PAGFP-utrophin (cyan), and transmission light microscopy (gray) of the same ROI as displayed in C.i. C.iii: Cryo-CLEM overlay of approximately the same ROI as in the previous panels, indicating that areas of high phalloidin-signal correspond to grid holes filled with actin filaments. Cryo-EM data visualized in grayscale, the other channels with same colormaps as C.ii. To enhance contrast, histogram equalization was applied to fluorescence signal. C.iv: Zoom on a grid hole, revealing actin filaments upon closer inspection. Particles giving strong contrast are ice contamination.* ***D:*** *Rat fibroblast cell transiently expressing mEmerald-ER3. High-intensity light illumination induced flickering of fluorescence signal, but sample heating hindered application of adequate optical power for single-molecule switching. SMLM was attempted after background subtraction, as described in the main text. Attempted mEmerald cryo-SMLM reconstruction (cyan), overlaid with average pixel intensity values throughout the acquisition (red). Illumination was constrained to reduce light-induced heating of the sample.* ***E:*** *B16 cells co-stained with AFP647-phalloidin (far-red imaging channel) and PaX560-phalloidin (orange channel). WF-image of the far-red channel is shown in red, cryo-SMLM reconstruction acquired in the orange channel in cyan.*

Surprisingly, many switching events were not induced by activation pulses, but occurred during illumination with 561 nm light. In a control experiment performed at RT (described in Section 2.3), we found that these blinking events presumably result from photoblueing of AFP647. Therefore, this measurement may point to photoblueing, reported for several far-red organic dyes (Helmerich et al., 2021), as potential cryo-photoswitching mechanism. The dataset shown in Figure 3.3E corresponds to our second attempt at acquiring cryo-SMLM data on this sample type. It was terminated due to failure of the cryo-stage. Since we decided to focus our efforts on integrating a vacuum cryostat instead of sending the Linkam cryo-stage for repair, we have not performed follow-up measurements optimizing acquisition parameters.

3.2 Vacuum cryostat

As mentioned in the introduction, commercially available vacuum cryostats require some modifications to be compatible with vitrified samples. Most notably, they are designed for loading samples at room temperature, before evacuation and cooldown. This workflow is clearly incompatible with vitrified biological material. A system including pertinent modifications has been published (Hoffman et al., 2020), and the authors generously shared their technical models for us to use[61]. We used their designs as basis for our implementation, and modified parts as we saw fit for our system. For example, we borrowed a loading chamber and a transfer rod belonging to an Aquilos I cryo-FIB-SEM system, both decommissioned after an upgrading the system to Aquilos II, from ISTA's Electron Microscopy Facility. This design choice affected modifications to the sample holder, as described in Section 3.2.1. Characterization of setup parameters are discussed in Section 3.2.2, and preliminary cryo-fluorescence and cryo-super-resolution microscopy data in Section 3.2.3.

3.2.1 Hardware integration

Our cryostat was cooled by a cryogen transfer line, supplying liquid nitrogen[62] from an external dewar (Figure 3.4A). At the heat exchanger, the cryogen evaporated, and subsequently left through an exhaust pipe. Hence, it did not come in direct contact with the cryostat interior, which was evacuated by a turbomolecular pump backed by a pre-vacuum pump (components are listed in Section B.1.6). Vacuum effectively eliminated convective heat transfer, thus allowing placement of samples in close proximity to the viewing window (fused silica, 25.4 mm diameter, 0.5 mm thickness).

The viewing window required an objective with a suitable correction collar. We used a 63x/0.75 NA objective allowing for correction of 0-1.5 mm glass thickness. Positioning the somewhat bulky cryostat, including the attached custom loading system (described below), necessitated adaptations to the microscope frontend (Figure B.2C). The cryostat was mounted on a high-load vertical stage. For horizontal positioning of the objective with respect to the sample, a translation stage moved a platform with the objective as wells as a mirror, which rotated the optical axis by 90°. The objective itself was screwed to a cage-mounted

[61] An alternative modification integrating the same cryostat model was recently published (Mazal et al., 2025b). It seems quite sophisticated, and entails increased engineering overhead. Some aspects may inspire future improvements to our workflow.

[62] Exchanging liquid nitrogen for liquid helium to reach lower sample temperature should be quite straightforward using the system.

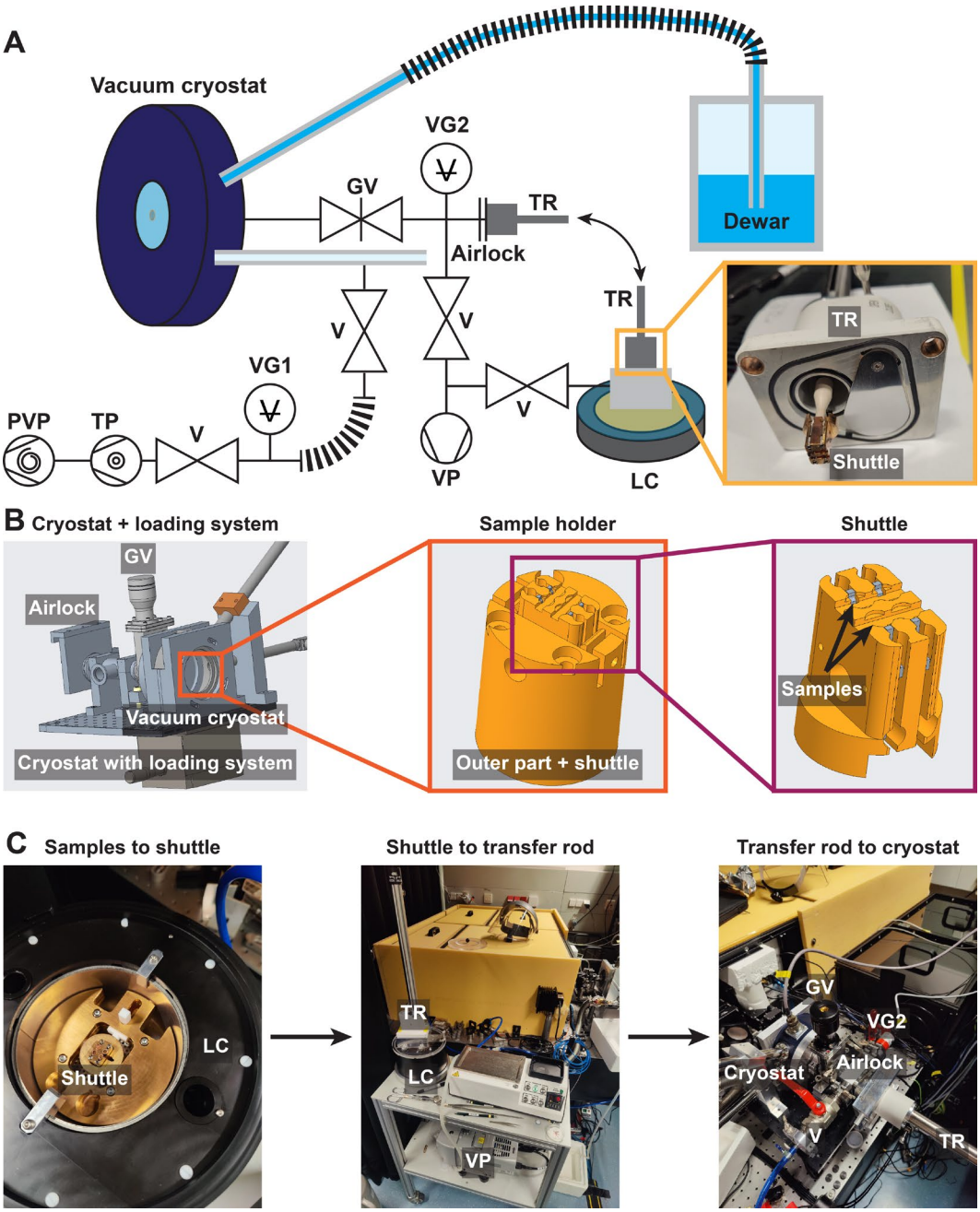

Figure 3.4: Integration of the vacuum cryostat in our homebuilt microscope setup. ***A:*** *Layout of the cooling and vacuum systems connected to the cryostat. The cryostat was connected to a liquid nitrogen dewar through a flexible, vacuum-isolated transfer line. A turbomolecular pump (TP), backed by a pre-vacuum pump (PVP), evacuated the cryostat, connected to the jacket of the nitrogen exhaust line through a corrugated vacuum hose. A separate vacuum pump (VP) evacuated either the transfer rod (TR) connected the lid of the loading chamber (LC) or the airlock, depending on the position of the respective valves (V). A gate valve (GV) connected the airlock to the cryostat for sample loading. Pressure was read out via vacuum gauges connected to the cryostat (VG1) and the airlock (VG2). Vacuum components were connected via KF-flanges.* ***B:*** *Modifications to the cold finger of the cryostat, replacing the installed metal post with a sample holder comprising an outer part and a shuttle, where up to 4 samples could be mounted. The back plate of the cryostat was exchanged for a modified version containing a hole for loading samples through the backside, using the airlock to ensure continuous vacuum while (un-)loading. On the shuttle, spring-loaded clamps (grey) held samples in place. Furthermore, the front plate of the cryostat was omitted in the left panel.* ***C:*** *Depiction of the sample loading workflow. The workflow is detailed in the main text. In short, in liquid nitrogen atmosphere, samples (clipped EM-grids) were loaded to the shuttle, which was picked up by the transfer rod and transferred to the cryostat under vacuum.*

translation stage for focusing. This arrangement comprising the objective lens and mirror sat on a 3D piezo stage[63] used for fine positioning and active sample stabilization.

A temperature controller, connected to a feedback system comprising a heater and a temperature sensor attached to the cold finger inside the cryostat, ensured temperature stability, specified to ±50 mK. The appendix of this thesis contains detailed descriptions of cryostat operation procedures (Section B.3).

A key modification to the cryostat was the loading mechanism, which required modifications to the sample holder[64] (Figure 3.4B). A custom back plate of the cryostat included an opening, through which cold, vitrified samples were loaded under vacuum via an airlock. Samples were mounted on a movable component, which we call shuttle. The shuttle was held in place at the imaging position by the outer part of the sample holder through magnetic attraction and mechanical clamping. A firm mechanical connection is instrumental for effective cooling because of the absence of convective heat transfer in vacuum. Pertinent components were manufactured from oxygen-free copper and gold-plaited. Currently, our sample holder does not include a temperature sensor. Therefore, we read out temperature from the built-in sensor at the cold finger which is a rather indirect proxy for sample temperature.

Inside the loading chamber, samples (up to 4 EM-grids) were loaded in liquid nitrogen atmosphere to the shuttle, where they were fixed by spring-loaded clamps (Figure 3.4B-C). Subsequently, the shuttle was rotated by 180° and picked up by the transfer rod from above. The transfer rod was attached to a dedicated lid, fitted to the loading chamber. Besides a vacuum port, the lid included a sliding valve, which was closed immediately after loading the shuttle to evacuate the chamber of the transfer rod. After closing the vacuum-tight lid of the transfer rod, it was transferred to the airlock, which was evacuated, followed by opening of the transfer rod lid and the gate valve. Finally, the shuttle was loaded to the imaging position inside the cryostat, and the gate valve was closed before starting cryo-microscopy acquisitions. After experiments, samples were unloaded by performing these steps in reverse order. Respective pump controllers operating the vacuum pumps attached to the cryostat and the pump for the airlock or transfer rod, were connected to RT nitrogen gas supply for venting spaces without introducing humidity.

3.2.2 Technical characterization

We characterized key performance parameters of our cryostat implementation. Besides temperature stability, we focused on mechanical stability and ice contamination. While the cryostat should be capable of nanoscale short-term stability, this hinges on the stability of our custom sample holder. Since ice contamination is closely related to vacuum quality, Section 3.2.2.3 treats both topics. Further improvements to the system are being implemented.

[63] The piezo stage was oriented horizontally with the movable part pointing upwards. As a result, the optical axis corresponded to the axis 2 of the piezo stage, as opposed to axis 3 for other frontend configurations. This required modifications to the axis assignment in the hardware control software for active sample stabilization. For all data presented here, the convention that z denotes the optical axis was maintained. Of note, the arrangement of the piezo stage also results in different ranges along the lateral axes, 30 µm along x and 10 µm along y.

[64] Modifications included removal of radiation shields from the back and front side of the cold finger due to geometrical constraints. We assumed that this should not affect cooling performance notably when operated with liquid nitrogen. However, we later installed a custom front radiation shield as cold trap (Section 3.2.2.3).

3.2.2.1 Temperature stability

As shown in Figure 3.5A, after starting supply of liquid nitrogen to the cryostat, temperature decreased slowly for tens of minutes before dropping rapidly[65]. After the temperature dropped below 78 K, nitrogen flow had to be greatly reduced to avoid excessive amounts of cryogen reaching the heat exchanger, leading to liquid nitrogen droplets exiting the exhaust port. Finding the right combination of pressure in the nitrogen dewar (≤ 5 psi, as specified by the manufacturer) and position of the transfer line's flow regulation valve proved to be tedious and highly variable between experiments. Adjusting the opening just enough to avoid heating of the sample holder generated mostly stable flow, resulting in long periods of high temperature stability (< 50 mK peak to peak). However, occasional spikes, correlated with bursts of nitrogen exiting the exhaust port, disrupted effective temperature control (Figure 3.5B). This behavior was difficult to troubleshoot since desired stability was often maintained for many hours before being disrupted without obvious cause. Moreover, performance of temperature control was not always reproducible, sometimes even changing within experiments. For example, in the measurement shown in Figure 3.5B, feedback[66] oscillated until the timepoint of 24280 s, when, after a spike, it suddenly became stable – again, without any intervention. Pressure in the dewar changed throughout some experiments, but typically not by a lot.

We recently realized that the leg of the transfer line entering the liquid nitrogen dewar was visibly bent. This might limit the stability of nitrogen flow, and we will attempt to straighten it. Another potential source of instability might be ice contamination in the dewar, transfer line or heat exchanger.

After having finished a cryo-imaging session, the interior cryostat components were warmed up by changing the setpoint of the temperature controller to a value slightly above room temperature[67] (Figure 3.5C). Relying solely on passive heating after switching off the liquid nitrogen supply is possible but was never attempted since it would have considerably increased warmup times.

[65] The precise temperature progression depended on nitrogen flow and components within the cryostat. For example, adding an additional cold trap, as described in Section 3.2.2.3, substantially increased cooldown times. However, the qualitative shape of the curve is reproducible.

[66] Surprisingly, changing the proportional, integral and differential feedback parameters within a wide range did not notably affect the temperature stabilization. I confirmed that the controller registered the entries by switching off feedback completely which led to deviations from the setpoint, as expected.

[67] I found 305 K to be a suitable value. Of note, it took over 1 h until all components genuinely reached room temperature, even though the setpoint was reached much sooner. Breaking vacuum earlier is not recommended since it might lead to accumulation of contamination inside the cryostat which might adversely affect vacuum levels in future experiments.

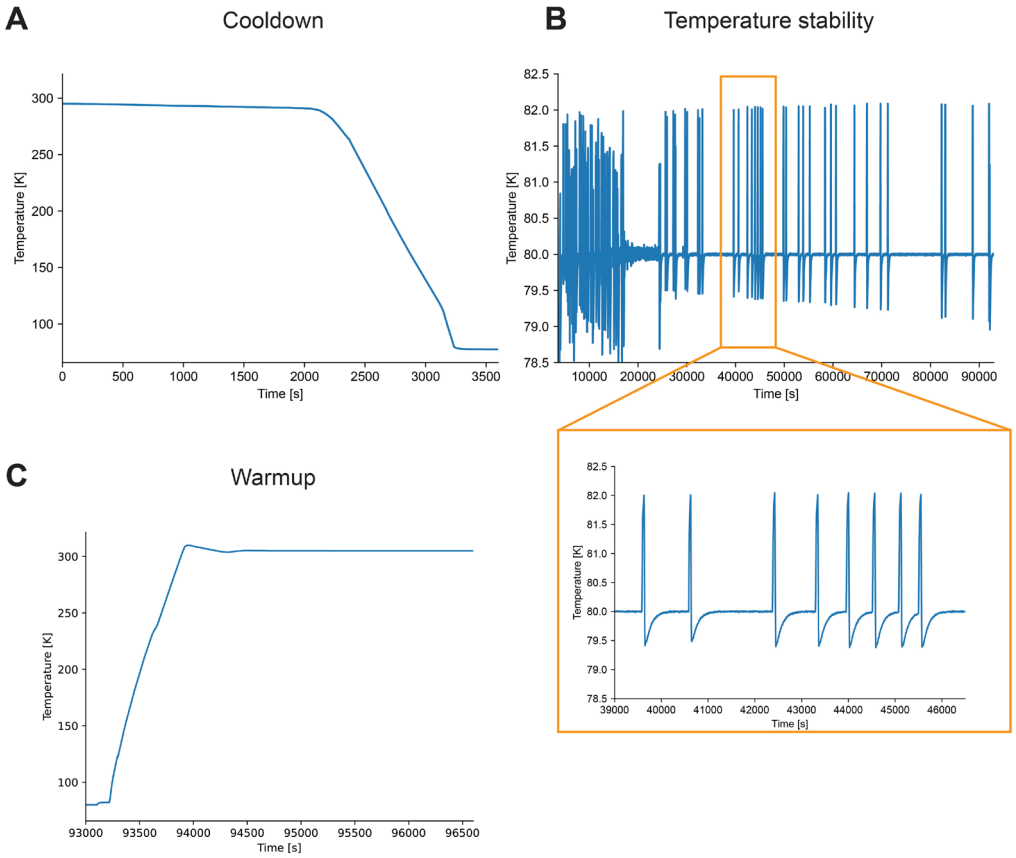

Figure 3.5: Temperature curves of a typical cryostat session, logged at ~1 Hz. ***A:*** *Temperature progression after starting the supply of liquid nitrogen from the dewar at ~0 s.* ***B:*** *Temperature traces while the cryostat was cooled down. The zoomed region below shows the highly repetitive shape of occasional spikes.* ***C:*** *After finishing all experiments, the cryostat is warmed up by changing the setpoint to 305 K, actively heating the cryostat interior.*

3.2.2.2 Mechanical stability

As mentioned in the introduction, high-stability vacuum cryostats typically exhibit lower vibrations than the commercial open cryo-stages tested in Section 3.1.1. The vibration amplitude of our cryostat model is specified at ±10 nm. However, substantially higher cryo-SMLM resolution has been reported using this model (Hoffman et al., 2020; Mazal et al., 2025b; Weisenburger et al., 2017), potentially because vibrations occurred at higher frequencies[68] and might have been averaged within the exposure time of single SMLM frames.

First stability measurements of our cryostat integration were performed by tracking an empty holey carbon grid, imaged using the WF-path of the stabilization module, without enabling feedback. After loading the shuttle, lateral drifts were very strong (Figure 3.6A), reaching up to ~10 nm/s. I did not directly measure drifts along the optical axis, but by eye it seemed that defocus was acceptable, indicating that axial drifts were negligible compared to lateral drifts. These very strong, continuous drifts typically subsided after roughly 3-4 h. Then, the sample still moved, but excursions slowed down and remained within a few µm (Figure 3.6B). Importantly, the short-term stability, indicating vibrations, which may not be rectifiable via active stabilization, was below ±10 nm, as specified. Occasional jumps of the sample

[68] A "typical vibration profile" displayed in the datasheet of the cryostat shows a notable fraction of the frequency spectrum above 20 Hz.

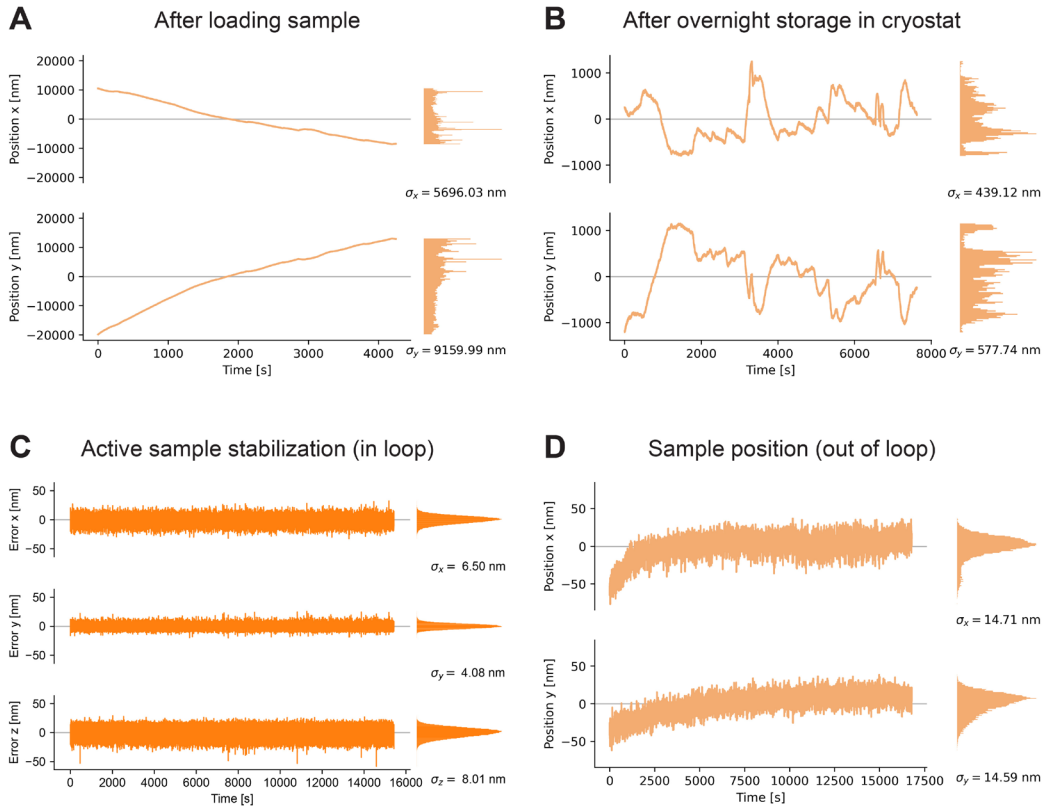

Figure 3.6: Mechanical stability of sample holder. ***A:*** *Tracking the position of an empty grid directly after loading to the cryostat. Active sample stabilization was not enabled. Loading was performed following the same workflow as for vitreous samples, pre-cooling the shuttle in the loading chamber (Section 3.2.1).* ***B:*** *Same grid as in A, tracked after leaving it inside the cryostat overnight.* ***C:*** *In loop errors of active stabilization, using the pattern of a holey carbon film as reference structure.* ***D:*** *Out-of-loop stability measurement tracking a bright spot, not showing photoswitching, in a B16 cell stained with AFP647-phalloidin, corresponding to the in loop data shown in C.*

position by few hundreds of nm were observed. They coincided with the temperature jumps discussed previously[69], identifying them as obstruction to nanoscale cryo-SMLM. I also tracked the position of the outer part of the sample holder, holding the shuttle in the cryostat (Figure 3.4B, middle panel) using an objective with long working distance, and qualitatively found comparable mechanical stability to directly tracking samples, confirming that the connection between the shuttle and the outer part was firm.

Directly after loading samples, the cryostat was incompatible with active stabilization. Excessive drifts during the acquisition of reference stacks may adversely affect displacement estimation, and samples would travel the entire range of our piezo stage (30 µm along x and z, 10 µm along y[70]) within < 20 min. After allowing for sufficient time for initial drifts to subside, active stabilization reached in loop performance better than 10 nm in 3D (measured as standard deviation of calibrated error signals; Figure 3.6C). However, the out-of-loop stability (measured by tracking brightly fluorescent sample features while active stabilization

[69] Interestingly, this behavior could not be reproduced by increasing the setpoint of the temperature controller by 2K. Hence, it might be connected to liquid nitrogen inducing vibrations in the heat exchanger, rather than thermal expansion of the sample holder. However, the effect of the heater might have been more subtle. Comprehensive investigation of the relationship between temperature and mechanical stability would require further measurements.

[70] As can be seen in Figure B.2C, axis names were modified from previous frontend configurations, such that z denotes the optical axis of the microscope, as customary.

was enabled; Figure 3.6D) was somewhat deteriorated. In particular, during the initial 1-2 h of stabilization measurements, drifts occurred that were not reflected in the error signals. This was observed on different samples, always moving in the same direction. Hence, it is likely connected to cross-talks observed from z to x and y. However, optical aberrations or drifts during the acquisition of reference stacks may additionally affect performance. I observed that calibration factors differed between samples and sometimes deviated substantially from 1, a behavior not observed previously for our stabilization scheme (Vorlaufer et al., 2025). Active stabilization was integrated into the cryostat frontend only recently. Extensive characterization, including stabilization measurements at RT, is still outstanding and may hint at applicable measures for improving performance. Nevertheless, when considering only timepoints after the initial settling period, I could routinely stabilize samples to below 10 nm, which already constitutes improved performance over the open cryo-stages we tested.

3.2.2.3 Ice contamination and vacuum leakage

Ice contamination is a major concern for cryo-EM since it can obstruct ROIs or limit image quality. Every sample handling step poses a potential risk for the accumulation of crystalline ice on samples, typically via condensation of humidity from ambient air or small flakes of ice swimming in liquid nitrogen. In principle, vacuum cryostats may reduce contamination compared to open cryo-stages by removing air, containing a few permille to percent of water vapor, from the sample environment. However, to my knowledge, no studies have rigorously investigated ice condensation on vitreous biological samples imaged in a cryo-CLEM workflow involving a vacuum cryostat.

After discouraging preliminary results, we set out to evaluate the effect of different steps in the workflow on ice contamination. Figure 3.7 contains a summary of our results. We used buffer (1xPBS, without any additives), applied to holey carbon grids, as test samples. Many of the imaged regions contained mostly open grid holes, indicating that the buffer had been blotted away there. Hence, visualized signal presumably stemmed from the support film and the accumulated ice contamination. Within the loading chamber, contamination remained at acceptable levels (Figure 3.7A). However, already in the transfer rod, samples collected an amount of ice contamination prohibitive to downstream cryo-EM (Figure 3.7B). Presumably, contamination accumulated further within the cryostat (Figure 3.7C-D). However, the high contamination levels on all grids rendered comparisons challenging, and some variation was observed between samples exposed to the same condition[71]. This type of experiment did not allow for decoupling of loading and unloading steps. A potential way to achieve this may be illuminating regions on EM-grids, while they are in the cryostat, with laser intensity high enough to melt away buffer and ice contamination (Figure 3.7E). For example, accumulation within the cryostat would be studied by illuminating different regions at different time points, and comparing the levels of contamination there, presumably accumulated after illumination. However, we found that illumination parameters have to be tuned carefully to avoid burning the support film. Observing the Fourier transform of EM images on pertinent regions did not show any indication of devitrification.

[71] For example, some samples were loaded in a room with humidity control. This did not result in observably reduced contamination, but since the overall contamination was strong on all samples, it remains to be seen if the level of humidity has a relevant effect on our workflow.

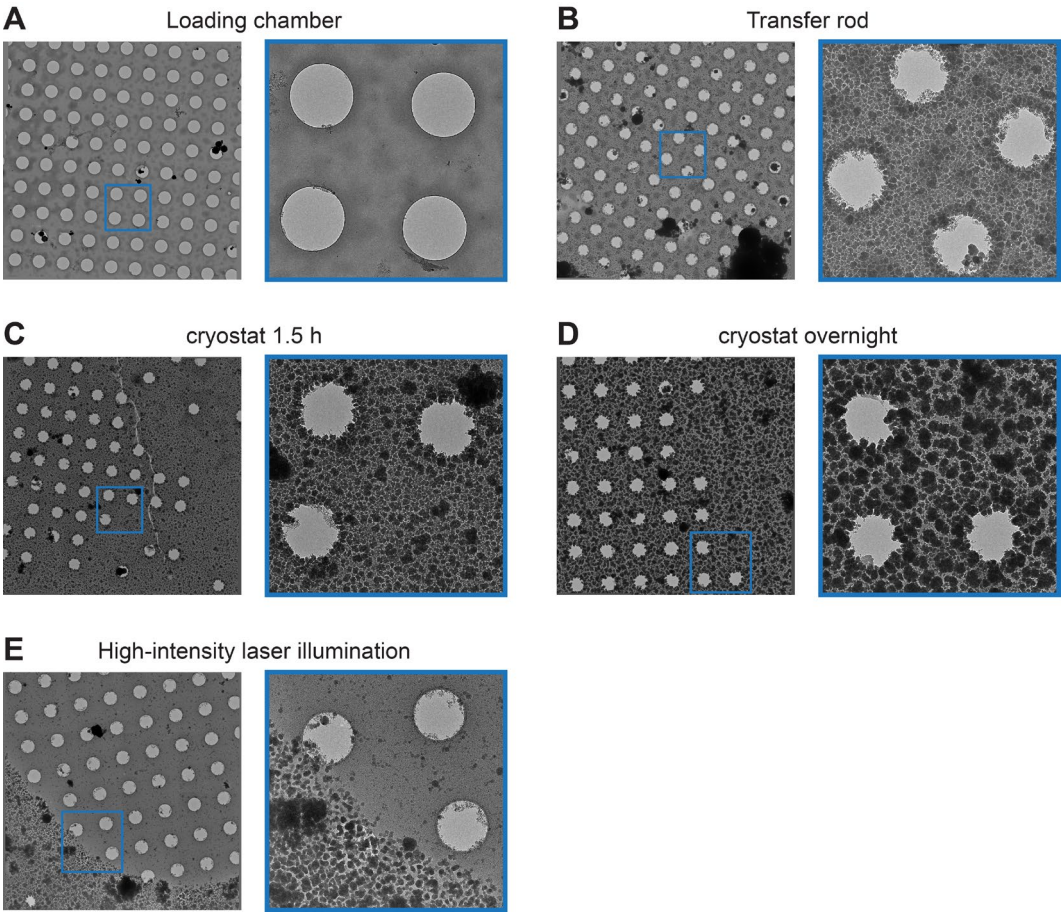

Figure 3.7: Ice contamination when using cryostat, assessed by imaging samples with cryo-EM after performing different steps of the cryostat-workflow. We used 1xPBS, plunge-frozen on holey carbon grids, as test samples. Two images are shown for every condition, the right panel always corresponding to a magnified visualization of the region marked in the left one. ***A:*** *The sample was loaded to the shuttle and returned to grid box, without leaving the liquid nitrogen in the loading chamber.* ***B:*** *The shuttle with mounted samples was pulled up into the transfer rod chamber. Pumping started immediately, lasting for 30 s. After closing the lid of the transfer rod and waiting for additional 30 s, the sample was returned to the grid box.* ***C:*** *The sample was loaded to the cryostat, and remained there for ~1.5 h before unloading.* ***D:*** *Same procedure as C, but the sample remained in the cryostat overnight.* ***E:*** *The sample was loaded to the cryostat, and the region shown here was subjected to high-intensity laser illumination. The bottom left is covered in partially melted ice. The remaining area was presumably fully melted.*

We reasoned that contamination in the transfer rod might arise due to vacuum leakage. Indeed, we observed leakage of the transfer rod chamber[72]. An updated version of the transfer rod, routinely in use at the Aquilos II cryo-FIB-SEM setup at ISTA's Electron Microscopy Facility, showed greatly reduced leakage. However, when we repeated the experiment shown in Figure 3.7B, we observed comparable levels of ice contamination. The most obvious difference between our setup and operation of the Aquilos II cryo-FIB-SEM, where this transfer rod is regularly used without ice contamination being a prevalent problem, is that our shuttle does not contain a cryo-shield to mechanically shield samples from ice contamination. An updated version of the shuttle containing a cryo-shield it currently in development at ISTA's Machine Shop.

[72] After evacuation of the airlock with the lid of the attached transfer rod open, we closed the transfer rod lid, and tracked the pressure with a handheld vacuum gauge, attached to the designated port at the transfer rod vacuum chamber. When venting the airlock, we observed a sudden pressure increase in the transfer rod by a few mbar.

After cooling the cryostat, we typically reached pressure levels around $3*10^{-6}$ mbar. While this is somewhat higher than the 10^{-6} mbar reported elsewhere (Hoffman et al., 2020; Mazal et al., 2025b), on its own, this value does not seem concerning. However, considering that our turbomolecular pump is quite powerful (pumping speed > 50 l/s) for the volume of the cryostat, it is conceivable that it removed invading air from potential leaks fast enough to reach high vacuum, while at the same time introducing humidity to the cryostat. I tested vacuum leaks in the cryostat by monitoring rising pressure after closing the valve between turbomolecular pump and the vacuum gauge connected to the cryostat (VG1 in Figure 3.4A)[73]. Pressure rose by $1.2*10^{-3}$ mbar/min. Exchanging the back plate modified for sample loading for the original one lowered this to $9.8*10^{-4}$ mbar/min, and shutting off the cryostat by closing the valve between it and the vacuum gauge VG1 resulted in $7*10^{-4}$ mbar/min. These values do not seem excessive, but further investigation would be necessary to make dependable statements[74]. We added an additional cold trap placed around the shuttle to the cryostat to mitigate buildup of contamination on samples inside the cryostat. Updated contamination test measurements are pending.

While we hope that the measures we are currently implementing will reduce ice contamination to acceptable levels, it remains to be seen if this type of cryostat is compatible with cryo-CLEM on plunge-frozen samples. Of note, even in the current state, this type of ice contamination does not seem to be prohibitive for fluorescence imaging (Section 3.2.3). However, further evaluation is necessary to assess its effect on optical performance.

3.2.3 Preliminary data using the cryostat

Our primary test sample was fluorescent beads, plunge-frozen on holey carbon EM-grids. Beads allowed for straightforward visualization of the microscope's PSF, including aberrations. I observed pronounced spherical aberrations (Figure 3.8A). Initially, I thought that this might be due to a slight mismatch of the objective's correction collar, set to 0.5, and the viewing window of the cryostat. However, changing the position of the correction collar had surprisingly little effect on the shape of the PSF. Moreover, the SBR was quite low, clearly reduced compared to imaging the same sample type with open cryo-stages. This might be due to ice contamination, the viewing window or the components in the microscope frontend, and further investigation is necessary to identify the sources and improve optical performance. Finally, I observed that the threshold for the optical intensity, at which beads disappeared during cryo-imaging, presumably due to melting, was notably lower than for the Linkam cryo-stage. This might be due to reduced thermal coupling of the sample holder in the cryostat or the absence of convective cooling in vacuum, as recently shown in simulations (Mojiri et al., 2025).

We also imaged B16 cells stained with AFP647-phalloidin, grown on holey carbon film (Figure 3.8B-E). The last experiment we had performed on the Linkam cryo-stage before malfunctioning was an attempt at cryo-PALM on cells co-stained with PaX560-phalloidin and AFP647-phalloidin (Section 3.1.2). Later, we realized that this measurement may have been affected by photoblueing of AFP647, providing a potential alternative pathway to cryo-SMLM. Hence, we aimed to continue investigating this effect, attempting cryo-SMLM on cell samples, despite our cryostat implementation's current shortcomings. The main limitation was light-

[73] Pressure rose to fast that I used only the pre-vacuum pump. To eliminate outgassing effects, I performed these measurements multiple hours after switching on the pump, and repeated them multiple times until the values did not change notably.

[74] Identifying the places of origin for the leaks would require helium sniffing or spraying tests.

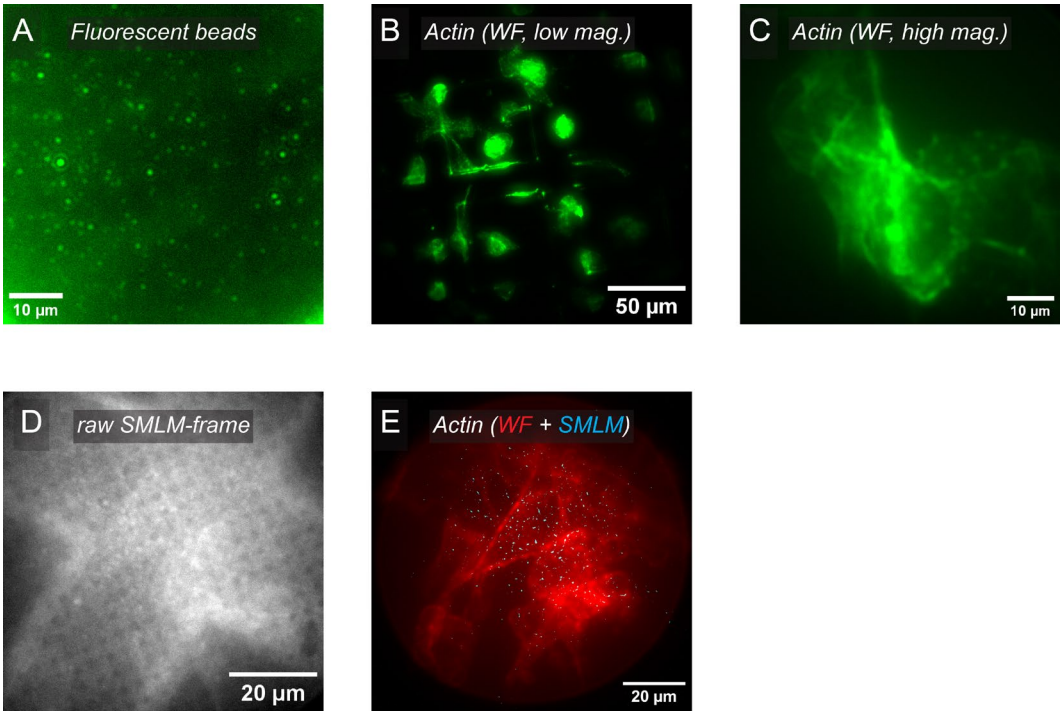

Figure 3.8: Preliminary cryo-fluorescence data acquired on the cryostat. ***A:*** *Fluorescent beads (yellow-green beads, 100 nm diameter) diluted 1:50 in milli-Q water, plunge-frozen on holey carbon EM-grids.* ***B:*** *WF image of B16 cells stained with AFP647-phalloidin, illuminated with 642 nm light and detected in the far-red imaging channel. For this overview image, a 20x objective was used, with the correction collar set to 0.5.* ***C:*** *Same sample as B, imaged with the 63x objective used for subsequent cryo-SMLM measurements.* ***D:*** *Raw frame of a cryo-SMLM experiment (reconstruction shown in E) on the same sample shown in B-C, detecting signal generated by 561 nm illumination in the orange channel. Background stems from support film on the grid bar. This region was chosen since it allowed for increased optical intensity. Switching events, faintly visible above the background, are attributed to photoblueing of AFP647.* ***E:*** *Overlay of widefield image (red; 642 nm illumination, far-red channel) and reconstruction of the same cryo-SMLM experiment as in D (green; 651 nm illumination, orange channel).*

induced devitrification. Typically, I could not apply enough laser power to observe photoblueing without inducing melting, followed by destruction of cellular features, and finally a substantial increase of the fluorescence from the support film, potentially indicating burning. This seemed to be less severe above grid bars, presumably due to increased heat transfer. At points where grid bars intersected, I managed to apply sufficient optical intensity to induce photoswitching[75] in some instances (Figure 3.8D), albeit at low levels and without assessing the devitrification status. Despite elevated background and aberrations, single-molecule localization was attempted (Figure 3.8E). I acquired data for > 20 h, but the active stabilization failed after ~10 h because drifts had exceeded the limits of the piezo stage. Despite these extended acquisition times, the localization density was clearly too low to reconstruct actin arrangements.

These proof-of-principle experiments showed that our cryostat implementation was in principle compatible with cryo-SMLM acquisitions, but data quality is currently limited by optical performance and low devitrification thresholds. Ice contamination, showing prohibitively high levels in cryo-EM, might affect cryo-light microscopy as well. After

[75] I tested illumination with 561 nm light only, or simultaneous 561 nm and 642 nm illumination, always detecting in the orange channel for SMLM measurements. The difference was not clearly notable. Further investigation, potentially testing other dyes, is needed to determine which illumination strategy is most conductive to inducing photoblueing.

implementing ongoing improvements, we will comprehensively evaluate performance of our cryostat for super-resolution cryo-CLEM.

4 Discussion and conclusions

In summary, we have constructed a super-resolution fluorescence microscopy setup, and used it for measurements at RT and cryogenic conditions. At RT, we achieved state-of-the-art camera-based 2D SMLM performance. Additionally, we generated proof-of-principle non-iterative 2D MINFLUX data on a synthetic test sample. Since uncorrected drifts adversely affected initial measurements, we developed a novel scheme to actively stabilize sample position in 3D which led to a publication (Vorlaufer et al., 2025) reprinted in Appendix A. We explored different cryo-stages for imaging near-natively preserved vitrified samples. The open cryo-stages we tested did not provide the mechanical stability conducive to cryo-super-resolution imaging on the nanoscale. Moreover, when using an open cryo-stage for testing fluorophores, assessing cryo-photophysics was hindered by limited acquisition times associated with accumulation of ice contamination. Therefore, we adapted a vacuum cryostat for loading vitrified samples. We performed technical measurements, characterizing thermal and mechanical stability as well as ice contamination. Moreover, we acquired preliminary imaging data. Improvements to the system are ongoing.

Some of the aims laid out at the beginning of the project (Section 1.3) have not yet or have only partially been attained. For enabling fluorescence-guided *in situ* structure analysis – requiring nanoscale 3D resolution and correlation accuracy – on cellular structures, MINFLUX would have to be implemented in an iterative fashion with localization in 3D to reach its full potential. Colocalization of fluorophores, required for correlation via *in situ* fiducials, could be achieved by splitting emission spectra (Gwosch et al., 2020) or detecting fluorescence lifetimes (Masullo et al., 2021; Zähringer et al., 2023). Reliably reaching adequate mechanical stability would necessitate improved passive stability of the setup, associated with laboratory temperature, or actively correcting excitation beam drifts. Pertinent solutions to these issues have been demonstrated, and integrating them in our setup should be a solvable technical task. However, cryo-MINFLUX is not only dependent on the microscopy setup, but also on adequate sample properties.

Identifying suitable fluorophores is a prerequisite for our downstream aims of generating cryo-MINFLUX data and establishing a high-accuracy cryo-CLEM[76] pipeline. We did not find fluorophores with adequate photoswitching properties for our high-resolution cryo-SMLM efforts. Since data did not look promising in camera-based cryo-SMLM, we did not attempt cryo-MINFLUX. Cryo-photophysics is limiting the field of cryo-super-resolution microscopy overall (Dahlberg and Moerner, 2021). Fluorophores explored for cryo-SMLM typically provided an increased photon budget after freezing, but in many scenarios, high-resolution reconstructions were limited to sparse, isolated particles due to reduced off-switching efficiency. Further efforts on developing optimized cryo-fluorophores, investigating photoswitching mechanisms at cryogenic temperatures, and potentially large-scale screening may be necessary for pushing cryo-SMLM forward.

While these areas are not our focus, adaptations to acquisition workflows might enable cryo-SMLM on previously inadequate fluorophores. Lowering sample temperature by using liquid helium alters photoswitching (Hoffman et al., 2020) and allows for increased optical intensity before devitrification, albeit at considerably increased overhead. Furthermore, it has been shown that spectroscopic investigation can reveal more efficient cryo-photoswitching

[76] Correlation accuracy is not necessarily limited by optical resolution, but correcting non-linear deformations on a fine spatial scale requires a correspondingly high local density of correlation points, and hence cryo-super-resolution.

pathways (Perez et al., 2024). Applying an electric potential to samples can bias switching kinetics at RT (Yang et al., 2024, 2023). We reproduced electrochemical fluorescence modulation of GFP at RT, but deprioritized exploration at cryogenic temperature due to the associated engineering overhead[77]. Fluorescence modulation by magnetic fields (Hayward et al., 2023) might be more straightforward to implement, but the effect has yet to be investigated on the single-molecule level.

Introducing an additional parameter for assigning localizations to molecular targets can be a powerful concept, realized in the COLD (Weisenburger et al., 2017) and RESI (Reinhardt et al., 2023) approaches. Using polarization-sensitive detection enabled the reconstruction of up to 7 sites on sparse particles at nm-scale resolution via cryo-SMLM (Mazal et al., 2025b). Implementing more sophisticated schemes for measuring molecular orientation (Rimoli et al., 2022; Wu et al., 2022; Zhang et al., 2023) might increase achievable localization densities. Moreover, overlaying excitation light with linearly polarized de-excitation would restrict detection to emitters exhibiting a particular orientation. An implementation using polarized STED was limited by cryo-photophysics (Hulleman et al., 2021a), but cryo-RESOLFT could be an interesting, currently unexplored alternative. Finally, at temperatures provided by liquid helium, heterogeneous spectral signatures might become a criterion for distinguishing emitters. However, great care would have to be taken to avoid heating the sample through optical illumination.

Cryo-SMLM data quality is affected by intrinsic fluorophore properties as well as the cryo-microscopy platform. Often, reaching appropriate levels of photoswitching is prohibited by optical intensities at which devitrification sets in. Hence, strong thermal coupling between sample and cryogen is imperative. At the same time, local heating via light absorption of the sample itself or the sample carrier (e.g., the support film of EM-grids) may induce devitrification. Metal-coated support films restrict downstream cryo-EM acquisition to grid holes, but they have proven themselves useful for improving cryo-super-resolution microscopy acquisitions. Removing the support film after freezing via cryo-FIB-milling might be an appealing alternative strategy.

Optical intensity levels compatible with vitrified samples may induce photoswitching with highly extended on- and off-times of fluorophores. This could enable high-fidelity reconstruction of molecular arrangements using cryo-SMLM, but necessitates prolonged acquisition times. Since the accumulation of ice contamination in open cryo-stages typically limits measurements to few hours, experiments may have to be terminated before the majority of fluorophores was activated. Using a vacuum cryostat might improve cryo-SMLM localization density on the same fluorophores and sample platforms. We acquired proof-of-principle data at extended acquisition times, but further improvements to the cryostat integration will be necessary for adequate performance.

Taken together, these factors will be decisive for determining whether MINFLUX or camera-based SMLM is a more suitable platform for realizing the vision of single-digit nm 3D localization precision and correlation accuracy. For example, fluorophores providing high switching contrast and adequate photoswitching kinetics may be amenable to cryo-MINFLUX, even if they yield only moderate photon budgets. On the other hand, if tens of thousands of

[77] The approach would require an electrically conductive sample carrier with a contact point for an electrode, and another contact point at the buffer. The electrical conductivity of vitrified buffer and its implications on electrochemical fluorescence modulation are not well characterized. Cryo-immersion might be a promising platform to realize the approach because typical immersion media remain liquid, albeit at high viscosity, during imaging, but their solidification temperature is often close to the devitrification threshold (Faul et al., 2025) which may impact cryo-SMLM data acquisition.

photons are detected per emission event, camera-based SMLM could achieve nanoscale localization precision at increased throughput, reduced demands on mechanical stability, and smaller hardware overhead. To my mind, the issue of localization accuracy of cryo-SMLM is not fully appreciated in the field, with a recent study showing biases of 10s of nm (Li et al., 2025). In particular when using plunge-frozen samples, a tilted or non-flat sample surface might induce considerable localization bias. Since aberrations affect MINFLUX and camera-based SMLM differently, this could become a somewhat subtle yet important argument for a particular technique.

Despite the discussed approaches for improving cryo-SMLM data quality, and ongoing efforts in various research groups, it is not clear whether the general aim we defined in the beginning – using cryo-fluorescence signal to assign molecular identity to cryo-electron densities at the single-molecule level – will become attainable in the near future. However, scientific insights might still be generated when accepting compromises to this ambitious aim. For example, as mentioned in Section 1.2.1, the effect of chemical fixation depends to a large extent on the structure of interest. Therefore, in some instances, fluorescence-guided structure analysis could be realized by performing super-resolution fluorescence microscopy on mildly chemically fixed samples at RT, before vitrification and cryo-ET. This workflow would be a comparatively straightforward way to achieve nanoscale optical resolution, as has become state-of-the-art for RT-SMLM on amenable targets (Section 1.2.3). Non-linear distortions during freezing may hamper correlation accuracy, and would have to be thoroughly characterized in pilot experiments. It stands to reason that vitrification might be less perturbative than freeze-substitution, which resulted in correlation accuracies better than 100 nm using *in situ* fiducials (Hoffman et al., 2020). The Arp2/3 complex, associated with actin branch junctions, has been reconstructed at sub-nm resolution from *in situ* cryo-ET data, acquired on mildly chemically fixed, membrane-extracted cells (Fäßler et al., 2020). Hence, this could be a suitable platform for benchmarking correlation of RT-SMLM to cryo-ET. In case these results are promising, the approach could then be applied to targets that are incompatible with current techniques for *in situ* structure determination, in order to generate novel biological insights. While this approach requires thorough characterization of fixation artifacts and would not be broadly generalizable, it could be a bridge technology until cryo-SMLM data quality improves sufficiently.

Using super-resolution cryo-CLEM is not the only strategy to identify target particles for *in situ* structure analysis. Potent electron-dense tags would considerably simplify workflows by natively providing nanoscale imaging resolution, omitting additional imaging steps, and avoiding registration of datasets. To date, the tags' large sizes and limitations related to labeling have hindered their broad application, but future realizations might facilitate electron-tag-guided *in situ* structure analysis. Distinctive advantages of light microscopy remain the increased field of view and imaging depth compared to cryo-ET. Hence, it is conceivable that cryo-CLEM will remain widely used for identifying ROIs for cryo-FIB-milling and cryo-ET, potentially with the fluorescence microscopy unit integrated in a cryo-EM setup, while electron-dense tags might enable particle picking on a wide range of targets.

Advancements of *in situ* cryo-EM/cryo-ET hardware and acquisition workflows will critically affect the choice of molecularly specific tags as well. After all, a major motivation for using tags is that the low SNR of cryo-ET prevents direct identification of particles in many instances. In the future, contrast will likely be enhanced by innovations in hardware, such as improved electron detectors or laser phase plates, as well as optimized acquisition schemes. Resulting data, exhibiting increased SNRs, would allow for pinpointing of smaller particles

without tags. Accordingly, the size of electron-dense tags could be reduced while retaining specificity of the signal they generate in cryo-ET.

Revealing biomolecular identity, localization, structure, and copy number of all relevant constituents of complex samples requires tremendous innovation in bioimaging technology. Due to their distinct characteristics, it stands to reason that fluorescent and electron-dense tags, in combination with refined cryo-ET acquisitions, may emerge as complementary approaches for realizing the longstanding vision of visual proteomics. Whatever the outcome of these developments may be, it is safe to say that technological innovation will continue to drive scientific progress in intriguing ways.

References

Abbe, E., 1873. Beiträge zur Theorie des Mikroskops und der mikroskopischen Wahrnehmung. Arch. Für Mikrosk. Anat. 9, 413–468. https://doi.org/10.1007/BF02956173

Ando, R., Mizuno, H., Miyawaki, A., 2004. Regulated Fast Nucleocytoplasmic Shuttling Observed by Reversible Protein Highlighting. Science 306, 1370–1373. https://doi.org/10.1126/science.1102506

Arnold, J., Mahamid, J., Lucic, V., de Marco, A., Fernandez, J.-J., Laugks, T., Mayer, T., Hyman, A.A., Baumeister, W., Plitzko, J.M., 2016. Site-Specific Cryo-focused Ion Beam Sample Preparation Guided by 3D Correlative Microscopy. Biophys. J. 110, 860–869. https://doi.org/10.1016/j.bpj.2015.10.053

Asano, S., Fukuda, Y., Beck, F., Aufderheide, A., Förster, F., Danev, R., Baumeister, W., 2015. A molecular census of 26S proteasomes in intact neurons. Science 347, 439–442. https://doi.org/10.1126/science.1261197

Axelrod, J.J., Zhang, J.T., Petrov, P.N., Glaeser, R.M., Müller, H., 2024. Modern approaches to improving phase contrast electron microscopy. Curr. Opin. Struct. Biol. 86, 102805. https://doi.org/10.1016/j.sbi.2024.102805

Balzarotti, F., Eilers, Y., Gwosch, K.C., Gynnå, A.H., Westphal, V., Stefani, F.D., Elf, J., Hell, S.W., 2017. Nanometer resolution imaging and tracking of fluorescent molecules with minimal photon fluxes. Science 355, 606–612. https://doi.org/10.1126/science.aak9913

Bäuerlein, F.J.B., Baumeister, W., 2021. Towards Visual Proteomics at High Resolution. J. Mol. Biol., From Protein Sequence to Structure at Warp Speed: How Alphafold Impacts Biology 433, 167187. https://doi.org/10.1016/j.jmb.2021.167187

Beck, M., Covino, R., Hänelt, I., Müller-McNicoll, M., 2024. Understanding the cell: Future views of structural biology. Cell 187, 545–562. https://doi.org/10.1016/j.cell.2023.12.017

Berger, C., Ravelli, R.B.G., López-Iglesias, C., Peters, P.J., 2021. Endocytosed nanogold fiducials for improved in-situ cryo–electron tomography tilt-series alignment. J. Struct. Biol. 213, 107698. https://doi.org/10.1016/j.jsb.2021.107698

Betzig, E., Patterson, G.H., Sougrat, R., Lindwasser, O.W., Olenych, S., Bonifacino, J.S., Davidson, M.W., Lippincott-Schwartz, J., Hess, H.F., 2006. Imaging Intracellular Fluorescent Proteins at Nanometer Resolution. Science 313, 1642–1645. https://doi.org/10.1126/science.1127344

Böning, D., Wieser, F.-F., Sandoghdar, V., 2021. Polarization-Encoded Colocalization Microscopy at Cryogenic Temperatures. ACS Photonics 8, 194–201. https://doi.org/10.1021/acsphotonics.0c01201

Brakemann, T., Stiel, A.C., Weber, G., Andresen, M., Testa, I., Grotjohann, T., Leutenegger, M., Plessmann, U., Urlaub, H., Eggeling, C., Wahl, M.C., Hell, S.W., Jakobs, S., 2011. A reversibly photoswitchable GFP-like protein with fluorescence excitation decoupled from switching. Nat. Biotechnol. 29, 942–947. https://doi.org/10.1038/nbt.1952

Briggs, J.A., 2013. Structural biology in situ—the potential of subtomogram averaging. Curr. Opin. Struct. Biol., Theory and simulation / Macromolecular assemblies 23, 261–267. https://doi.org/10.1016/j.sbi.2013.02.003

Burkel, B.M., von Dassow, G., Bement, W.M., 2007. Versatile fluorescent probes for actin filaments based on the actin-binding domain of utrophin. Cell Motil. 64, 822–832. https://doi.org/10.1002/cm.20226

Chang, Y.-W., Chen, S., Tocheva, E.I., Treuner-Lange, A., Löbach, S., Søgaard-Andersen, L., Jensen, G.J., 2014. Correlated cryogenic photoactivated localization microscopy and cryo-electron tomography. Nat. Methods 11, 737–739. https://doi.org/10.1038/nmeth.2961

Clarke, N.I., Royle, S.J., 2018. FerriTag is a new genetically-encoded inducible tag for correlative light-electron microscopy. Nat. Commun. 9, 2604. https://doi.org/10.1038/s41467-018-04993-0

Cnossen, J., Hinsdale, T., Thorsen, R.Ø., Siemons, M., Schueder, F., Jungmann, R., Smith, C.S., Rieger, B., Stallinga, S., 2020. Localization microscopy at doubled precision with patterned illumination. Nat. Methods 17, 59–63. https://doi.org/10.1038/s41592-019-0657-7

Dahan, I., Sorrentino, S., Boujemaa-Paterski, R., Medalia, O., 2018. Tiopronin-Protected Gold Nanoparticles as a Potential Marker for Cryo-EM and Tomography. Structure 26, 1408-1413.e3. https://doi.org/10.1016/j.str.2018.06.009

Dahlberg, P.D., Moerner, W.E., 2021. Cryogenic Super-Resolution Fluorescence and Electron Microscopy Correlated at the Nanoscale. Annu. Rev. Phys. Chem. 72, 253–278. https://doi.org/10.1146/annurev-physchem-090319-051546

Dahlberg, P.D., Perez, D., Hecksel, C.W., Chiu, W., Moerner, W.E., 2022. Metallic support films reduce optical heating in cryogenic correlative light and electron tomography. J. Struct. Biol. 214, 107901. https://doi.org/10.1016/j.jsb.2022.107901

Dahlberg, P.D., Sartor, A.M., Wang, J., Saurabh, S., Shapiro, L., Moerner, W.E., 2018. Identification of PAmKate as a Red Photoactivatable Fluorescent Protein for Cryogenic Super-Resolution Imaging. J. Am. Chem. Soc. 140, 12310–12313. https://doi.org/10.1021/jacs.8b05960

Dahlberg, P.D., Saurabh, S., Sartor, A.M., Wang, J., Mitchell, P.G., Chiu, W., Shapiro, L., Moerner, W.E., 2020. Cryogenic single-molecule fluorescence annotations for electron tomography reveal in situ organization of key proteins in *Caulobacter*. Proc. Natl. Acad. Sci. 117, 13937–13944. https://doi.org/10.1073/pnas.2001849117

de Boer, P., Hoogenboom, J.P., Giepmans, B.N.G., 2015. Correlated light and electron microscopy: ultrastructure lights up! Nat. Methods 12, 503–513. https://doi.org/10.1038/nmeth.3400

de Teresa-Trueba, I., Goetz, S.K., Mattausch, A., Stojanovska, F., Zimmerli, C.E., Toro-Nahuelpan, M., Cheng, D.W.C., Tollervey, F., Pape, C., Beck, M., Diz-Muñoz, A., Kreshuk, A., Mahamid, J., Zaugg, J.B., 2023. Convolutional networks for supervised mining of molecular patterns within cellular context. Nat. Methods 20, 284–294. https://doi.org/10.1038/s41592-022-01746-2

Deguchi, T., Iwanski, M.K., Schentarra, E.-M., Heidebrecht, C., Schmidt, L., Heck, J., Weihs, T., Schnorrenberg, S., Hoess, P., Liu, S., Chevyreva, V., Noh, K.-M., Kapitein, L.C., Ries, J., 2023. Direct observation of motor protein stepping in living cells using MINFLUX. Science 379, 1010–1015. https://doi.org/10.1126/science.ade2676

Dempsey, G.T., Vaughan, J.C., Chen, K.H., Bates, M., Zhuang, X., 2011. Evaluation of fluorophores for optimal performance in localization-based super-resolution imaging. Nat. Methods 8, 1027–1036. https://doi.org/10.1038/nmeth.1768

DeRosier, D.J., 2021. Where in the cell is my protein? Q. Rev. Biophys. 54, e9. https://doi.org/10.1017/S003358352100007X

Dertinger, T., Colyer, R., Iyer, G., Weiss, S., Enderlein, J., 2009. Fast, background-free, 3D super-resolution optical fluctuation imaging (SOFI). Proc. Natl. Acad. Sci. 106, 22287–22292. https://doi.org/10.1073/pnas.0907866106

Enderlein, J., Toprak, E., Selvin, P.R., 2006. Polarization effect on position accuracy of fluorophore localization. Opt. Express 14, 8111–8120. https://doi.org/10.1364/OE.14.008111

Engelhardt, J., Keller, J., Hoyer, P., Reuss, M., Staudt, T., Hell, S.W., 2011. Molecular Orientation Affects Localization Accuracy in Superresolution Far-Field Fluorescence Microscopy. Nano Lett. 11, 209–213. https://doi.org/10.1021/nl103472b

Faoro, R., Bassu, M., Mejia, Y.X., Stephan, T., Dudani, N., Boeker, C., Jakobs, S., Burg, T.P., 2018. Aberration-corrected cryoimmersion light microscopy. Proc. Natl. Acad. Sci. 115, 1204–1209. https://doi.org/10.1073/pnas.1717282115

Fäßler, F., Dimchev, G., Hodirnau, V.-V., Wan, W., Schur, F.K.M., 2020. Cryo-electron tomography structure of Arp2/3 complex in cells reveals new insights into the branch junction. Nat. Commun. 11, 6437. https://doi.org/10.1038/s41467-020-20286-x

Faul, N., Chen, S.-Y., Lamberz, C., Bruckner, M., Dienemann, C., Burg, T.P., 2025. Cryo-iCLEM: Cryo correlative light and electron microscopy with immersion objectives. J. Struct. Biol. 108179. https://doi.org/10.1016/j.jsb.2025.108179

Fung, H.K.H., Hayashi, Y., Salo, V.T., Babenko, A., Zagoriy, I., Brunner, A., Ellenberg, J., Müller, C.W., Cuylen-Haering, S., Mahamid, J., 2023. Genetically encoded multimeric tags for subcellular protein localization in cryo-EM. Nat. Methods 20, 1900–1908. https://doi.org/10.1038/s41592-023-02053-0

Furubayashi, T., Ishida, K., Kashida, H., Nakata, E., Morii, T., Matsushita, M., Fujiyoshi, S., 2019. Nanometer Accuracy in Cryogenic Far-Field Localization Microscopy of Individual Molecules. J. Phys. Chem. Lett. 10, 5841–5846. https://doi.org/10.1021/acs.jpclett.9b02184

Geismann, M.K., Gomez-Segalas, A., Passera, A., Shirzadian, M., Balzarotti, F., 2024. A Fast Interferometric Beam Shaper for Multi-Emitter 3D MINFLUX. https://doi.org/10.1101/2023.12.09.570565

Giske, A., 2007. CryoSTED microscopy - a new spectroscopic approach for improving the resolution of STED microscopy using low temperature (doctoral thesis). Ruperto-Carola University of Heidelberg, Heidelberg, Germany.

Grabner, C.P., Jansen, I., Neef, J., Weihs, T., Schmidt, R., Riedel, D., Wurm, C.A., Moser, T., 2022. Resolving the molecular architecture of the photoreceptor active zone with 3D-MINFLUX. Sci. Adv. 8, eabl7560. https://doi.org/10.1126/sciadv.abl7560

Grimm, J.B., English, B.P., Choi, H., Muthusamy, A.K., Mehl, B.P., Dong, P., Brown, T.A., Lippincott-Schwartz, J., Liu, Z., Lionnet, T., Lavis, L.D., 2016. Bright photoactivatable fluorophores for single-molecule imaging. Nat. Methods 13, 985–988. https://doi.org/10.1038/nmeth.4034

Grimm, J.B., Lavis, L.D., 2022. Caveat fluorophore: an insiders' guide to small-molecule fluorescent labels. Nat. Methods 19, 149–158. https://doi.org/10.1038/s41592-021-01338-6

Grotjohann, T., Testa, I., Leutenegger, M., Bock, H., Urban, N.T., Lavoie-Cardinal, F., Willig, K.I., Eggeling, C., Jakobs, S., Hell, S.W., 2011. Diffraction-unlimited all-optical imaging and writing with a photochromic GFP. Nature 478, 204–208. https://doi.org/10.1038/nature10497

Grotjohann, T., Testa, I., Reuss, M., Brakemann, T., Eggeling, C., Hell, S.W., Jakobs, S., 2012. rsEGFP2 enables fast RESOLFT nanoscopy of living cells. eLife 1, e00248. https://doi.org/10.7554/eLife.00248

Gu, L., Li, Y., Zhang, S., Xue, Y., Li, W., Li, D., Xu, T., Ji, W., 2019. Molecular resolution imaging by repetitive optical selective exposure. Nat. Methods 16, 1114–1118. https://doi.org/10.1038/s41592-019-0544-2

Gunewardene, M.S., Subach, F.V., Gould, T.J., Penoncello, G.P., Gudheti, M.V., Verkhusha, V.V., Hess, S.T., 2011. Superresolution Imaging of Multiple Fluorescent Proteins with Highly Overlapping Emission Spectra in Living Cells. Biophys. J. 101, 1522–1528. https://doi.org/10.1016/j.bpj.2011.07.049

Gustafsson, N., Culley, S., Ashdown, G., Owen, D.M., Pereira, P.M., Henriques, R., 2016. Fast live-cell conventional fluorophore nanoscopy with ImageJ through super-resolution radial fluctuations. Nat. Commun. 7, 12471. https://doi.org/10.1038/ncomms12471

Gwosch, K.C., Balzarotti, F., Pape, J.K., Hoess, P., Ellenberg, J., Ries, J., Matti, U., Schmidt, R., Sahl, S.J., Hell, S.W., 2023. Reply to: Assessment of 3D MINFLUX data for quantitative structural biology in cells. Nat. Methods 20, 52–54. https://doi.org/10.1038/s41592-022-01695-w

Gwosch, K.C., Pape, J.K., Balzarotti, F., Hoess, P., Ellenberg, J., Ries, J., Hell, S.W., 2020. MINFLUX nanoscopy delivers 3D multicolor nanometer resolution in cells. Nat. Methods 17, 217–224. https://doi.org/10.1038/s41592-019-0688-0

Harke, B., Keller, J., Ullal, C.K., Westphal, V., Schönle, A., Hell, S.W., 2008. Resolution scaling in STED microscopy. Opt. Express 16, 4154–4162. https://doi.org/10.1364/OE.16.004154

Hauser, M., Wojcik, M., Kim, D., Mahmoudi, M., Li, W., Xu, K., 2017. Correlative Super-Resolution Microscopy: New Dimensions and New Opportunities. Chem. Rev. 117, 7428–7456. https://doi.org/10.1021/acs.chemrev.6b00604

Hayward, R.F., Rai, A., Lazzari-Dean, J.R., Lefebvre, A.E.Y.T., York, A.G., Ingaramo, M., 2023. Magnetic control of the brightness of fluorescent proteins. Github.io.

Heilemann, M., van de Linde, S., Schüttpelz, M., Kasper, R., Seefeldt, B., Mukherjee, A., Tinnefeld, P., Sauer, M., 2008. Subdiffraction-Resolution Fluorescence Imaging with Conventional Fluorescent Probes. Angew. Chem. Int. Ed. 47, 6172–6176. https://doi.org/10.1002/anie.200802376

Helmerich, D.A., Beliu, G., Matikonda, S.S., Schnermann, M.J., Sauer, M., 2021. Photoblueing of organic dyes can cause artifacts in super-resolution microscopy. Nat. Methods 18, 253–257. https://doi.org/10.1038/s41592-021-01061-2

Helmerich, D.A., Budiarta, M., Taban, D., Doose, S., Beliu, G., Sauer, M., 2024. PCNA as Protein-Based Nanoruler for Sub-10 nm Fluorescence Imaging. Adv. Mater. 36, 2310104. https://doi.org/10.1002/adma.202310104

Hess, S.T., Girirajan, T.P.K., Mason, M.D., 2006. Ultra-High Resolution Imaging by Fluorescence Photoactivation Localization Microscopy. Biophys. J. 91, 4258–4272. https://doi.org/10.1529/biophysj.106.091116

Heydarian, H., Joosten, M., Przybylski, A., Schueder, F., Jungmann, R., Werkhoven, B. van, Keller-Findeisen, J., Ries, J., Stallinga, S., Bates, M., Rieger, B., 2021. 3D particle averaging and detection of macromolecular symmetry in localization microscopy. Nat. Commun. 12, 2847. https://doi.org/10.1038/s41467-021-22006-5

Heydarian, H., Schueder, F., Strauss, M.T., van Werkhoven, B., Fazel, M., Lidke, K.A., Jungmann, R., Stallinga, S., Rieger, B., 2018. Template-free 2D particle fusion in

localization microscopy. Nat. Methods 15, 781–784. https://doi.org/10.1038/s41592-018-0136-6

Hinterer, F., Schneider, M.C., Hubmer, S., López-Martinez, M., Zelger, P., Jesacher, A., Ramlau, R., Schütz, G.J., 2022. Robust and bias-free localization of individual fixed dipole emitters achieving the Cramér Rao bound for applications in cryo-single molecule localization microscopy. PLOS ONE 17, e0263500. https://doi.org/10.1371/journal.pone.0263500

Hoffman, D.P., Shtengel, G., Xu, C.S., Campbell, K.R., Freeman, M., Wang, L., Milkie, D.E., Pasolli, H.A., Iyer, N., Bogovic, J.A., Stabley, D.R., Shirinifard, A., Pang, S., Peale, D., Schaefer, K., Pomp, W., Chang, C.-L., Lippincott-Schwartz, J., Kirchhausen, T., Solecki, D.J., Betzig, E., Hess, H.F., 2020. Correlative three-dimensional super-resolution and block-face electron microscopy of whole vitreously frozen cells. Science 367, eaaz5357. https://doi.org/10.1126/science.aaz5357

Hofmann, M., Eggeling, C., Jakobs, S., Hell, S.W., 2005. Breaking the diffraction barrier in fluorescence microscopy at low light intensities by using reversibly photoswitchable proteins. Proc. Natl. Acad. Sci. 102, 17565–17569. https://doi.org/10.1073/pnas.0506010102

Huebinger, J., Grecco, H., Masip, M.E., Christmann, J., Fuhr, G.R., Bastiaens, P.I.H., 2021. Ultrarapid cryo-arrest of living cells on a microscope enables multiscale imaging of out-of-equilibrium molecular patterns. Sci. Adv. 7, eabk0882. https://doi.org/10.1126/sciadv.abk0882

Hulleman, C.N., Li, W., Gregor, I., Rieger, B., Enderlein, J., 2018. Photon Yield Enhancement of Red Fluorophores at Cryogenic Temperatures. ChemPhysChem 19, 1774–1780. https://doi.org/10.1002/cphc.201800131

Hulleman, C.N., Moerland, R.J., Stallinga, S., Rieger, B., 2021a. Polarized stimulated-emission depletion and dark-state lifetime at vacuum and cryogenic temperature conditions. Phys. Rev. A 104, 063516. https://doi.org/10.1103/PhysRevA.104.063516

Hulleman, C.N., Thorsen, R.Ø., Kim, E., Dekker, C., Stallinga, S., Rieger, B., 2021b. Simultaneous orientation and 3D localization microscopy with a Vortex point spread function. Nat. Commun. 12, 5934. https://doi.org/10.1038/s41467-021-26228-5

Irgen-Gioro, S., Yoshida, S., Walling, V., Chong, S., 2022. Fixation can change the appearance of phase separation in living cells. eLife 11, e79903. https://doi.org/10.7554/eLife.79903

Jahr, W., Velicky, P., Danzl, J.G., 2020. Strategies to maximize performance in STimulated Emission Depletion (STED) nanoscopy of biological specimens. Methods, Progress in Super-resolution Fluorescence Microscopy 174, 27–41. https://doi.org/10.1016/j.ymeth.2019.07.019

Jouchet, P., Cabriel, C., Bourg, N., Bardou, M., Poüs, C., Fort, E., Lévêque-Fort, S., 2021. Nanometric axial localization of single fluorescent molecules with modulated excitation. Nat. Photonics 15, 297–304. https://doi.org/10.1038/s41566-020-00749-9

Jungmann, R., Avendaño, M.S., Woehrstein, J.B., Dai, M., Shih, W.M., Yin, P., 2014. Multiplexed 3D cellular super-resolution imaging with DNA-PAINT and Exchange-PAINT. Nat. Methods 11, 313–318. https://doi.org/10.1038/nmeth.2835

Jungmann, R., Steinhauer, C., Scheible, M., Kuzyk, A., Tinnefeld, P., Simmel, F.C., 2010. Single-Molecule Kinetics and Super-Resolution Microscopy by Fluorescence Imaging of Transient Binding on DNA Origami. Nano Lett. 10, 4756–4761. https://doi.org/10.1021/nl103427w

Kirchweger, P., Mullick, D., Swain, P.P., Wolf, S.G., Elbaum, M., 2023. Correlating cryo-super resolution radial fluctuations and dual-axis cryo-scanning transmission electron tomography to bridge the light-electron resolution gap. J. Struct. Biol. 215, 107982. https://doi.org/10.1016/j.jsb.2023.107982

Klar, T.A., Hell, S.W., 1999. Subdiffraction resolution in far-field fluorescence microscopy. Opt. Lett. 24, 954–956. https://doi.org/10.1364/OL.24.000954

Klar, T.A., Jakobs, S., Dyba, M., Egner, A., Hell, S.W., 2000. Fluorescence microscopy with diffraction resolution barrier broken by stimulated emission. Proc. Natl. Acad. Sci. 97, 8206–8210. https://doi.org/10.1073/pnas.97.15.8206

Korogod, N., Petersen, C.C., Knott, G.W., 2015. Ultrastructural analysis of adult mouse neocortex comparing aldehyde perfusion with cryo fixation. eLife 4, e05793. https://doi.org/10.7554/eLife.05793

Kounatidis, I., Stanifer, M.L., Phillips, M.A., Paul-Gilloteaux, P., Heiligenstein, X., Wang, H., Okolo, C.A., Fish, T.M., Spink, M.C., Stuart, D.I., Davis, I., Boulant, S., Grimes, J.M., Dobbie, I.M., Harkiolaki, M., 2020. 3D Correlative Cryo-Structured Illumination Fluorescence and Soft X-ray Microscopy Elucidates Reovirus Intracellular Release Pathway. Cell 182, 515-530.e17. https://doi.org/10.1016/j.cell.2020.05.051

Last, M.G.F., Tuijtel, M.W., Voortman, L.M., Sharp, T.H., 2023. Selecting optimal support grids for super-resolution cryogenic correlated light and electron microscopy. Sci. Rep. 13, 8270. https://doi.org/10.1038/s41598-023-35590-x

Leake, M.C., Quinn, S.D., 2023. A guide to small fluorescent probes for single-molecule biophysics. Chem. Phys. Rev. 4, 011302. https://doi.org/10.1063/5.0131663

Lelek, M., Gyparaki, M.T., Beliu, G., Schueder, F., Griffié, J., Manley, S., Jungmann, R., Sauer, M., Lakadamyali, M., Zimmer, C., 2021. Single-molecule localization microscopy. Nat. Rev. Methods Primer 1, 1–27. https://doi.org/10.1038/s43586-021-00038-x

Lew, M.D., Backlund, M.P., Moerner, W.E., 2013. Rotational Mobility of Single Molecules Affects Localization Accuracy in Super-Resolution Fluorescence Microscopy. Nano Lett. 13, 3967–3972. https://doi.org/10.1021/nl304359p

Li, H., Metskas, L.A., Huang, F., 2025. Systematic Characterization of Optical Aberrations Reveals Cryo-FLM Localization Fidelity. https://doi.org/10.1101/2025.07.25.666845

Li, S., Jia, X., Niu, T., Zhang, X., Qi, C., Xu, W., Deng, H., Sun, F., Ji, G., 2023. HOPE-SIM, a cryo-structured illumination fluorescence microscopy system for accurately targeted cryo-electron tomography. Commun. Biol. 6, 1–12. https://doi.org/10.1038/s42003-023-04850-x

Li, W., Stein, S.C., Gregor, I., Enderlein, J., 2015. Ultra-stable and versatile widefield cryo-fluorescence microscope for single-molecule localization with sub-nanometer accuracy. Opt. Express 23, 3770. https://doi.org/10.1364/OE.23.003770

Li, Y., Mund, M., Hoess, P., Deschamps, J., Matti, U., Nijmeijer, B., Sabinina, V.J., Ellenberg, J., Schoen, I., Ries, J., 2018. Real-time 3D single-molecule localization using experimental point spread functions. Nat. Methods 15, 367–369. https://doi.org/10.1038/nmeth.4661

Lincoln, R., Bossi, M.L., Remmel, M., D'Este, E., Butkevich, A.N., Hell, S.W., 2022. A general design of caging-group-free photoactivatable fluorophores for live-cell nanoscopy. Nat. Chem. 14, 1013–1020. https://doi.org/10.1038/s41557-022-00995-0

Liu, B., Xue, Y., Zhao, W., Chen, Y., Fan, C., Gu, L., Zhang, Y., Zhang, X., Sun, L., Huang, X., Ding, W., Sun, F., Ji, W., Xu, T., 2015. Three-dimensional super-resolution protein

localization correlated with vitrified cellular context. Sci. Rep. 5, 13017. https://doi.org/10.1038/srep13017
Liu, S., Hoess, P., Ries, J., 2022. Super-Resolution Microscopy for Structural Cell Biology. Annu. Rev. Biophys. 51, 301–326. https://doi.org/10.1146/annurev-biophys-102521-112912
Liu, S., Huh, H., Lee, S.-H., Huang, F., 2020. Three-Dimensional Single-Molecule Localization Microscopy in Whole-Cell and Tissue Specimens. Annu. Rev. Biomed. Eng. 22, 155–184. https://doi.org/10.1146/annurev-bioeng-060418-052203
Lucas, B.A., Himes, B.A., Xue, L., Grant, T., Mahamid, J., Grigorieff, N., 2021. Locating macromolecular assemblies in cells by 2D template matching with cisTEM. eLife 10, e68946. https://doi.org/10.7554/eLife.68946
Lucas, B.A., Zhang, K., Loerch, S., Grigorieff, N., 2022. In situ single particle classification reveals distinct 60S maturation intermediates in cells. eLife 11, e79272. https://doi.org/10.7554/eLife.79272
Mahamid, J., Pfeffer, S., Schaffer, M., Villa, E., Danev, R., Kuhn Cuellar, L., Förster, F., Hyman, A.A., Plitzko, J.M., Baumeister, W., 2016. Visualizing the molecular sociology at the HeLa cell nuclear periphery. Science 351, 969–972. https://doi.org/10.1126/science.aad8857
Mantovanelli, A.M.R., Glushonkov, O., Adam, V., Wulffelé, J., Thédié, D., Byrdin, M., Gregor, I., Nevskyi, O., Enderlein, J., Bourgeois, D., 2023. Photophysical Studies at Cryogenic Temperature Reveal a Novel Photoswitching Mechanism of rsEGFP2. J. Am. Chem. Soc. https://doi.org/10.1021/jacs.3c01500
Masullo, L.A., Steiner, F., Zähringer, J., Lopez, L.F., Bohlen, J., Richter, L., Cole, F., Tinnefeld, P., Stefani, F.D., 2021. Pulsed Interleaved MINFLUX. Nano Lett. 21, 840–846. https://doi.org/10.1021/acs.nanolett.0c04600
Mazal, H., Wieser, F.-F., Bollschweiler, D., Sandoghdar, V., 2025a. Cryogenic light microscopy of vitrified samples with Ångstrom precision. https://doi.org/10.1101/2025.05.27.656160
Mazal, H., Wieser, F.-F., Bollschweiler, D., Sandoghdar, V., 2025b. Cryogenic light microscopy of vitrified samples with Ångstrom precision. https://doi.org/10.1101/2025.05.27.656160
Mazal, H., Wieser, F.-F., Sandoghdar, V., 2022. Deciphering a hexameric protein complex with Angstrom optical resolution. eLife 11, e76308. https://doi.org/10.7554/eLife.76308
McCafferty, C.L., Klumpe, S., Amaro, R.E., Kukulski, W., Collinson, L., Engel, B.D., 2024. Integrating cellular electron microscopy with multimodal data to explore biology across space and time. Cell 187, 563–584. https://doi.org/10.1016/j.cell.2024.01.005
McEvoy, A.L., Hoi, H., Bates, M., Platonova, E., Cranfill, P.J., Baird, M.A., Davidson, M.W., Ewers, H., Liphardt, J., Campbell, R.E., 2012. mMaple: A Photoconvertible Fluorescent Protein for Use in Multiple Imaging Modalities. PLOS ONE 7, e51314. https://doi.org/10.1371/journal.pone.0051314
Moebel, E., Martinez-Sanchez, A., Lamm, L., Righetto, R.D., Wietrzynski, W., Albert, S., Larivière, D., Fourmentin, E., Pfeffer, S., Ortiz, J., Baumeister, W., Peng, T., Engel, B.D., Kervrann, C., 2021. Deep learning improves macromolecule identification in 3D cellular cryo-electron tomograms. Nat. Methods 18, 1386–1394. https://doi.org/10.1038/s41592-021-01275-4
Moerner, W.E., Orrit, M., 1999. Illuminating Single Molecules in Condensed Matter. Science 283, 1670–1676. https://doi.org/10.1126/science.283.5408.1670

Mojiri, S., Dobbs, J.M., Faul, N., Burg, T.P., Mahamid, J., Ries, J., 2025. Effects of base temperature, immersion medium, and EM grid material on devitrification thresholds in cryogenic optical super-resolution microscopy. J. Struct. Biol. 217, 108231. https://doi.org/10.1016/j.jsb.2025.108231

Mortensen, K.I., Churchman, L.S., Spudich, J.A., Flyvbjerg, H., 2010. Optimized localization analysis for single-molecule tracking and super-resolution microscopy. Nat. Methods 7, 377–381. https://doi.org/10.1038/nmeth.1447

Moser, F., Pražák, V., Mordhorst, V., Andrade, D.M., Baker, L.A., Hagen, C., Grünewald, K., Kaufmann, R., 2019. Cryo-SOFI enabling low-dose super-resolution correlative light and electron cryo-microscopy. Proc. Natl. Acad. Sci. 116, 4804–4809. https://doi.org/10.1073/pnas.1810690116

Mulhall, E.M., Gharpure, A., Lee, R.M., Dubin, A.E., Aaron, J.S., Marshall, K.L., Spencer, K.R., Reiche, M.A., Henderson, S.C., Chew, T.-L., Patapoutian, A., 2023. Direct observation of the conformational states of PIEZO1. Nature 620, 1117–1125. https://doi.org/10.1038/s41586-023-06427-4

Mund, M., Tschanz, A., Wu, Y.-L., Frey, F., Mehl, J.L., Kaksonen, M., Avinoam, O., Schwarz, U.S., Ries, J., 2023. Clathrin coats partially preassemble and subsequently bend during endocytosis. J. Cell Biol. 222, e202206038. https://doi.org/10.1083/jcb.202206038

Nahmani, M., Lanahan, C., DeRosier, D., Turrigiano, G.G., 2017. High-numerical-aperture cryogenic light microscopy for increased precision of superresolution reconstructions. Proc. Natl. Acad. Sci. 114, 3832–3836. https://doi.org/10.1073/pnas.1618206114

Nieuwenhuizen, R.P.J., Lidke, K.A., Bates, M., Puig, D.L., Grünwald, D., Stallinga, S., Rieger, B., 2013. Measuring image resolution in optical nanoscopy. Nat. Methods 10, 557–562. https://doi.org/10.1038/nmeth.2448

Patterson, G.H., Lippincott-Schwartz, J., 2002. A Photoactivatable GFP for Selective Photolabeling of Proteins and Cells. Science 297, 1873–1877. https://doi.org/10.1126/science.1074952

Perez, D., Dahlberg, P.D., Wang, J., Sartor, A.M., Borden, J.S., Shapiro, L., Moerner, W.E., 2022. Identification and demonstration of roGFP2 as an environmental sensor for cryogenic correlative light and electron microscopy. J. Struct. Biol. 214, 107881. https://doi.org/10.1016/j.jsb.2022.107881

Perez, D., Dowlatshahi, D.P., Azaldegui, C.A., Ansell, T.B., Dahlberg, P.D., Moerner, W.E., 2024. Exploring Transient States of PAmKate to Enable Improved Cryogenic Single-Molecule Imaging. J. Am. Chem. Soc. https://doi.org/10.1021/jacs.4c05632

Phillips, M.A., Harkiolaki, M., Pinto, D.M.S., Parton, R.M., Palanca, A., Garcia-Moreno, M., Kounatidis, I., Sedat, J.W., Stuart, D.I., Castello, A., Booth, M.J., Davis, I., Dobbie, I.M., 2020. CryoSIM: super-resolution 3D structured illumination cryogenic fluorescence microscopy for correlated ultrastructural imaging. Optica 7, 802–812. https://doi.org/10.1364/OPTICA.393203

Pleiner, T., Bates, M., Trakhanov, S., Lee, C.-T., Schliep, J.E., Chug, H., Böhning, M., Stark, H., Urlaub, H., Görlich, D., 2015. Nanobodies: site-specific labeling for super-resolution imaging, rapid epitope-mapping and native protein complex isolation. eLife 4, e11349. https://doi.org/10.7554/eLife.11349

Power, R.M., Tschanz, A., Zimmermann, T., Ries, J., 2024. Build and operation of a custom 3D, multicolor, single-molecule localization microscope. Nat. Protoc. 1–59. https://doi.org/10.1038/s41596-024-00989-x

Prakash, K., Curd, A.P., 2023. Assessment of 3D MINFLUX data for quantitative structural biology in cells. Nat. Methods 20, 48–51. https://doi.org/10.1038/s41592-022-01694-x

Radmacher, N., Chizhik, A.I., Nevskyi, O., Gallea, J.I., Gregor, I., Enderlein, J., 2025. Molecular Level Super-Resolution Fluorescence Imaging. https://doi.org/10.1146/annurev-biophys-071524-105321

Reinhardt, S.C.M., Masullo, L.A., Baudrexel, I., Steen, P.R., Kowalewski, R., Eklund, A.S., Strauss, S., Unterauer, E.M., Schlichthaerle, T., Strauss, M.T., Klein, C., Jungmann, R., 2023. Ångström-resolution fluorescence microscopy. Nature 617, 711–716. https://doi.org/10.1038/s41586-023-05925-9

Reymond, L., Ziegler, J., Knapp, C., Wang, F.-C., Huser, T., Ruprecht, V., Wieser, S., 2019. SIMPLE: Structured illumination based point localization estimator with enhanced precision. Opt. Express 27, 24578–24590. https://doi.org/10.1364/OE.27.024578

Rice, G., Wagner, T., Stabrin, M., Sitsel, O., Prumbaum, D., Raunser, S., 2023. TomoTwin: generalized 3D localization of macromolecules in cryo-electron tomograms with structural data mining. Nat. Methods 20, 871–880. https://doi.org/10.1038/s41592-023-01878-z

Rice, W.J., Cheng, A., Noble, A.J., Eng, E.T., Kim, L.Y., Carragher, B., Potter, C.S., 2018. Routine determination of ice thickness for cryo-EM grids. J. Struct. Biol. 204, 38–44. https://doi.org/10.1016/j.jsb.2018.06.007

Rickgauer, J.P., Grigorieff, N., Denk, W., 2017. Single-protein detection in crowded molecular environments in cryo-EM images. eLife 6, e25648. https://doi.org/10.7554/eLife.25648

Rimoli, C.V., Valades-Cruz, C.A., Curcio, V., Mavrakis, M., Brasselet, S., 2022. 4polar-STORM polarized super-resolution imaging of actin filament organization in cells. Nat. Commun. 13, 301. https://doi.org/10.1038/s41467-022-27966-w

Rust, M.J., Bates, M., Zhuang, X., 2006. Sub-diffraction-limit imaging by stochastic optical reconstruction microscopy (STORM). Nat. Methods 3, 793–796. https://doi.org/10.1038/nmeth929

Sabinina, V.J., Hossain, M.J., Hériché, J.-K., Hoess, P., Nijmeijer, B., Mosalaganti, S., Kueblbeck, M., Callegari, A., Szymborska, A., Beck, M., Ries, J., Ellenberg, J., 2021. Three-dimensional superresolution fluorescence microscopy maps the variable molecular architecture of the nuclear pore complex. Mol. Biol. Cell 32, 1523–1533. https://doi.org/10.1091/mbc.E20-11-0728

Sau, A., Schnorrenberg, S., Huang, Z., Bandyopadhyay, D., Sharma, A., Gürth, C.-M., Dave, S., Musser, S.M., 2025. Overlapping nuclear import and export paths unveiled by two-colour MINFLUX. Nature 1–7. https://doi.org/10.1038/s41586-025-08738-0

Scheiderer, L., von der Emde, H., Hesselink, M., Weber, M., Hell, S.W., 2024a. MINSTED tracking of single biomolecules. Nat. Methods 1–5. https://doi.org/10.1038/s41592-024-02209-6

Scheiderer, L., Wirth, J.O., Tarnawski, M., Hell, S.W., 2024b. Dual-color MINFLUX: Kinesin-1 takes Chassé-Inchworm steps. https://doi.org/10.1101/2024.03.05.583551

Scher, N., Rechav, K., Paul-Gilloteaux, P., Avinoam, O., 2021. In situ fiducial markers for 3D correlative cryo-fluorescence and FIB-SEM imaging. iScience 24, 102714. https://doi.org/10.1016/j.isci.2021.102714

Schmidt, R., Weihs, T., Wurm, C.A., Jansen, I., Rehman, J., Sahl, S.J., Hell, S.W., 2021. MINFLUX nanometer-scale 3D imaging and microsecond-range tracking on a common

fluorescence microscope. Nat. Commun. 12, 1478. https://doi.org/10.1038/s41467-021-21652-z

Schnitzbauer, J., Strauss, M.T., Schlichthaerle, T., Schueder, F., Jungmann, R., 2017. Super-resolution microscopy with DNA-PAINT. Nat. Protoc. 12, 1198–1228. https://doi.org/10.1038/nprot.2017.024

Schueder, F., Rivera-Molina, F., Su, M., Marin, Z., Kidd, P., Rothman, J.E., Toomre, D., Bewersdorf, J., 2024. Unraveling cellular complexity with transient adapters in highly multiplexed super-resolution imaging. Cell 187, 1769-1784.e18. https://doi.org/10.1016/j.cell.2024.02.033

Sharonov, A., Hochstrasser, R.M., 2006. Wide-field subdiffraction imaging by accumulated binding of diffusing probes. Proc. Natl. Acad. Sci. 103, 18911–18916. https://doi.org/10.1073/pnas.0609643104

Sica, A.V., Zaoralová, M., Antolini, C., Boltje, D.B., Penzes, J.J., Malmqvist, L.M., Jensen, G., Kaelber, J.T., Dahlberg, P., 2024. Optical Interference for the Guidance of Cryogenic Focused Ion Beam Milling Beyond the Axial Diffraction Limit. https://doi.org/10.1101/2024.11.01.621231

Silvester, E., Vollmer, B., Pražák, V., Vasishtan, D., Machala, E.A., Whittle, C., Black, S., Bath, J., Turberfield, A.J., Grünewald, K., Baker, L.A., 2021. DNA origami signposts for identifying proteins on cell membranes by electron cryotomography. Cell 184, 1110-1121.e16. https://doi.org/10.1016/j.cell.2021.01.033

Štefko, M., Ottino, B., Douglass, K.M., Manley, S., 2018. Autonomous illumination control for localization microscopy. Opt. Express 26, 30882–30900. https://doi.org/10.1364/OE.26.030882

Steinhauer, C., Jungmann, R., Sobey, T.L., Simmel, F.C., Tinnefeld, P., 2009. DNA Origami as a Nanoscopic Ruler for Super-Resolution Microscopy. Angew. Chem. Int. Ed. 48, 8870–8873. https://doi.org/10.1002/anie.200903308

Subach, F.V., Patterson, G.H., Manley, S., Gillette, J.M., Lippincott-Schwartz, J., Verkhusha, V.V., 2009. Photoactivatable mCherry for high-resolution two-color fluorescence microscopy. Nat. Methods 6, 153–159. https://doi.org/10.1038/nmeth.1298

Tegunov, D., Xue, L., Dienemann, C., Cramer, P., Mahamid, J., 2021. Multi-particle cryo-EM refinement with M visualizes ribosome-antibiotic complex at 3.5 Å in cells. Nat. Methods 18, 186–193. https://doi.org/10.1038/s41592-020-01054-7

Thevathasan, J.V., Kahnwald, M., Cieśliński, K., Hoess, P., Peneti, S.K., Reitberger, M., Heid, D., Kasuba, K.C., Hoerner, S.J., Li, Y., Wu, Y.-L., Mund, M., Matti, U., Pereira, P.M., Henriques, R., Nijmeijer, B., Kueblbeck, M., Sabinina, V.J., Ellenberg, J., Ries, J., 2019. Nuclear pores as versatile reference standards for quantitative superresolution microscopy. Nat. Methods 16, 1045–1053. https://doi.org/10.1038/s41592-019-0574-9

Toro-Nahuelpan, M., Zagoriy, I., Senger, F., Blanchoin, L., Théry, M., Mahamid, J., 2020. Tailoring cryo-electron microscopy grids by photo-micropatterning for in-cell structural studies. Nat. Methods 17, 50–54. https://doi.org/10.1038/s41592-019-0630-5

Tuijtel, M.W., Koster, A.J., Jakobs, S., Faas, F.G.A., Sharp, T.H., 2019. Correlative cryo super-resolution light and electron microscopy on mammalian cells using fluorescent proteins. Sci. Rep. 9, 1369. https://doi.org/10.1038/s41598-018-37728-8

Unterauer, E.M., Shetab Boushehri, S., Jevdokimenko, K., Masullo, L.A., Ganji, M., Sograte-Idrissi, S., Kowalewski, R., Strauss, S., Reinhardt, S.C.M., Perovic, A., Marr, C., Opazo,

F., Fornasiero, E.F., Jungmann, R., 2024. Spatial proteomics in neurons at single-protein resolution. Cell 187, 1785-1800.e16. https://doi.org/10.1016/j.cell.2024.02.045

van de Linde, S., Löschberger, A., Klein, T., Heidbreder, M., Wolter, S., Heilemann, M., Sauer, M., 2011. Direct stochastic optical reconstruction microscopy with standard fluorescent probes. Nat. Protoc. 6, 991–1009. https://doi.org/10.1038/nprot.2011.336

van den Dries, K., Fransen, J., Cambi, A., 2022. Fluorescence CLEM in biology: historic developments and current super-resolution applications. FEBS Lett. 596, 2486–2496. https://doi.org/10.1002/1873-3468.14421

Vorlaufer, J., Semenov, N., Kreuzinger, C., Javoor, M.G., Zens, B., Dueñas, N.A., Tavakoli, M.R., Šuplata, M., Jahr, W., Lyudchik, J., Wartak, A., Schur, F.K.M., Danzl, J.G., 2025. Image-based 3D active sample stabilization on the nanometer scale for optical microscopy. Biophys. Rep. 5. https://doi.org/10.1016/j.bpr.2025.100211

Wang, L., Bateman, B., Zanetti-Domingues, L.C., Moores, A.N., Astbury, S., Spindloe, C., Darrow, M.C., Romano, M., Needham, S.R., Beis, K., Rolfe, D.J., Clarke, D.T., Martin-Fernandez, M.L., 2019. Solid immersion microscopy images cells under cryogenic conditions with 12 nm resolution. Commun. Biol. 2, 1–11. https://doi.org/10.1038/s42003-019-0317-6

Wang, Q., Mercogliano, C.P., Löwe, J., 2011. A Ferritin-Based Label for Cellular Electron Cryotomography. Structure 19, 147–154. https://doi.org/10.1016/j.str.2010.12.002

Wang, W., Jakobi, A., Wu, Y.-L., Ries, J., Stallinga, S., Rieger, B., 2023. Particle fusion of super-resolution data reveals the unit structure of Nup96 in Nuclear Pore Complex. Sci. Rep. 13, 13327. https://doi.org/10.1038/s41598-023-39829-5

Weber, M., Leutenegger, M., Stoldt, S., Jakobs, S., Mihaila, T.S., Butkevich, A.N., Hell, S.W., 2021. MINSTED fluorescence localization and nanoscopy. Nat. Photonics 15, 361–366. https://doi.org/10.1038/s41566-021-00774-2

Weber, M., von der Emde, H., Leutenegger, M., Gunkel, P., Sambandan, S., Khan, T.A., Keller-Findeisen, J., Cordes, V.C., Hell, S.W., 2022. MINSTED nanoscopy enters the Ångström localization range. Nat. Biotechnol. 1–8. https://doi.org/10.1038/s41587-022-01519-4

Weisenburger, S., Boening, D., Schomburg, B., Giller, K., Becker, S., Griesinger, C., Sandoghdar, V., 2017. Cryogenic optical localization provides 3D protein structure data with Angstrom resolution. Nat. Methods 14, 141–144. https://doi.org/10.1038/nmeth.4141

Weisenburger, S., Jing, B., Hänni, D., Reymond, L., Schuler, B., Renn, A., Sandoghdar, V., 2014. Cryogenic Colocalization Microscopy for Nanometer-Distance Measurements. ChemPhysChem 15, 763–770. https://doi.org/10.1002/cphc.201301080

Wolff, J.O., Scheiderer, L., Engelhardt, T., Engelhardt, J., Matthias, J., Hell, S.W., 2023. MINFLUX dissects the unimpeded walking of kinesin-1. Science 379, 1004–1010. https://doi.org/10.1126/science.ade2650

Wu, G.-H., Mitchell, P.G., Galaz-Montoya, J.G., Hecksel, C.W., Sontag, E.M., Gangadharan, V., Marshman, J., Mankus, D., Bisher, M.E., Lytton-Jean, A.K.R., Frydman, J., Czymmek, K., Chiu, W., 2020. Multi-scale 3D Cryo-Correlative Microscopy for Vitrified Cells. Structure 28, 1231-1237.e3. https://doi.org/10.1016/j.str.2020.07.017

Wu, T., Lu, J., Lew, M.D., 2022. Dipole-spread-function engineering for simultaneously measuring the 3D orientations and 3D positions of fluorescent molecules. Optica 9, 505. https://doi.org/10.1364/OPTICA.451899

Yang, Y., Fan, S., Webb, J.A., Ma, Y., Goyette, J., Chen, X., Gaus, K., Tilley, R.D., Gooding, J.J., 2023. Electrochemical fluorescence switching of enhanced green fluorescent protein. Biosens. Bioelectron. 237, 115467. https://doi.org/10.1016/j.bios.2023.115467

Yang, Y., Ma, Y., Berengut, J.F., Lee, L.K., Tilley, R.D., Gaus, K., Gooding, J.J., 2024. Electrochemically controlled blinking of fluorophores for quantitative STORM imaging. Nat. Photonics 1–8. https://doi.org/10.1038/s41566-024-01431-0

Young, L.N., Villa, E., 2023. Bringing Structure to Cell Biology with Cryo-Electron Tomography. Annu. Rev. Biophys. 52, 573–595. https://doi.org/10.1146/annurev-biophys-111622-091327

Zähringer, J., Cole, F., Bohlen, J., Steiner, F., Kamińska, I., Tinnefeld, P., 2023. Combining pMINFLUX, graphene energy transfer and DNA-PAINT for nanometer precise 3D super-resolution microscopy. Light Sci. Appl. 12, 70. https://doi.org/10.1038/s41377-023-01111-8

Zhang, O., Guo, Z., He, Y., Wu, T., Vahey, M.D., Lew, M.D., 2023. Six-dimensional single-molecule imaging with isotropic resolution using a multi-view reflector microscope. Nat. Photonics 17, 179–186. https://doi.org/10.1038/s41566-022-01116-6

A. Publication “Image-based 3D active sample stabilization on the nanometer scale for optical microscopy”

The following article is reprinted from (Vorlaufer et al., 2025) under CC BY license. Formatting was harmonized to the style of this document without modifying the content. Supporting material comprises 5 figures and can be retrieved from the online version of the article (https://doi.org/10.1016/j.bpr.2025.100211).

A.1 Abstract

Super-resolution microscopy often entails long acquisition times of minutes to hours. Since drifts during the acquisition adversely affect data quality, active sample stabilization is commonly used for some of these techniques to reach their full potential. Although drifts in the lateral plane can often be corrected after acquisition, this is not always possible or may come with drawbacks. Therefore, it is appealing to stabilize sample position in three dimensions (3D) during acquisition. Various schemes for active sample stabilization have been demonstrated previously, with some reaching sub-nanometer stability in 3D. Here, we present a scheme for active drift correction that delivers the nanometer-scale 3D stability demanded by state-of-the-art super-resolution techniques and is straightforward to implement compared to previous schemes capable of reaching this level of stabilization precision. Using a refined algorithm that can handle various types of reference structure, without sparse signal peaks being mandatory, we stabilized sample position to ∼1 nm in 3D using objective lenses both with high and low numerical aperture. Our implementation requires only the addition of a simple widefield imaging path and we provide an open-source control software with graphical user interface to facilitate easy adoption of the module. Finally, we demonstrate how this has the potential to enhance data collection for diffraction-limited and super-resolution imaging techniques using single-molecule localization microscopy and cryo-confocal imaging as showcases.

A.2 Why it matters

Super-resolution light microscopy has enabled the visualization of biological structures down to the nanometer scale. However, uncorrected drifts during often extended acquisition times may adversely affect data quality. Active drift correction in three dimensions has achieved sub-nanometer stabilization, but state-of-the-art techniques come with overheads on sample preparation and/or hardware. Here, we demonstrate an image-based stabilization scheme that allows for flexibility regarding structures used for stabilization and is straightforward to adopt. Using a simple implementation, we stabilized the sample position to around 1 nm over extended acquisition times and demonstrated usefulness in two example imaging settings where sample drifts are critical: super-resolution (single-molecule localization) microscopy and confocal imaging at cryogenic temperatures.

A.3 Introduction

Fluorescence imaging is a powerful technique to reveal biological information, with super-resolution approaches (1,2) routinely allowing for the investigation of length scales down to few tens of nanometers. However, uncorrected motion of the sample during acquisition adversely affects data quality both in conventional and in super-resolution microscopy. This issue is typically aggravated for super-resolution approaches due to the higher spatial resolution and extended acquisition times.

Depending on the modality of image formation, drifts affect different super-resolution techniques in distinct ways. In single-molecule localization microscopy (SMLM) (3), emitters are activated in a spatially stochastic manner and individually localized. Therefore, uncorrected sample movements corrupt information about the relative positions of localized fluorophores, effectively decreasing the resolution of a reconstructed dataset. Since axial drifts directly hamper the localization by defocusing the signal from single emitters, focus-stabilization systems are common components of state-of-the-art SMLM setups (3,4). Compared to axial drifts, lateral drifts can be more readily corrected after acquisition, for example using redundant cross-correlation (RCC) (5) or fiducial markers (6,7,8). However, this approach becomes more elaborate when applications require high accuracy. For example, to achieve sub-nanometer resolution in advanced variants of SMLM, a combination of RCC- and fiducial-based drift correction followed by local refinement was required (9,10). It is attractive to actively stabilize the sample position (i.e., measure and compensate drifts during acquisition) in three dimensions (3D) during an acquisition, as this generates a markedly improved starting point for any downstream corrections. Moreover, active 3D stabilization allows for the observation of how the reconstructed structure builds up in real time, avoids regions of interest (ROIs) drifting out of the field of view, and eliminates blurring of the point spread function (PSF) by drifts occurring within individual camera frames.

Recently, the minimal photon fluxes (MINFLUX) (11) and minimal STED (MINSTED) (12) concepts have achieved imaging and tracking at (sub-)nanometer localization precision by combining coordinate-stochastic activation of fluorophores with coordinate-targeted readout of their spatial coordinates. These concepts crucially depend on accurately positioning light patterns with respect to fluorophore positions. Since relative drifts between fluorophore coordinates and positions of light pattern cannot be readily measured or corrected, it is essential to actively stabilize sample position in 3D during acquisition in such modalities. Under optimal imaging conditions, the precision of sample stabilization can indeed become limiting for the achievable resolution (13).

Sample motion during imaging has much broader implications, reaching beyond SMLM and nanometer-scale imaging. For diffraction-limited and super-resolution imaging realized on point-scanning microscopy platforms, including, e.g., typical implementations of stimulated emission depletion super-resolution microscopy (14,15), drifts skew the resulting image in an unpredictable manner. Since these distortions cannot be corrected after an acquisition, drifts are problematic for accurately extracting the relationship between coordinates queried at different time points. Depending on the magnitude and timescale of drifts, they may either interfere with visualization of individual (sub-diffraction) structures or lead to larger-scale distortions that may, e.g., compromise correlation to other imaging modalities, such as electron microscopy (16).

Imaging at cryogenic temperatures offers the possibility to directly analyze structures preserved in a near-native state by rapid freezing avoiding formation of crystalline ice ("vitrification"), without the need for chemical fixation. Here, the temperature of the sample needs to be kept below ~135 K to avoid devitrification. In this imaging setting, prominent mechanical drifts may occur due to limited mechanical stability of commonly used cryo-stages, which may impact the performance of both diffraction-limited approaches, in particular point scanning, as well as super-resolution imaging (17). In addition to the development of highly stable cryo-stages for optical imaging, there is an opportunity to increase imaging performance and correlation accuracy with potent stabilization techniques.

Image-based active drift correction requires the structures that are used for the measurement of sample position to be in highly stable spatial relation with the structures of interest in the (biological) sample. Schemes capable of stabilizing sample position to (sub-)nanometer levels in 3D typically utilize sparse signal peaks from external fiducial markers added to the sample (18,19,20,21,22,23). Adding fiducials entails an extra step in the sample preparation that might be undesirable for certain preparations or require careful optimization. Fiducial beads may show bleaching, intensity fluctuations, or aggregation (6), as well as movements on the nanometer scale relative to the structures of interest (8). This prompted, e.g., the development of DNA origamis specifically tailored to point accumulation for imaging in nanoscale topography (PAINT)-imaging, featuring integrated binding sites for single fluorophores used as markers for drift correction (24). Fiducials in the same spectral channel(s) as the biological structures of interest may decrease usable field of view or cause out-of-focus background. Taken together, it would be desirable to have flexible options for stabilizing either on structures directly present in the biological specimen itself or another reference structure in highly stable relation to the sample. Implementations using biological structures for stabilization have been limited by the low contrast of brightfield imaging (25), although Shang et al. (26) recently achieved 3- to 6-nm stabilization precision using differential phase contrast imaging. Overall, currently available schemes that realize nanoscale active stabilization in 3D add a substantial amount of complexity to the hardware and/or sample preparation process.

Here, we describe a scheme for active stabilization of sample position capable of reaching nanoscale precision in 3D with moderate overhead to the microscope hardware and sample preparation. Our approach reaches sub-nanometer 3D stabilization precision with an image-based approach and is applicable to a diverse set of reference structures (e.g., scattering beads, structured sample supports), where sparse signal peaks, as typically provided by fiducial beads, are not mandatory. It reaches such high performance also in imaging settings where an objective lens with a comparatively low numerical aperture (NA; in our case 0.75) is used. This combination of nanoscale stability with flexibility regarding sample preparation and NA promises to be an enabling feature for various techniques for which active stabilization is currently challenging. We achieved this performance by combining cross-correlation for determining lateral displacements with estimation of axial displacements through analysis of pixel intensity distributions, in both cases comparing measurement image frames to reference stacks along the respective directions acquired directly before experiments. We show the usefulness of our scheme by applying it in two example imaging settings: SMLM of the nuclear pore complex and cryo-confocal imaging of fluorescent beads. Our concept is straightforward to implement (Fig. 1 *A*), and we provide an open-source software package including a graphical user interface to enable other researchers to adopt our method easily.

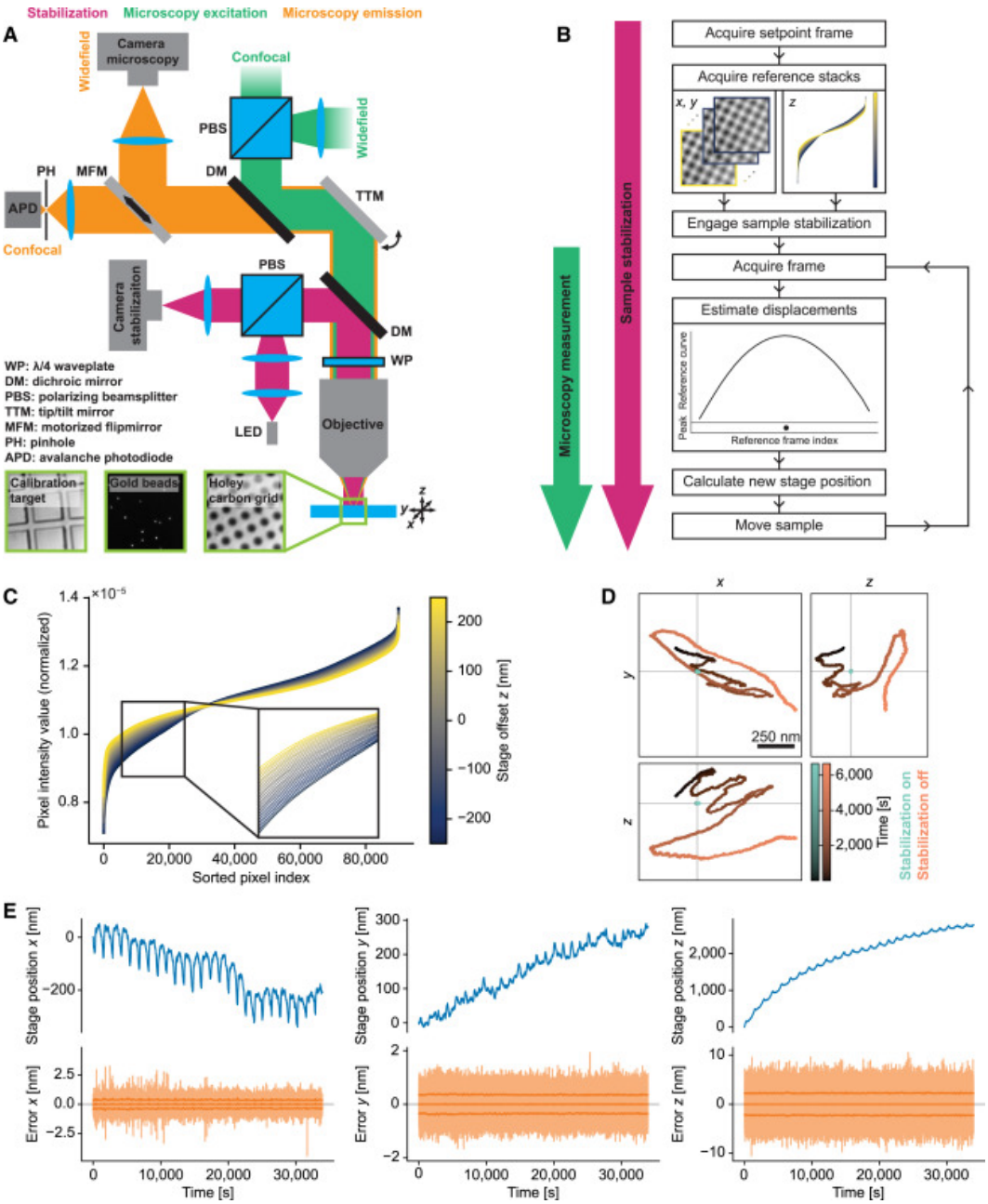

Figure A.1: Active stabilization concept. (A) Schematics of optical path for sample stabilization (magenta), comprising a widefield imaging path using near-infrared light, combined with the microscopy path (green/orange) via a dichroic mirror (DM). For further details, see Fig. S1. Bottom: representative raw images of different structures used for stabilization. Right: holey carbon film commonly used in cryo-fluorescence imaging and electron microscopy. Middle: gold beads immobilized on a coverslip. Left: magnification calibration target with 10-µm tiles. Individual images have approximately 23-µm edge length. (B) Stabilization workflow. After choosing an ROI and acquisition of reference stacks (data shown correspond to one of the datasets used in Fig. 2B), the scheme estimates displacements in each iteration of the active feedback loop by comparing camera frames against the reference stacks and actuates on sample position. Microscopy measurements are started once feedback is engaged (indicated by arrows left of the workflow diagram). (C) Normalized pixel intensity as a function of intensity-sorted pixel index for each frame (color coded) of the reference stack along the z direction. Enlarged view of the data in (B). Curves for the individual frames of the reference stack (spaced 20 nm along z) can be discerned as separate lines in the magnified view. (D) Position of an individual gold bead on a coverslip over time with and without sample stabilization, tracked in the microscopy path for 1 h 51 min. For stabilization of sample position, a distinct set of gold beads on the same coverslip was used in the stabilization path. (E) Long-term stabilization measurement on a holey carbon film. The blue curves show the stage movement applied to

compensate drifts. Error signals reflecting the residual deviations from the setpoint sample position (semi-transparent orange curves) are centered on 0. The central solid orange line shows the rolling average of the error signals across 1000 data points. The lines above and below represent the standard deviation across the same window. The prominent periodic stage movements are correlated with fluctuations of laboratory temperature.

A.4 Materials and methods

A.4.1 Microscope setup

We performed all measurements on a homebuilt setup comprising separate paths for active sample stabilization and for microscopy measurements (widefield and confocal). See Fig. S1 for a schematic of the beam path as well as a list of the components used. The hardware was controlled by a standard microscope-control PC equipped with an Intel Core i7 CPU (8 × 3.6 GHz) and 64 GB RAM.

The setup was constructed in an upright configuration to facilitate compatibility with a commercial cryo-stage (CMS196 V3, Linkam Scientific Instruments, Redhill, United Kingdom). The sample stage was mounted on a calibrated 3D piezo stage, which was used for drift correction. Light was collected by the same objective as was used for illumination. Depending on the application, we used either an oil-immersion objective (100×/NA 1.45, Olympus) or a long working distance air objective (100×/NA 0.75, Leica). We used a Leica tube lens for all measurements, as this also provided adequate performance when using the Olympus oil-immersion objective.

The common beam path shared by the stabilization and the other imaging modalities comprised an achromatic $\lambda/4$ waveplate placed near the objective lens to create circularly polarized light at the sample, as well as a telescope consisting of the tube lens and an achromatic doublet lens. A shortpass dichroic mirror (DM) separated the path used for sample stabilization (operated at near-infrared wavelength) from the main part of the microscope (microscopy excitation and emission paths in Fig. 1 *A*).

A.4.1.1 Sample stabilization path

Light from a fiber-coupled LED emitting around 940 nm was collimated and spectrally filtered. We chose this spectral window because it is not commonly used in fluorescence imaging. The vertical polarization component was reflected by a polarizing beam splitter (PBS) and directed to the common optical path described above while the horizontal polarization was dumped. The light reflected by the sample had an orthogonal polarization after passing the $\lambda/4$ waveplate near the objective lens in both directions and was hence transmitted by the PBS. A longpass filter blocked residual light from the microscopy path before the light was focused on a camera. By default, we used a temperature-stabilized charge-coupled device (CCD) camera at 10-ms exposure time. However, we also confirmed that the concept worked equally well, in fact with even better performance (evaluated by the magnitude of residual estimated displacements (error signal)), using an industry-grade complementary metal oxide semiconductor (CMOS) camera (Figs. 1 *D* and S2) after allowing enough time for the camera temperature to equilibrate after starting continuous frame acquisition. Without this warm-up phase, which typically lasted for several hours depending on the heatsink attached to the camera (Fig. S2), pixel intensity values increased gradually during acquisition of reference stacks and active stabilization, which led to nonoptimal performance despite intensity normalization.

The image pixel size of the employed CCD camera was 75 nm/78 nm along *x*/*y* directions for the air objective, and 67 nm/70 nm for the oil-immersion objective, as measured with a

calibration target with 10-μm tile pattern (Planotec S1934, FIAS, Biedermannsdorf, Austria). Note that objective lenses were not fully corrected for the near-infrared range. For the CMOS camera, we measured pixel sizes of 55 nm/52 nm for the air objective and 50 nm/50 nm for the oil objective (again *x*/*y*), which is in line with the difference of the specified pixel sizes of the cameras. The field of view was limited by the aperture of the focusing lens in front of the camera, corresponding to a diameter of 56 μm in the sample plane. For the stabilization measurements, we read out an ROI of 300 × 300 pixels. The LED illumination delivered a maximum optical power of ~280 μW at the sample position. We adjusted the intensity for every measurement, such that the maximum pixel intensity value was around 60%–80% of the saturation level of the camera.

A.4.1.2 Microscopy path

For the microscopy applications tested here, we used either widefield or confocal fluorescence imaging. Laser beams at two different wavelengths (488 and 642 nm) were combined via DMs and coupled into one of two polarization-maintaining optical fibers for widefield and confocal illumination, depending on the position of a motorized flip mirror.

For confocal imaging, polarization direction at the output of the fiber was chosen horizontal, and light was collimated and transmitted through a PBS. The light was then reflected by a multi-band DM and passed a tip/tilt piezo mirror, which was situated in a plane conjugate to the objective's back focal plane to scan the beam across the sample. The fluorescence was collected by the same path, transmitted through the multi-pass DM and focused on a pinhole. After spectral filtering, it was detected by an avalanche photo-diode operated in single-photon counting mode. Confocal measurements were performed using home-written software for microscope control.

Light for widefield imaging exited the respective fiber with vertical polarization. It was combined with the confocal imaging path by reflecting it from the PBS that transmitted the light for confocal imaging. In the widefield illumination path, a lens before the PBS focused the light at the back focal plane of the objective lens. For widefield imaging, a motorized flip mirror after the multi-pass DM guided the emitted light to a scientific CMOS (sCMOS) camera. For evaluating the out-of-loop stability in 3D, i.e., the positional stability of sample features measured with structures and an optical path distinct from those used in the sample stabilization, we induced astigmatism by placing a pair of cylindrical lenses with f = ± 1 m rotated against each other before the camera, as described by Power et al. (4). Without the added astigmatism, images had a pixel size of 53 nm for the oil objective (using 642 nm light) and 60 nm for the air objective (using 488-nm light).

A.4.2 Stabilization workflow

Our stabilization unit was controlled by a custom graphical user interface (GUI) written in Python. The GUI controlled servo motors and a piezo stage for coarse and fine adjustment of sample position, respectively, as well as the camera. The software allowed for setting and saving of all stabilization parameters. Options for saving the raw image, stage position, and error signals (i.e., estimated displacement of measured position from setpoint) for every iteration of the feedback loop were also included. Plots showing the stage position and error signal for a given axis in real time facilitated straightforward assessment of the stabilization performance. Computer code for sample stabilization is part of this submission and is available via GitHub (see data and code availability statement).

After defining ROI and stabilization parameters, the sample stabilization was engaged. First, we saved a camera frame as the setpoint of the stabilization ("setpoint frame"). Subsequently, a reference stack was acquired for every axis by moving the stage over a user-defined range (symmetrical with respect to the starting position of the stage) and step size. After every step, we allowed the stage to settle, including an additional 100-ms buffer time, and added the latest camera frame to the respective reference stack. Normalizing the frames in terms of intensity turned out to be critical for adequate performance. We achieved this by dividing each pixel intensity value by the sum across all pixels.

After the acquisition of the reference stacks, the stage was moved back to the starting position and the actual drift compensation started. The feedback mechanism iteratively estimated the amount the sample had moved since the beginning of the measurement and actuated the sample piezo stage to compensate for these displacements. Drifts during the acquisition of reference stacks or potential systematic biases of the displacement estimation may result in constant offsets of the calculated displacements. Directly using these displacements may therefore hold the sample at a constant position that is slightly offset from the user-defined setpoint. To avoid this, our error signals were defined as the displacements with respect to the setpoint frame acquired before the reference stacks (instead of the center of the reference stacks). The algorithm used for continuous drift correction is described in the results section and laid out as pseudocode below.

For fine calibration of error signal amplitude in physical length units (nanometer), we acquired calibration measurements after every stabilization measurement shown in Fig. 2 by switching off the feedback and recording the error signals as we stepped the stage back and forth by 20 nm along the respective axis. This procedure was repeated for all axes. Due to drifts occurring during these calibration measurements, we found that it was convenient to find the calibration factors by manually tuning them. When using Gaussian fitting for displacement estimation, we typically found best correspondence between step size of the stage and error signal amplitude with scaling factors between 0.85 and 1.1. We estimate that our calibrations and hence values of the error signals stated in this publication were accurate within a few percent.

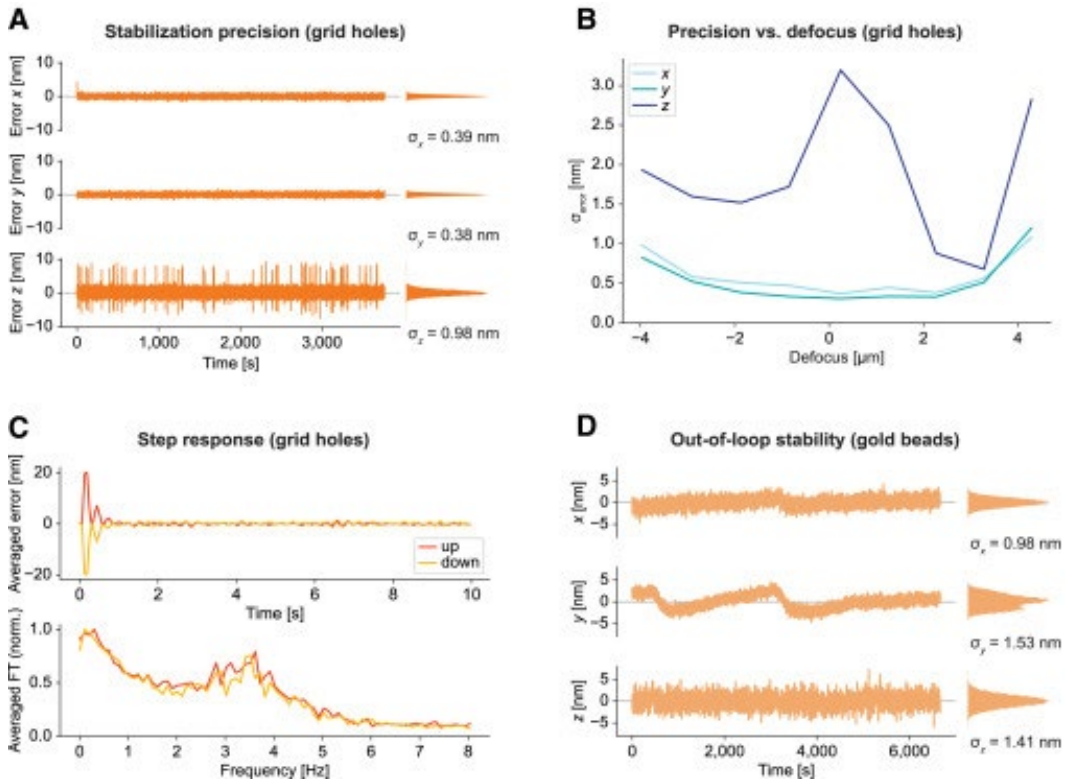

Figure A.2: Performance characterization. (A) Representative measurement of the in-loop stability, as derived from error signals, of the active stabilization unit on holey carbon grids. The measurement was acquired at a slight positive defocus (sample shifted toward objective) with an air objective with 0.75 NA. Histograms of the respective error curves are displayed to their right together with standard deviation σ. Along the optical axis, there were occasional spikes, which may be related to vibrations associated with the fan of the camera. (B) Precision of the active stabilization for different defocus positions using the same sample as in (A). The focus position was determined by eye as the position where the structure appeared sharpest. The sample was then moved manually in steps of 1 µm along z, and the stabilization was engaged at each position. Each curve shows the standard deviation of the error signals (σ_{error}) of measurements of ~200-s duration. (C) Step response of the active sample stabilization. Dynamic response of the system tested by applying offsets to the stage position in steps of ±20 nm every 10 s. Curves shown here represent averages of 10 steps in each direction along the x axis. Raw data as well as corresponding measurements for the other axes are shown in Fig. S4. (D) Position of an individual gold bead on a coverslip over time, imaged in the microscopy path. In the stabilization path, a set of gold beads in a different ROI was used for stabilizing sample position. Residual drifts included relative drifts of the microscopy vs. stabilization path of the microscope.

The following is a pseudocode implementation of the key elements of the stabilization workflow as depicted in Fig. 1 *B*.

A.4.2.1 Acquisition of reference stacks

Stage positions for reference stacks for each axis are specified by the stack range and step size. For the *z* axis, frames are transformed into a 1D array (flattened) and pixel intensity values sorted before appending to the reference stack. For the other axes, raw images are appended to the stack.

```
for each axis:
   for each specified stage position:
    move stage to new stage position
    acquire frame
    normalize frame
    if axis is z axis:
        convert frame to 1D array of pixel intensity values
        sort array
        append sorted array to reference stack
    else:
        append frame to reference stack.
```

A.4.2.2 Displacement estimation in x and y directions

Cross-correlation between images a and b is calculated as follows, with the number of pixels in each row $n$row and in each column $n$col:

$$\mathrm{CC}(a,b) = \sum_{i=0}^{n_{\mathrm{row}}-1} \sum_{j=0}^{n_{\mathrm{col}}-1} a_{i,j} b_{i,j}$$

```
for each entry in reference stack:
   calculate cross-correlation (current frame, reference
   stack entry)
   append to correlation curve
scale correlation curve to range [0,1]
fit Gaussian to scaled correlation curve
displacement = center position of Gaussian.
```

A.4.2.3 Displacement estimation z direction

Mean squared error (MSE) between 1D arrays a and b of length n are calculated as follows:

$$\mathrm{MSE}(a,b) = \frac{1}{n} \sum_{i=0}^{n-1} (a_i - b_i)^2$$

```
normalize frame
convert frame to 1D array of pixel intensity values
sort array
for each entry in reference stack:
  calculate MSE(current array, reference stack entry)
  append to MSE curve
invert MSE curve by multiplication with -1
scale inverted MSE curve to range [0,1]
fit Gaussian to scaled MSE curve
displacement = center position of Gaussian.
```

A.4.3 Sample preparation, data acquisition, and analysis

A.4.3.1 Performance characterization

For the performance measurements on electron microscopy grids, we used a clipped holey carbon 2/2 200 mesh copper grid (N1-C16nCu20-01, Quantifoil Micro Tools, Großlöbichau, Germany; 2-μm hole diameter with 2-μm distances between holes) attached to a microscopy slide with parafilm. For the out-of-loop measurements on gold beads, we used a commercial

alignment sample with 150-nm beads fixed on a coverslip (Abberior, Göttingen, Germany). Data analysis was mainly performed via custom Python scripts.

For out-of-loop measurements (Figs. 1 *D* and 2 *C*), we stabilized the sample position using a set of gold beads and additionally detected gold beads in a different region on the sCMOS camera of the widefield-microscopy path with the cylindrical lens unit in place, acquiring 20,000 frames at ~3-Hz frame rate with 50-ms exposure time. Here, we employed the Fit3Dcspline software package (27) to localize gold beads in 3D using experimental PSFs. To generate the experimental PSF model, we used three *z* stacks of beads acquired in different regions on the same coverslip with the cylindrical lens unit in place. Each stack spanned a range of ±700 nm at a step size of 20 nm. For display purposes, only every fifth datapoint is plotted in Fig. 1 *D*.

A.4.3.2 SMLM of nuclear pores

For fixing gold beads on coverslips, we adapted a protocol described by Balzarotti et al. (11). Before seeding the cells, #1.5H coverslips (18 mm round, 0117580, Paul Marienfeld, Lauda-Königshofen, Germany) were cleaned with Hellmanex III (Z805939, Merck, Darmstadt, Germany; 2% in Milli-Q water; sonicated 2 × 15 min, then washed with Milli-Q water), dried with nitrogen gas, and coated with 0.01% poly-L lysine (P4707, Merck). Subsequently, they were washed 3 × 2 min in Milli-Q water, and dried with nitrogen gas before incubation with 150-nm gold beads (A11-150-CIT-DIH-1-50, Nanopartz, Loveland, Colorado, US) for 10 min that had been diluted 1:5 in Milli-Q water and sonicated for 10 min. The coverslips were then washed 3 × 2 min in phosphate-buffered saline. Finally, they were placed in new, sterile 12-well plates and sterilized with UV in a cell-culture hood for 1 h before seeding cells.

We used U-2 OS cells stably expressing a Nup96-GFP fusion protein (U-2 OS-CRISPR-NUP96-mEGFP clone no.195, 300174, CLS Cell Lines Service, Eppelheim, Germany) from Thevathasan et al. (28) and followed their protocol for nanobody staining against GFP (28,29). In brief, we prefixed the U-2 OS cells for 30 s in transport buffer (TRB: 20 mM HEPES pH 7.5 (H3375, Merck), 110 mM potassium acetate (4986.1, Carl Roth), 1 mM EGTA (E3889, Merck), 250 mM sucrose (84097, Merck) in Milli-Q water) supplemented with 2.5% (w/v) formaldehyde (prepared from stock F8775, Merck), then washed with TRB 2 × 5 min, and permeabilized with TRB supplemented with 25 μg/mL digitonin (D141, Merck) for 8 min on ice. We washed the samples 2 × 5 min with TBA buffer (1% w/v bovine serum albumin (A1391, AppliChem, Darmstadt, Germany) added to TRB), and stained them with FluoTag-X4 anti-GFP nanobodies conjugated to Alexa Fluor 647 dyes (N0304-AF647-L, NanoTag Biotechnologies, Göttingen, Germany) diluted 1:250 in TBA. Cells were washed in TBA 2 × 5 min, then again fixed in TBA supplemented with 2.5% formaldehyde for 10 min and washed again in TBA 2 × 5 min. Subsequently, 0.4% (v/v) Triton (X100, Merck) in phosphate-buffered saline was applied for 3 min to permeabilize the nuclear envelope. The samples were washed in phosphate-buffered saline 2 × 5 min before performing another round of nanobody staining the same way as the first time. Finally, the samples were washed 3 × 10 min in phosphate-buffered saline and mounted in dSTORM buffer (500 mM TRIS (T1503, Merck), 10 mM NaCl (S7653, Merck), 10% (w/v) glucose (G8270, Merck), 0.4 mg/mL glucose oxidase (G2133, Merck), 64 μg/mL catalase (C30, Merck) in phosphate-buffered saline) on cavity slides (1320002, Marienfeld). Immediately after mounting, the coverslips were sealed with twinsil extra-hart (Picodent, Wipperfürth, Germany).

For every dSTORM measurement (Fig. 3), we acquired 20,000 frames at ~6.7-Hz frame rate with 50-ms exposure time. Our field of view was a circle with a diameter of roughly

60 μm, limited by the aperture of the focusing lens in front of the camera. Typically, measurements contained 2–4 nuclei within the field of view.

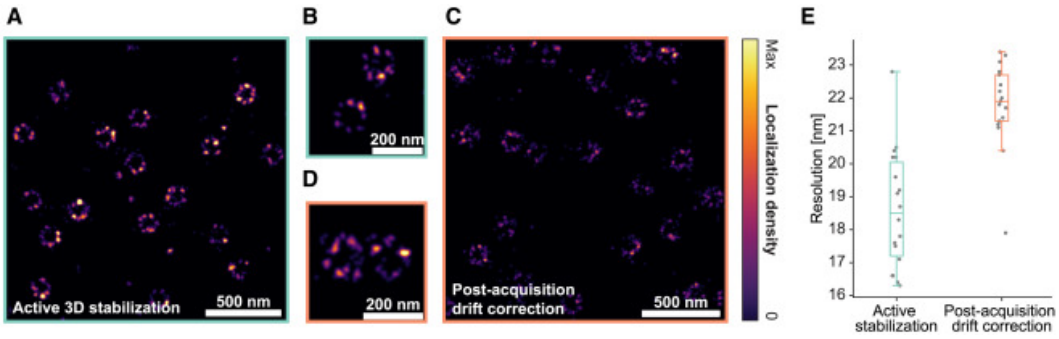

Figure A.3: Active stabilization for dSTORM imaging of nuclear pores. (A and B) Two ROIs at different zoom factors of a dSTORM reconstruction of nuclear pores with active stabilization engaged, showing the ring-like arrangement of the subunits. Observed variability between individual pores includes biological factors and imperfections in labeling. (C and D) Analogous measurement from different cells on the same coverslip without active stabilization, using RCC-based drift correction after acquisition. See Fig. S5 for additional imaging data. (E) Resolution of reconstructions with active 3D stabilization or post-acquisition drift correction displayed as boxplots (lower whisker: lowest data point within 1.5× interquartile range below first quartile, first quartile, median, third quartile, upper whisker: highest data point within 1.5× interquartile range above third quartile). Datapoints represent individual ROIs recorded across two individual measurements for each of the two conditions on the same coverslip. See section materials and methods for details on resolution measurements.

We performed localization using the Picasso software package (version 0.6.8) (30). For the two experiments for which active stabilization was disabled, we corrected drifts after acquisition in Picasso using RCC. For one of the datasets, the frame segmentation parameter was set to 200 frames and for the other we used three rounds of RCC with a frame segmentation of 1000 frames.

We exported the localizations to PALMsiever (version 1.0.1) (31) and used the FIRE plugin of the package to calculate the resolution of different ROIs in our SMLM-reconstructions. FIRE is an approach for estimating the resolution of super-resolution microscopy data based on the concept of Fourier ring correlation (32).

For the resolution measurements (Fig. 3 *E*), we selected different nonoverlapping ROIs across the field of view. Every ROI spanned 4.096 × 4.096 μm^2 at a pixel size of 1 nm. We chose the ROIs such that they contained only single-molecule blinking events, and no continuously emitting bright clusters.

A.4.3.3 Cryo-confocal imaging

We applied 3 μL of sonicated 100-nm Yellow-Green beads (F8803, Thermo Fisher Scientific, Waltham, Massachusetts, US) diluted 1:200 in Milli-Q water to holey carbon 2/2 200 mesh copper grids (Quantifoil Micro Tools) and vitrified them using a GP2 plunge-freezing device (Leica Microsystems) with 3-s blotting time. The grids were stored at liquid-nitrogen temperature until imaging.

We mounted the grid on the Linkam cryo-stage operated at liquid-nitrogen temperature, and first acquired a low-magnification overview image using a 4× objective with a field of view spanning roughly 1.5 mm (half the grid diameter). This image was used to select areas for subsequent high-magnification light-microscopy acquisition.

To prevent condensation of humidity from the environment on the front lens of the high-magnification air objective (working distance 4.7 mm), we heated it with a resistive foil heater

attached to the side of the objective. We applied a constant current of 300 mA to the heater, which resulted in a heating power of 1.8 W applied to the objective body. The current was chosen such that the objective temperature remained approximately at room temperature throughout the operation with our open cryo-stage.

We positioned the sample while observing it in widefield mode because of the higher imaging speed and larger field of view. Since grids typically exhibit bending, the focus was set to an intermediate position where the field of view contained beads that were slightly above and below the focal plane and we opened the pinhole to detect a larger number of beads. Subsequently, we engaged the active stabilization, switched to point-scanning mode, and acquired 40 scans with approximately 34 and 26 nm pixel size (along *x* and *y*) and subsequently another 40 scans without stabilization.

Our confocal setup exhibited distortions due to the delayed response of our scan mirror. We corrected for such distortions using Fiji's BigWarp plugin (33). Using a thin-plate spline transformation, we registered the first confocal scan via landmarks to a widefield image of the same region as largely distortion-free reference and applied the same transformation to all confocal scans. To increase the precision of landmark placings, we placed them at the center position of the beads extracted by Fiji's ThunderSTORM plugin (34). Beads that were not visible throughout the experiment because they drifted out of the field of view were manually excluded from the data displayed in Fig. 4 *A* and *B*.

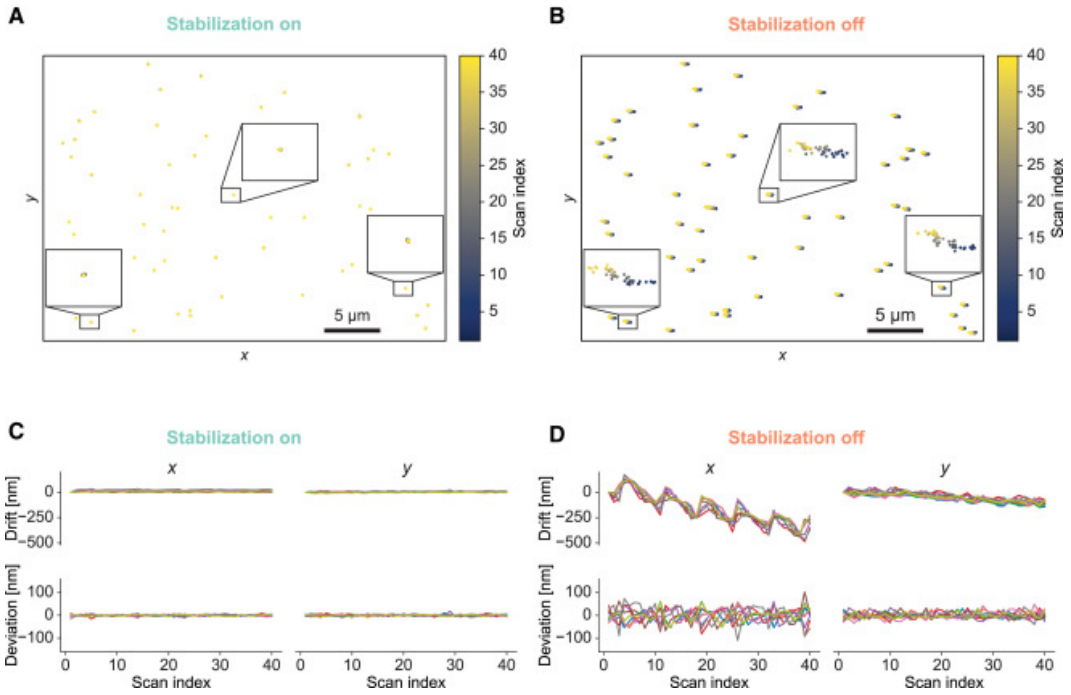

Figure A.4: Cryo-confocal imaging. (A and B) Tracking position of fluorescent beads at cryogenic temperature over 40 confocal scans with sample stabilization engaged (A) or switched off (B), with beads embedded in vitreous ice after plunge-freezing. Insets: 10-fold enlarged views of trajectories of manually selected beads. Tracks differed from each other, reflecting drifts within individual scans, as beads were stably embedded in the vitreous ice. (C and D) Top row: drifts of nine manually selected beads as a function of scan index from the same datasets as (A) and (B), respectively. Bottom row: deviations of bead positions relative to the mean position of the selected beads for every scan. Display ranges of corresponding panels in (C) and (D) were identical to facilitate comparison of the associated spatial scales with and without stabilization.

To show the deviation of different beads across scans (bottom row in Fig. 4 *C* and *D*), we manually selected beads across the field of view. First, the localization traces were subtracted by the mean position over all scans to center them on 0. All points of the centered traces were then subtracted by the mean position of all selected beads in the respective scans to obtain deviations occurring during scans.

A.5 Results

A.5.1 Concept and implementation

We designed our sample stabilization scheme with the aim of providing nanoscale active stabilization in all three spatial dimensions while posing minimal requirements in terms of specific hardware and modifications to the sample preparation. Sample position at the time point of engagement of the stabilization unit was defined as the setpoint for position stabilization, whereas displacement of measured position from this setpoint constituted the error signal. Error signals for stabilizing lateral (*xy*) position were derived from image cross-correlation, whereas analysis of intensity distributions yielded the error signal for stabilizing axial (*z*) position, both with respect to reference stacks recorded directly before engaging the stabilization. This allowed us to estimate displacements using the information encoded in all pixels within a ROI rather than relying on peak fitting of individual fiducial beads.

We implemented our scheme by adding a standard widefield imaging path (Fig. 1 *A*; see section materials and methods; Fig. S1 for additional details) to a homebuilt microscope. Using separate imaging paths for stabilization and microscopy measurements allowed for simultaneously acquiring biological data and stabilizing sample position without mutually interfering with performance. To avoid interfering with fluorescence data acquisition, we chose near-infrared illumination with detection of back-scattered light on a camera in the sample stabilization path. Feedback for the sample stabilization acted on a 3D piezo stage to which the sample was mounted.

The experimental workflow (Fig. 1 *B*) started by acquiring a reference stack for every axis, which we then used for displacement estimation in the subsequent closed-loop operation (i.e., continuously measuring displacements and correcting them). For estimating the lateral displacements at a given time, we acquired a frame and calculated the cross-correlation to all images in the reference stacks for *x* and *y* axes after intensity normalization. This resulted in a correlation curve for each axis whose peak position reflected the current sample position (Fig. S3 *A*). We extracted displacements by fitting a Gaussian function.

The same procedure worked in principle also for estimating displacements along the optical axis. However, the performance strongly depended on the measurement setup. For example, when using an air objective with NA of 0.75, the axial precision was typically around 20 nm (standard deviation), which was insufficient for high-performance super-resolution imaging. Inducing astigmatism in the detection path with a cylindrical lens improved this figure but led to strong crosstalk to the other axes.

We therefore devised a refined approach for stabilization along the *z* axis, avoiding the use of astigmatism: we observed that the shape of the distribution of pixel intensity values of individual frames continuously changed with *z* position of the sample (Figs. 1 *C* and S3 *B*). For every iteration of the feedback loop, we thus calculated the mean squared error (MSE) of the normalized, intensity-sorted pixel intensity values between the current frame and every plane in the reference stack along the *z* axis. The resulting curve of MSEs exhibited a convex shape with the minimum indicating the axial position. After normalization and inversion (Fig. S3 *A*,

bottom), we determined the position of the resulting peak by fitting a Gaussian function in the same manner as for the lateral directions.

For active feedback, we used a proportional-integral control algorithm, moving the piezo sample stage position. As expected, this proved to be more robust than pure proportional feedback, for example when changing samples or objectives. We also added a small portion of second-order integrator, i.e., integration of the summed error, which proved advantageous in presence of strong drifts, arising, e.g., from temperature fluctuations.

The active stabilization strongly suppressed drifts (Fig. 1 *D*). When measured as mean standard deviation across four gold beads, while stabilizing on a different set of beads, drift reduction was by a factor of 50, 46, and 210 in *x*, *y*, and *z*, with measured residual drifts comparable to the localization uncertainty. Fig. 1 *E* shows how our active stabilization counteracted sample drifts over roughly 9 h. Fluctuations of the laboratory temperature during the measurement led to particularly strong drifts, but the residual displacement of the sample, as derived from the calibrated error signals, remained at the setpoint with nanometer-scale accuracy with deviations being attributed largely to noise associated with estimating displacements.

A.5.2 Performance characterization

We characterized the performance of our sample stabilization scheme on two diverse target structures, holey carbon films and sparse gold beads, to demonstrate the flexibility of the scheme. We used holey carbon films to evaluate the attainable stabilization precision, its dependence on defocus of the sample, and to characterize the dynamic step response. Gold beads allowed for an additional validation of stabilization performance by 3D localization of the sparse peaks in the separate microscopy path.

We used the standard deviation of the error signal as a measure of the stabilization precision ("in-loop stability"). For this evaluation, we stabilized the 3D-position of an empty holey carbon grid. These are commonly used as sample carriers in electron microscopy and cryo-fluorescence imaging. We imaged the sample using the stabilization path with an air objective (NA 0.75) with long working distance (4.7 mm), as required by our cryo-stage. At room temperature, we typically obtained in-loop stability better than 1 nm in the lateral plane and around 1–4 nm along the optical axis (Fig. 2 *A* and *B*). We stabilized the sample for a full day without observable degradation of precision.

Next, we examined the relationship between the stabilization precision and the defocus of the sample. The lateral precision did not change notably within 2 μm of the focal plane, and it slightly deteriorated at larger defocus (Fig. 2 *B*). By contrast, axial precision was highest at a defocus of 2–3 μm. The optimum defocus value and magnitude of improvement over in-focus stabilization changed for different sample types and objectives. We attribute the improved axial stability at moderate defocus to more pronounced variation of the intensity distributions with axial position (Fig. S3). This observation is not unique to our implementation, with several previous schemes for 3D active sample stabilization requiring defocus (7,20,22,35).

To test the dynamic behavior of our implementation, we applied step-wise offsets of 20 nm in alternating directions to the stage position every 10 s and observed the step response of the sample stabilization. Fig. 2 *C* shows the averaged error signals of 10 of these steps in either direction along the *x* axis. The raw data as well as data for the other axes are displayed in Fig. S4. The stabilization brings the error back to the noise floor within less than a second. To quantify the temporal response, we fitted the average step responses to an exponentially

decaying function with a temporal offset t_0 and decay constant τ: $f(t) = \alpha e^{-(t-t_0)/\tau}$. The results were similar for all axes with $t_0 \approx 100$ ms and $\tau \approx 150$ ms when the sample was operated at a defocus. In focus, the step response along *z* was slower. The Fourier transform of the curves in Fig. 2 *C* showed a peak at approximately 3.5 Hz followed by a monotonous decline, which represents timescales that are fast compared to those associated with pronounced microscope drifts, typically observed over multiple seconds to hours, with drift rates depending on a number of parameters. For example, for the measurement shown in Fig. 1 *D* without active stabilization, within 10 s, the sample moved by a median distance of 7 nm (across all time points; maximum drift observed within 10 s was 31 nm). The sampling rate was around 16 Hz. In this particular measurement, we optimized feedback parameters for speed, whereas we usually used parameters optimized for high static stabilization precision for other measurements.

In practice, biological data are acquired in imaging paths that are only partially identical with the stabilization path. Accordingly, it is informative to evaluate the stabilization performance in a separate microscopy path, i.e., in an "out-of-loop" measurement. This also accounts for potential confounding factors (e.g., relative drifts between optical paths or crosstalk between axes in error signal generation). We performed such out-of-loop measurements on gold beads immobilized on a coverslip. We used gold beads in one region of the coverslip for stabilization, detecting them on the camera of the sample stabilization path. In parallel, we localized a different set of beads in 3D on the camera of the widefield-microscopy path, using back-scattered light from a different light source.

Out-of-loop stability was on the nanometer scale (Fig. 2 *D*) over the 1 h 51 min measurement time, with σ_x = 1.03 ± 0.09 nm, σ_y = 1.58 ± 0.03 nm, and σ_z = 1.51 ± 0.13 nm (mean ± standard deviation of position of five beads manually selected from different regions within a measurement). These numbers are limited by the finite precision of the localization of the beads in the microscopy path. Averaging localizations over subsequent frames improved the values to σ_x = 0.60 ± 0.06 nm, σ_y = 1.43 ± 0.02 nm, and σ_z = 0.39 ± 0.11 nm (same beads as before, averaging the localizations of 400 subsequent frames). However, some nanometer-scale fluctuations on the timescale of tens of minutes (Fig. 2 *D*) remained that were not apparent in the error signals of the respective axes. We attribute them to drifts in the part of the microscopy path that was distinct from the stabilization path, likely related to temperature fluctuations in the laboratory. Along the optical axis, the standard deviation of the out-of-loop error (without averaging over subsequent frames) was about three times smaller than the in-loop error of the displacement estimation. This is presumably related to the fact that the value derived from the error signal ("in-loop measurement") is dominated by noise in the error signal, which is averaged out by the integrator in the proportional-integral feedback, showing that, in certain scenarios, drifts can be compensated on finer length scales than suggested by the in-loop measurement.

A.5.3 Example applications

We set out to test our scheme in two different application scenarios: SMLM at room temperature and confocal imaging at cryogenic temperatures. We selected those modalities with very different characteristics to demonstrate the versatility of the approach.

A.5.3.1 Sample stabilization in SMLM

To test our stabilization scheme in a typical high-performance imaging scenario, we chose a well-established SMLM modality, dSTORM (36), and applied it to a biological structure that

is commonly used as test and reference structure in super-resolution imaging. We labeled a protein of the nuclear pore complex (NPC), which is a multi-protein assembly that regulates traffic between the nucleus and cytoplasm. NPCs comprise a central pore and a ring-like arrangement of proteins with eightfold symmetry. The Nup96 protein is located in the ring region of NPCs and is a popular target for super-resolution imaging (28). This protein is arranged in two stacked circles with an average diameter of ~108 nm (37).

We used a previously established cell line expressing a Nup96-mEGFP fusion protein at endogenous levels (28). For dSTORM imaging, we labeled mEGFP with Alexa Fluor 647-conjugated nanobodies, thus minimizing displacement between the fluorophore and the biological target. For active 3D sample stabilization, we collected light scattered by gold beads attached to the coverslip carrying the cells.

We performed imaging of NPCs on the facet of the nuclear envelope facing the coverslip, which was well within the axial operating range of our sample stabilization scheme, and acquired dSTORM measurements in the widefield-microscopy path of the setup with the active stabilization switched either on or off. We then compared the quality of the reconstructed NPC structures with active 3D stabilization engaged to reconstructions with commonly employed correction of lateral drifts after acquisition using RCC without active stabilization. We found the eightfold symmetric structure of NPCs to be more faithfully represented with active stabilization (Fig. 3). To corroborate this observation independently of potential bias from manually selecting NPCs and to average out variability of NPCs, we also determined spatial resolution in both acquisition modes with a Fourier ring correlation-based method (see section materials and methods). The results confirmed that active stabilization indeed gave better resolution than post-acquisition correction (18.6 ± 1.8 nm vs. 21.8 ± 1.3 nm, respectively, mean ± standard deviation; $p = 2.2 \times 10^{-5}$ with Mann-Whitney U-test using 18 and 17 ROIs from two measurements each on the same coverslip with active stabilization on/off).

Note that, in the case where active sample stabilization was disengaged, the *z* position was not actively stabilized either, which is different from common SMLM acquisitions. However, we gave the setup ample time to reach thermal equilibrium after turning on equipment and chose a day with high temperature stability in the laboratory, such that axial drifts were observed to be small. Although the width of the detected single-molecule peaks increased slightly during the 50 min of acquisition (Fig. S5 *C*), this effect was small (6% variability of the median peak width across all frames).

A.5.3.2 Active stabilization for confocal imaging at cryogenic conditions

We chose cryo-confocal imaging as a second test case for our stabilization scheme. Imaging at cryogenic temperatures has the potential to reveal biological structures in a near-natively preserved state, but cryo-stages suitable for cryo-light microscopy often exhibit strong drifts at various timescales relevant for biological imaging, from sub-seconds to hours. Such drifts impact image quality and correlation accuracy to other imaging modalities. For example, sample drifts during an acquisition in a point-scanning approach, such as confocal imaging, may distort images in ways that cannot be corrected afterward. Therefore, we reasoned that our 3D sample stabilization could enhance data collection in this application.

To evaluate our active sample stabilization scheme at cryogenic temperatures, we plunge-froze fluorescent beads on holey carbon grids. We used the structure of the holey carbon grid in scattering mode as reference for our 3D sample stabilization. In parallel, confocal imaging under cryo-conditions was performed on fluorescent beads using the confocal-microscopy

path, with a commercial open cryo-stage to maintain the sample below the devitrification temperature. We acquired series of confocal scans with and without engaging the stabilization. When comparing the peak positions of individual beads across different scans (Fig. 4), active sample stabilization strongly mitigated both overall drifts (by a factor of 21, as evaluated from the root-mean-square values of the respective tracks) and apparent relative movements of different beads with respect to each other (by a factor of 6). Assuming that positions of fluorescent beads were fixed by the rigid structure of the vitreous ice, relative movements of beads in the imaging data can be attributed to drifts occurring during individual confocal scans. Since our sample stabilization operated on timescales much faster than confocal scanning, it effectively fixed sample position during acquisition of individual confocal imaging frames.

A.6 Discussion

We have developed an image-based scheme for nanometer-scale active sample stabilization in 3D with moderate overhead for hardware or sample preparation. We showed that our approach improved data quality on the example of two distinct imaging applications. Our algorithm does not require sparse fiducial beads to be added to the sample and is expected to enable active sample stabilization for a wider range of scenarios than the showcase applications shown here. Our scheme is equally compatible with sparse peaks from fiducial beads, which we demonstrated using dSTORM imaging of nuclear pores. We showed that, compared to post-acquisition drift correction, active stabilization resulted in an improved resolution of single-molecule reconstructions. Moreover, we showed that active sample stabilization mitigated distortions in cryo-confocal imaging. Artifacts stemming from drifts that occur during scans cannot be easily corrected *post hoc*. Therefore, active stabilization can be crucial for reaching the full potential of cryogenic imaging and its correlation to other imaging modalities.

We chose to utilize the light scattered back from the sample because this configuration delivers a stable signal over extended time periods without being affected by photo-bleaching. Moreover, it does not require high illumination intensity, thus minimizing perturbations to the sample, for example when operating at cryogenic temperatures or investigating living specimens. Our stabilization unit comprised a widefield imaging path to maintain simplicity of the implementation and minimize the length of the optical path, as drifts within the module itself would lead to erroneous repositioning of the sample. Still, for some applications, other contrast modalities that offer increased capacity for background suppression, such as second-harmonic imaging, Raman, or fluorescence, may be preferred for generating the error signal. Also, phase contrast, differential interference contrast, and interferometric scattering microscopy (38) may be applicable. Implementing our stabilization scheme with such techniques would presumably extend the range of suitable features for stabilization to structures that produce insufficient amplitude contrast in our current configuration.

Our scheme provides a useful combination of moderate experimental complexity and modest computational requirements. Future adaptations may refine the algorithms for drift estimation to find procedures that are optimal in a mathematical sense. Alternatively, deep learning may be explored for extracting displacements. Further performance improvements may be possible if accepting additional overhead, such as use of an amplitude filter in a Fourier plane for background suppression (23). The microscopy path of the setup may also be actively stabilized in addition to the sample position, e.g., by using a laser beam directed at

the microscopy camera as "optical fiducial" (20,35). Overall, the design choices for a specific application will likely depend on factors such as the type of structures used for stabilization, required precision, and NA of the objective lens.

We observed that temperature stability of the camera chip was important for accurate stabilization. Therefore, we chose an actively cooled CCD camera available in the lab for our implementation. However, vibrations from the camera fan might have produced the occasional spikes along *z* visible in Fig. 2 *A*. Using an industry-grade, passively cooled CMOS camera, we obtained even higher in-loop stabilization precision than reported in Fig. 2 with the same sample and objective (Fig. S2) after allowing for sufficient time for temperature equilibration. We reason that a camera with low readout noise and fanless active chip cooling available at moderate price would be a particularly useful choice for our scheme.

The feedback rate of our implementation depended on the acquisition parameters, including the size of the ROI and the number of frames per reference stack. By tuning these, we reached around 16-Hz update rate. At this point, the readout speed of the camera became the limiting factor. Although the response time was sufficient for the applications we tested, the sampling rate of the feedback can, in principle, be further increased by using a faster camera (suitable models can run at frame rates of hundreds of Hz). Similarly, calculations for displacement estimation could potentially be sped up by performing them on a graphics processing unit (GPU) instead of a standard instrument-control PC, but eventually the response time of the sample stage will limit the usable feedback rate.

The choice of the feedback type may be affected by the desired characteristics in terms of speed and accuracy as well as the dynamics of the stabilization unit, including piezo stage, camera, PC interface, and computation. For example, although others have noted that pure proportional feedback allowed for high-performance drift correction (20,21,25), we opted for standard proportional/integral feedback with a small component of second-order integrator, which yielded satisfactory performance and did not require precise calibration of measured displacements.

Although our implementation is based on a homebuilt setup, it should be straightforward to integrate our scheme in commercial microscopes, such as utilizing commonly available side or back ports on commercial microscope stands. Various imaging modalities besides the applications shown here, such as quantitative time-lapse or multiplexed imaging, may benefit from effective, straightforward active stabilization. The ease of implementation of our scheme may reduce the entry barrier for users who may otherwise not consider active sample stabilization for their application. With its simplicity and flexibility (e.g., compatibility with high- and low-NA objective lenses), while allowing nanoscale stabilization in 3D, we expect our stabilization scheme to be of value in a range of applications.

A.7 Data and code availability

Computer code for sample stabilization is available at https://github.com/danzllab/samplestabilization under the GNU Affero General Public License (GNU AGPLv3) (Copyright: Institute of Science and Technology Austria). Computer code for spatial light modulator control is available at https://github.com/danzllab/SLMcontrol under the GNU Affero General Public License (GNU AGPLv3) license (Copyright: Institute of Science and Technology Austria).

A.8 Acknowledgments

We acknowledge expert support by ISTA's scientific service units, including the Miba Machine Shop, the Electron Microscopy Facility, and the Lab Support Facility. This work has been made possible in part by CZI grant DAF2021-234754 and grant DOI: https://doi.org/10.37921/812628ebpcwg from the Chan Zuckerberg Initiative DAF, an advised fund of Silicon Valley Community Foundation (funder DOI: https://doi.org/10.13039/100014989) (F.K.M.S. and J.G.D.). We further gratefully acknowledge funding by the following sources: Austrian Science Fund (FWF) grant DK W1232 (M.R.T. and J.G.D.); Austrian Academy of Sciences DOC fellowship 26137 (M.R.T.); Marie Skłodowska-Curie Actions Fellowship GA no. 665385 under the EU Horizon 2020 program (J.L.); ISTA postdoctoral fellowship IST fellow (A.W.); and Human Frontier Science Program postdoctoral fellowship LT000557/2018 (W.J.).

A.9 Author contributions

J.V. and J.G.D. designed the study, interpreted data, and wrote the manuscript. J.V. performed experiments and analysis. N.S. programmed the sample stabilization user interface. C.K., N.A.D., M.G.J., B.Z., and M.R.T. performed sample preparation. M.Š. programmed hardware control. W.J. programmed control software for spatial light modulator. A.W. supported hardware design. J.L. advised on computational implementation. F.K.M.S. advised on cryo-sample preparation and imaging.

A.10 Declaration of interests

The authors declare no competing interests.

A.11 Supporting material

PDF (1.28 MB)
Document S1. Figures S1–S5
PDF (4.54 MB)
Document S2. Article plus supporting material

A.12 References

1. Huang, B. · Bates, M. · Zhuang, X.
Super resolution fluorescence microscopy
Annu. Rev. Biochem. 2009; **78**:993-1016
2. Sahl, S.J. · Hell, S.W. · Jakobs, S.
Fluorescence nanoscopy in cell biology
Nat. Rev. Mol. Cell Biol. 2017; **18**:685-701
3. Lelek, M. · Gyparaki, M.T. ...
Single-molecule localization microscopy
Nat. Rev. Methods Primers. 2021; **1**:39
4. Power, R.M. · Tschanz, A. ...
Build and operation of a custom 3D, multicolor, single-molecule localization microscope
Nat. Protoc. 2024; **19**:2467-2525
5. Wang, Y. · Schnitzbauer, J. ...
Localization events-based sample drift correction for localization microscopy with redundant cross-correlation algorithm
Opt. Express. 2014; **22**:15982-15991

6. Balinovic, A. · Albrecht, D. · Endesfelder, U.
Spectrally red-shifted fluorescent fiducial markers for optimal drift correction in localization microscopy
J. Phys. D Appl. Phys. 2019; **52**, 204002
7. Lee, S.H. · Baday, M. ...
Using fixed fiduciary markers for stage drift correction
Opt. Express. 2012; **20**:12177-12183
8. Li, K. · Ni, J. ...
Motion screening of fiducial marker for improved localization precision and resolution in SMLM
Opt. Express. 2023; **31**:26764-26776
9. Reinhardt, S.C.M. · Masullo, L.A. ...
Ångström-resolution fluorescence microscopy
Nature. 2023; **617**:711-716
10. Weisenburger, S. · Boening, D. ...
Cryogenic optical localization provides 3D protein structure data with Angstrom resolution
Nat. Methods. 2017; **14**:141-144
11. Balzarotti, F. · Eilers, Y. ...
Nanometer resolution imaging and tracking of fluorescent molecules with minimal photon fluxes
Science. 2017; **355**:606-612
12. Weber, M. · Leutenegger, M. ...
MINSTED fluorescence localization and nanoscopy
Nat. Photonics. 2021; **15**:361-366
13. Weber, M. · von der Emde, H. ...
MINSTED nanoscopy enters the Ångström localization range
Nat. Biotechnol. 2023; **41**:569-576
14. Hell, S.W. · Wichmann, J.
Breaking the diffraction resolution limit by stimulated emission: stimulated-emission-depletion fluorescence microscopy
Opt. Lett. 1994; **19**:780-782
15. Klar, T.A. · Jakobs, S. ...
Fluorescence microscopy with diffraction resolution barrier broken by stimulated emission
Proc. Natl. Acad. Sci. 2000; **97**:8206-8210
16. Hauser, M. · Wojcik, M. ...
Correlative Super-Resolution Microscopy: New Dimensions and New Opportunities
Chem. Rev. 2017; **117**:7428-7456
17. Dahlberg, P.D. · Moerner, W.E.
Cryogenic Super-Resolution Fluorescence and Electron Microscopy Correlated at the Nanoscale
Annu. Rev. Phys. Chem. 2021; **72**:253-278
18. Carter, A.R. · King, G.M. ...
Stabilization of an optical microscope to 0.1 nm in three dimensions
Appl. Opt. 2007; **46**:421-427
19. Coelho, S. · Baek, J. ...

3D active stabilization for single-molecule imaging
Nat. Protoc. 2021; **16**:497-515
20. Coelho, S. · Baek, J. ...
Ultraprecise single-molecule localization microscopy enables in situ distance measurements in intact cells
Sci. Adv. 2020; **6**, eaay8271
21. Grover, G. · Mohrman, W. · Piestun, R.
Real-time adaptive drift correction for super-resolution localization microscopy
Opt. Express. 2015; **23**:23887-23898
22. Koo, P.K. · Setru, S.U. · Mochrie, S.G.J.
Active drift stabilization in three dimensions via image cross-correlation
Rev. Sci. Instrum. 2013; **84**, 103705
23. Schmidt, R. · Weihs, T. ...
MINFLUX nanometer-scale 3D imaging and microsecond-range tracking on a common fluorescence microscope
Nat. Commun. 2021; **12**:1478
24. Dai, M. · Jungmann, R. · Yin, P.
Optical imaging of individual biomolecules in densely packed clusters
Nat. Nanotechnol. 2016; **11**:798-807
25. McGorty, R. · Kamiyama, D. · Huang, B.
Active microscope stabilization in three dimensions using image correlation
Opt. Nanoscopy. 2013; **2**:3
26. Shang, M. · Zhou, Z. ...
High-precision 3D drift correction with differential phase contrast images
Opt. Express. 2021; **29**:34641-34655
27. Li, Y. · Mund, M. ...
Real-time 3D single-molecule localization using experimental point spread functions
Nat. Methods. 2018; **15**:367-369
28. Thevathasan, J.V. · Kahnwald, M. ...
Nuclear pores as versatile reference standards for quantitative superresolution microscopy
Nat. Methods. 2019; **16**:1045-1053
29. Pleiner, T. · Bates, M. ...
Nanobodies: site-specific labeling for super-resolution imaging, rapid epitope-mapping and native protein complex isolation
Elife. 2015; **4**, e11349
30. Schnitzbauer, J. · Strauss, M.T. ...
Super-resolution microscopy with DNA-PAINT
Nat. Protoc. 2017; **12**:1198-1228
31. Pengo, T. · Holden, S.J. · Manley, S.
PALMsiever: a tool to turn raw data into results for single-molecule localization microscopy
Bioinformatics. 2015; **31**:797-798
32. Nieuwenhuizen, R.P.J. · Lidke, K.A. ...
Measuring image resolution in optical nanoscopy
Nat. Methods. 2013; **10**:557-562
33. Bogovic, J.A. · Hanslovsky, P. · Saalfeld, S. ...

Robust registration of calcium images by learned contrast synthesis
2016 IEEE 13th International Symposium on Biomedical Imaging (ISBI) (2016 IEEE 13th International Symposium on Biomedical Imaging (ISBI)
IEEE, 2016; 1123-1126
34. Ovesný, M. · Křížek, P. ...
ThunderSTORM: a comprehensive ImageJ plug-in for PALM and STORM data analysis and super-resolution imaging
Bioinformatics. 2014; **30**:2389-2390
35. Pertsinidis, A. · Zhang, Y. · Chu, S.
Subnanometre single-molecule localization, registration and distance measurements
Nature. 2010; **466**:647-651
36. Heilemann, M. · Van De Linde, S. ...
Subdiffraction-resolution fluorescence imaging with conventional fluorescent probes
Angew. Chem. Int. Ed. 2008; **47**:6172-6176
37. Wang, W. · Jakobi, A. ...
Particle fusion of super-resolution data reveals the unit structure of Nup96 in Nuclear Pore Complex
Sci. Rep. 2023; **13**, 13327
38. Kukura, P. · Ewers, H. ...
High-speed nanoscopic tracking of the position and orientation of a single virus
Nat. Methods. 2009; **6**:923-927

B. Setup details

This section contains further technical details regarding the microscope setup described in Section 2.1. The beam paths are depicted in detail and all relevant components and setup parameters are listed.

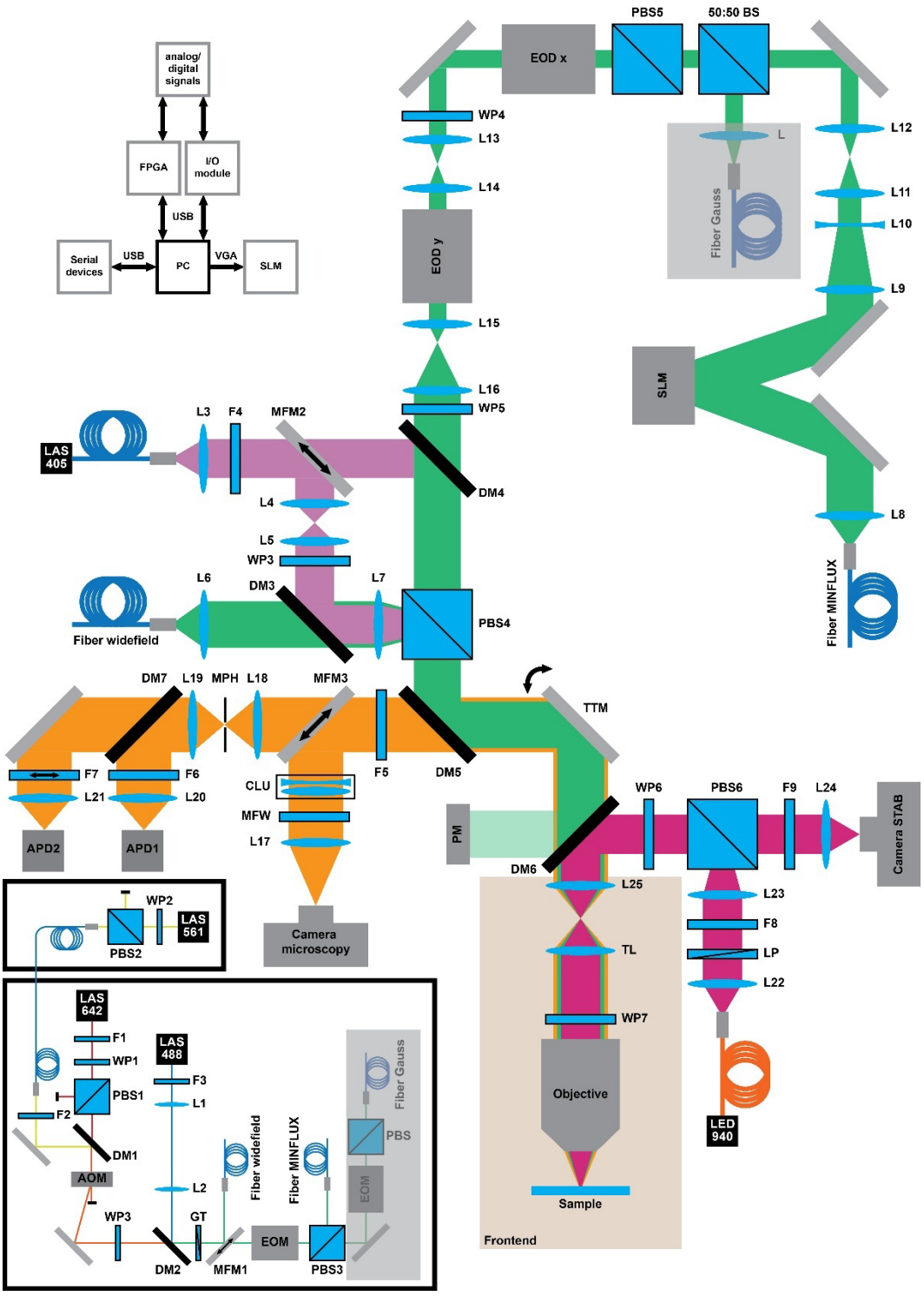

Figure B.1: Complete optical path of the microscope. Excitation light is shown in green, activation light in violet, emission in orange and light for the active stabilization module in magenta. The laser module, which is constructed on a different breadboard, is depicted within by black boxes. Parts shaded in grey were planned but

not fully implemented. For simplicity, lenses on the input side of the optical fibers and some mirrors are omitted, and the WF illumination is depicted only up to PBS4. The frontend (brown background) is show in greater detail in Figure B.2.

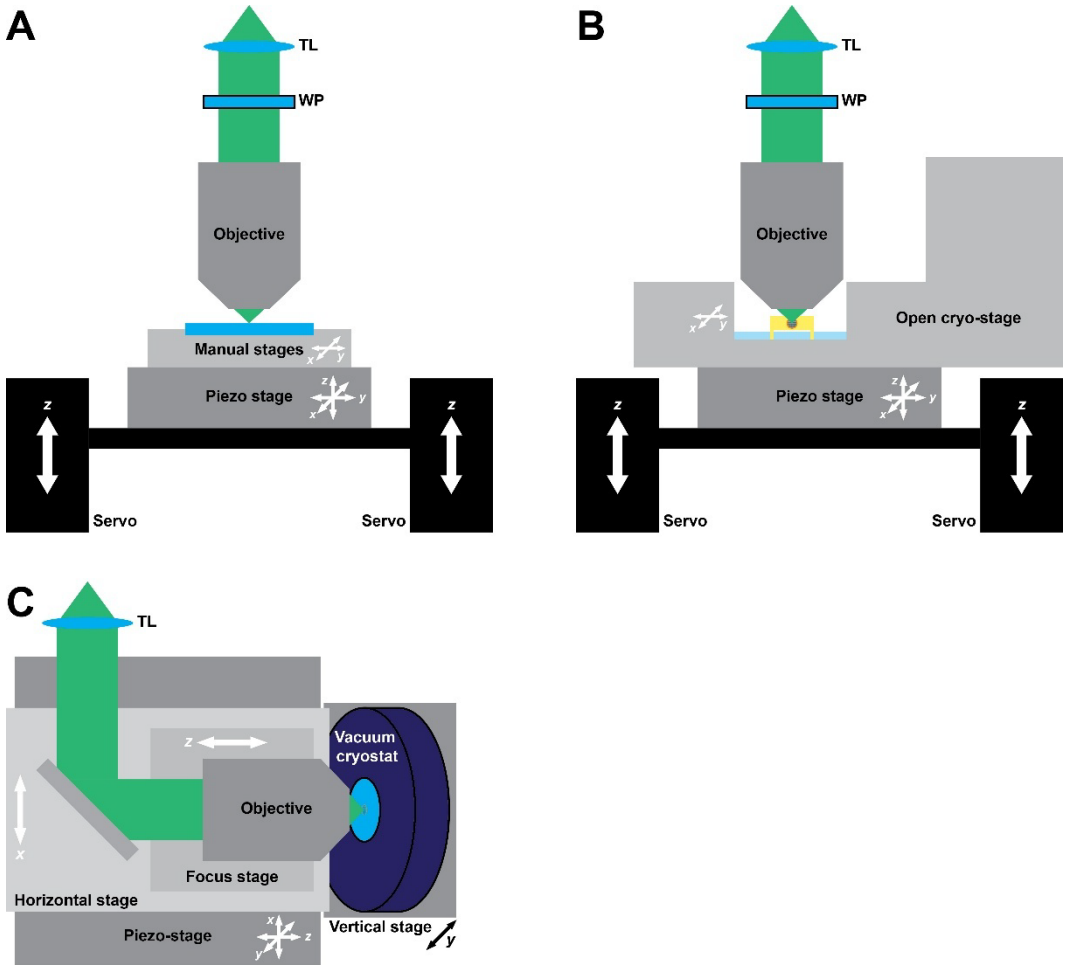

Figure B.2: Microscope frontend configurations. For simplicity, only the excitation light is shown. A and B are shown from the side, and C from a top-down point of view. ***A:*** *Configuration for RT imaging. The sample slide is mounted on manual stages for coarse lateral positioning. Servo stepper motors focus the sample with roughly 1 µm precision. A 3D piezo stage is used for fine positioning and active stabilization.* ***B:*** *Configuration for imaging with open cryo-stages. The frontend is analogous to* ***A*** *except that the sample is mounted in a cryo-stage where it is cooled by liquid nitrogen. The cryo-stage depicted here comes with integrated lateral sample positioning functionality (as is the case for the Linkam cryo-stage), such that it can be attached directly to the piezo stage. Otherwise, stages for coarse positioning would have to be attached to the cryo-stage (as is the case for the Leica cryo-stage).* ***C:*** *Configuration for imaging with the vacuum cryostat. Samples are coarsely positioned using three manual translation stages, one of them moving the cryostat vertically. The other two move a platform comprising a mirror and the objective, and adjust focus of the objective, respectively. They are mounted on a 3D piezo stage for fine positioning. A λ/4 waveplate will likely be added in the same position as shown in A and B.*

B.1 Components

B.1.1 Laser module

LAS642: 642 nm excitation laser, 2W (2RU-VFL-P-2000-642-B1R, MPB Communications, Pointe-Claire, Canada).

LAS561: 561 nm excitation laser, 1 W (Jive1000, Cobolt AB, Solna, Sweden).

LAS488: 488 nm excitation laser, 200 mW (IBEAM-SMART-488-S-HP, Toptica Photonics, Gräfelfing, Germany).

AOM: acousto-optical modulator (MT110-A1,5-VIS, AA Opto-Electronic, Orsay, France).

EOM: electro-optical modulator (LM0202 VIS KD*P, Qioptiq Photonics GmbH & Co. KG, Feldkirchen, Germany; driven by DIV20, Qioptiq).

MFM1: motorized flip mirror (MFF101/M, Thorlabs, Newton, New Jersey, USA).

F1: 640/10 nm bandpass filter (ZET640/10x, Chroma Technology, Bellows Falls, Vermont, USA).

F2: 561/4 nm bandpass filter (FF01-561/4-25, Semrock, Rochester, New York, USA).

F3: 488/10 nm bandpass filter (ZET488/10x, Chroma).

DM1: 568 nm longpass dichroic mirror (F48-573, AHF Analysentechnik AG, Tübingen, Germany).

DM2: 488 nm longpass dichroic mirror (ZT488rdc-UF3, Chroma).

WP1: zero-order λ/2 waveplate, 633 nm (WPH10M-633, Thorlabs).

WP2: zero-order λ/2 waveplate, 488 nm (WPH10M-488, Thorlabs).

PBS1: polarizing beamsplitter cube, 633 nm design wavelength (PBS25-633, Thorlabs).

PBS2: polarizing beamsplitter cube, 420-680 nm coating (PBS251, Thorlabs).

PBS3: polarizing beamsplitter cube, 400-700 nm coating (PTW 0.15, Bernhard Halle Nachfl., Berlin, Germany).

L1: achromatic doublet, f = 50 mm (AC254-050-A-ML, Thorlabs).

L2: achromatic doublet, f = 60 mm (AC254-060-A-ML, Thorlabs).

GT: Glan-Thompson polarizer (GTH10M-A, Thorlabs).

Fiber MINFLUX: polarization-maintaining single-mode fiber for confocal excitation (QPMJ-3AF3S-405/650-3/125-3AS-5-1-WK, Oz Optics, Ottawa, Canada).

Fiber widefield: polarization-maintaining single-mode fiber for WF excitation (PMC-E-400RGB-2.8-NA011-3-APC.EC/OPC.EC-400-P, Schäfter + Kirchhoff, Hamburg, Germany).

B.1.2 Widefield

LAS405: 405 nm activation laser, 100 mW (IBEAM-SMART-405-S, Toptica).

Camera microscopy: sCMOS camera for WF detection (Orca Fusion BT, Hamamatsu Photonics, Hamamatsu, Japan).

MFM2: motorized flip mirror (MFF101/M, Thorlabs).

MFM3: motorized flip mirror (MFF101/M, Thorlabs).

F4: 405/10 nm bandpass filter (FF01-405/10-25, Semrock).

F5: 842 nm shortpass filter (FF01-842/SP-25, Semrock).

MFW: motorized filter wheel (FW102C, Thorlabs) loaded with 446/60 nm bandpass filter (FF02-447/60-25, Semrock) at position 1, 525/50 nm bandpass filter (FF03-525/50-25, Semrock) at position 2, 595/40 nm bandpass filter (ET595/40m, Chroma) at position 3, 706/95 nm (ET706/95m, Chroma) + 698/70 nm (FF01-698/70-25, Semrock) bandpass filters at position 4.

DM4: 405 nm longpass dichroic mirror (F48-403, AHF).

DM5: 405/488/561/640 multipass dichroic mirror (ZT405/488/561/640rpcv2-UF3, Chroma).

WP3: zero-order λ/2 waveplate, 405 nm (WPH10M-405, Thorlabs).

PBS4: polarizing beamsplitter cube, 400-700 nm coating (PTW 0.25, Bernhard Halle).

L3: achromatic doublet, f = 25 mm (AC127-025-A-ML, Thorlabs).

L4: aspheric lens, f = 5.5 mm (C105TMD-A, Thorlabs).

L5: achromatic doublet, f = 50 mm (AC254-050-A-ML, Thorlabs).

L6: achromatic doublet, f = 100 mm (AC254-100-A-ML, Thorlabs).

L7: achromatic doublet, f = 150 mm (AC254-150-A-ML, Thorlabs).

L17: achromatic doublet, f = 80 mm (AC254-080-A-ML, Thorlabs).

CLU (removable; only for 3D localization): cylindrical lens unit comprising cylindrical lenses with f = 1000 mm (LJ1516RM-A, Thorlabs) and f = -1000 mm (LK1002RM-A, Thorlabs) rotated against each other.

B.1.3 MINFLUX

SLM: spatial light modulator (X13268-01, Hamamatsu).

EOD x, y: electro-optical deflectors (M-311A, ConOptics Inc., Danbury, Connecticut, USA) driven by pairs of high-voltage amplifiers (WMA-300, Falco Systems BV, Hilversum, Netherlands) in a differential configuration.

TTM: tip/tilt mirror (PSH25-2 SG OEM, Piezosystem Jena, Jena, Germany; driven by d-Drive, Piezosystem Jena).

APD1: avalanche photodiode-based single-photon counting module (COUNT-100B, Laser Components, Munich, Germany).

APD2: avalanche photodiode-based single-photon counting module (SPCM-AQRH-44-BR1, Excelitas Inc., Waltham, Massachusetts, USA).

MPH: motorized pinhole wheel (MPH16, Thorlabs).

F6: 525/50 nm bandpass filter (FF03-525/50-25, Semrock).

F7: 706/95 nm bandpass filter (ET706/95m, Chroma), mounted on motorized flip mount (MFF101/M, Thorlabs).

DM7: 560 nm longpass dichroic mirror (F48-558, AHF).

WP4: achromatic λ/2 waveplate, 400-800 nm (AHWP10M-600, Thorlabs).

WP5: achromatic λ/2 waveplate, 350-850 nm (AHWP10M-580, Thorlabs).

50:50 BS: non-polarizing beamsplitter cube, 400-700 nm (BS013, Thorlabs).

PBS5: polarizing beamsplitter cube, 420-680 nm coating (PBS251, Thorlabs).

L8: achromatic doublet, f = 40 mm (AC254-040-A-ML, Thorlabs).

L9: achromatic doublet, f = 400 mm (AC254-400-A-ML, Thorlabs).

L10: achromatic doublet, f = -50 mm (ACN127-050-A, Thorlabs).

L11: achromatic doublet, f = 150 mm (AC254-150-A-ML, Thorlabs).

L12: achromatic doublet, f = 200 mm (AC254-200-A-ML, Thorlabs).

L13: achromatic doublet, f = 150 mm (AC254-150-A-ML, Thorlabs).

L14: achromatic doublet, f = 150 mm (AC254-150-A-ML, Thorlabs).

L15: achromatic doublet, f = 150 mm (AC254-150-A-ML, Thorlabs).

L16: achromatic doublet, f = 400 mm (AC254-400-A-ML, Thorlabs).

L18: achromatic doublet, f = 100 mm (AC254-100-A-ML, Thorlabs).

L19: achromatic doublet, f = 75 mm (AC254-075-A-ML, Thorlabs).

L20: achromatic doublet, f = 30 mm (AC254-030-A-ML, Thorlabs).

L21: achromatic doublet, f = 40 mm (AC254-40-A-ML, Thorlabs).

B.1.4 Active stabilization module

LED940: 940 nm fiber-coupled LED (M940F3, Thorlabs; driven by LEDD1B, Thorlabs), coupled into multimode fiber with 0.22 NA (M47L01, Thorlabs).

Camera STAB: stabilization camera, CCD (Luca R, Andor, Belfast, UK) or CMOS (U3-3060SE-M-GL Rev.1.2, IDS Imaging Development Systems, Obersulm, Germany).

F8: 950/57 nm bandpass filter (ET950/57x, Chroma).

F9: 808 nm longpass filter (BLP01-808R-25, Semrock).

DM6: 770 nm shortpass dichroic mirror (T770spxr-1380-UF3, Chroma).

LP: linear polarizer (LPNIRE100-B, Thorlabs) on rotational mount.

WP6: zero-order λ/4 waveplate, 915 nm (WPQ10M-915, Thorlabs).

PBS6: polarizing beamsplitter cube, 700-1100 nm coating (PBS252, Thorlabs).

L22: achromatic doublet, f = 50 mm (AC254-050-B-ML, Thorlabs).

L23: achromatic doublet, f = 150 mm (AC254-150-B-ML, Thorlabs).

L24: achromatic doublet, f = 80 mm (AC254-080-B-ML, Thorlabs).

B.1.5 Frontend (compare Figure B.2)

Open cryo-stage: microscopy stage cooled by liquid nitrogen (CMS196V3, Linkam Scientific Instruments Ltd., Redhill, UK or 11501272, Leica Microsystems, Wetzlar, Germany)

Vacuum cryostat: continuous flow cryostat for microscopy (ST-500, Lake Shore Cryostronics Inc., Westerwille, Ohio, USA).

Piezo stage: 3D piezo stage (P-733.3DD, Physik Instrumente (PI) GmbH & Co. KG, Karlsruhe, Germany; driven by E-727, Physik Instrumente).

Servos: two translation stages (DRV250, Thorlabs; driven by BSC202, Thorlabs); connected by 12.7 mm thick breadboard.

Vertical stage: high-load vertical linear stage (M-MVN120, Newport Corporation, Irvine, California, USA).

Horizontal stage: linear translation stage (PT1B/M, Thorlabs).

Focus stage: z-axis translation mount (SM1ZA, Thorlabs).

Objective: air objective (HC PL FLUOTAR L 100x/0.75, Leica), air objective with correction collar (LD PN 63x/0.75 Korr, Zeiss) or oil objective (UPLXAPO100XO, Olympus, Tokyo, Japan).

TL: tube lens (11090148038000, Leica or 425308-0000-000, Carl Zeiss AG, Oberkochen, Germany).

WP7: achromatic λ/4 waveplate, 350-850 nm (AQWP10M-580, Thorlabs).

L25: achromatic doublet, f = 75 mm (AC254-75-AB-ML, Thorlabs).

B.1.6 Vacuum cryostat and accessories (compare Figure 3.4)

Vacuum cryostat: continuous flow cryostat for microscopy (ST-500, Lake Shore Cryotronics Inc., Westerwille, Ohio, USA).

Temperature controller: Model 335 (Lake Shore).

Dewar: liquid nitrogen dewar including pressure-building system (TP100, Air Liquide, Paris, France; borrowed from ISTA's Electron Microscopy Facility).

TP: turbomolecular pump (HiPace 80 Neo, Pfeiffer Vacuum + Fab Solutions, Aßlar, Germany).

PVP: pre-vacuum pump (HiScroll 6, Pfeiffer).

VP: dry-scroll vacuum pump (IDP3, Agilent Technologies Inc., Santa Clara, California, USA; borrowed from ISTA's Electron Microscopy Facility).

VG1: Vacuum gauge for cryostat (PKR360, Pfeiffer).

VG2: Vacuum gauge for airlock (TPR270, Pfeiffer).

GV: gate valve (SG0150MVQF, Kurt J. Lesker Company GmbH, Dresden, Germany).

LC: loading chamber (Aquilos I loading chamber, Thermo Fisher; borrowed from ISTA's Electron Microscopy Facility).

TR: transfer rod (Aquilos I transfer rod, Thermo Fisher; borrowed from ISTA's Electron Microscopy Facility).

Vacuum pump controllers: OmniControl 001 (Pfeiffer; connected to PVP, TP and VG2), OmniControl 200 (connected to VG1); Aquilos I pump controller (Thermo Fisher Scientific, Waltham, Massachusetts, US; connected to VP; borrowed from ISTA's Electron Microscopy Facility).

B.1.7 Data acquisition

PC: microscope control PC (C9Z390-CG, Super Micro Computer., San Jose, California, USA).

FPGA: field-programmable gate array (USB-7856R, National Instruments, Austin, Texas, USA).

I/O module: analog/digital input-output module for data acquisition (USB-3114, Meilhaus, Alling, Germany).

B.1.8 Other

Optical table: passively damped optical table (M-ST-UT2-56-8, Newport).

Microscopy breadboard: precision-grade optical breadboard (M-PG-35-4, Newport).

Mirrors: silver mirrors (PF10-03-P01, Thorlabs) between objective and TTM, dielectric mirrors for near-infrared light in the active stabilization module (BB1-E03, Thorlabs), dielectric mirrors for visible light (BB1-E02, Thorlabs) elsewhere.

PM: calibrated silicon-photodiode power meter (PM16-130, Thorlabs).

B.2 Software

In the tables below, software packages written by colleagues in the Danzl lab, and those provided by manufacturers are listed. Device names correspond to the abbreviations introduced in the previous section. DCS was written by Marek Šuplata (except for parts of the active stabilization module written by me). samplestabilization was written by Nikolai Semenov (except for the core workflow containing the algorithm written by me). CryoCode was written by Nikolai Semenov. SLMcontrol was written by Wiebke Jahr. minflux-analysis was written by me.

NAME	DESCRIPTION	DEVICES	LOCATION
DCS	Hardware control for confocal, MINFLUX, active stabilization.	FPGA (EODs, TTM, APDs), I/O module (AOM), Piezo stage, Camera STAB, Servos	https://git.ista.ac.at/marek.suplata/dcs2 (private)
samplestabilization	GUI for active sample stabilization.	Camera STAB, Piezo stage	https://github.com/danzllab/samplestabilization
CryoCode	Logging of cryostat temperature.	Cryostat temperature controller	Microscope control PC (private)
SLMcontrol	Adjusting phase pattern on SLM.	SLM	https://github.com/danzllab/SLMcontrol
minflux-analysis	Software tool for MINFLUX localization, visualization, analysis	n.a.	https://github.com/danzllab/minflux-analysis

Table B.1: Custom software packages.

DEVICE	NAME	VERSION	COMMENTS
LAS642	GUI-VFL	4.2.1	
LAS405, 488	TOPAS iBeam smart	1.3.0.106	Use shortcuts TOPAS1/2 to connect to both lasers simultaneously.
MFM	Thorlabs Kinesis	1.14.36	For testing, after DCS connection stopped working.
MFW	Thorlabs FWxC	5.0.0	
CAMERA MICROSCOPY	Hokawo	3.0.pf8	Crashed occasionally.
MPH	Thorlabs MPH16	4.0	After DCS connection stopped working.
CAMERA STAB	IDS peak Cockpit	1.7.0.0	For testing.
LINKAM STAGE	Link	1.2.14.37	
PIEZO STAGE	PIMikroMove	2.29.0.1	For testing and calibration.
PM	Thorlabs Optical Power Monitor	4.1.4204.742	
I/O MODULE	DAQami	4.2.1f1	For testing.

Table B.2: Software packages provided by device manufacturers.

B.3 Cryostat operation

1. **Fill dewar:** Get at least 30 l of liquid nitrogen, depending on intended experiment duration.
2. **Insert cryogen transfer line:** Since the transfer line is inserted into the dewar vertically from the top, this step requires two people to lift it high enough. Only the back of the laboratory, where no pipes or cables obstruct the ceiling, provides enough vertical space. Make sure that the o-ring sealing the dewar leg of the transfer line is tight, to be able to build up pressure. Then, place the dewar on the scale to monitor its fill level and attach the short leg of the transfer line to the cryostat. Make sure the transfer line is inserted all the way into the cryostat to prevent spilling of liquid nitrogen.

3. **Evacuate cryostat:** First, switch on the pre-vacuum pump (BKP on pump controller). Once pressure has reached on the order of 10^{-2}-10^{-1} mbar, switch the on turbomolecular pump (TMP on pump controller). Wait until the pressure has dropped to ca. 10^{-5} mbar. This may take multiple hours, so it is often practical to pump down overnight.

   Attention! The turbomolecular pump requires a pre-vacuum below 22 mbar (for N_2) during operation. Sudden pressure shocks, e.g., due to accidental opening of valves connected to the pump, as well as mechanical shocks to the pump itself, will damage the device and lead to risk of injury.
4. **Cool down:** Generate pressure in the liquid nitrogen dewar by opening the respective valve. I found 3-4 psi to be an adequate range. Bear in mind that it will take over an hour for the pressure to reach a constant value. Turn the dewar leg of transfer line clockwise to enable flow of liquid nitrogen to dewar. Switch on the temperature controller and start the CryoCode software[78] to start logging temperature. For the first minutes, the temperature typically decreases quite slowly, then the cooldown accelerates. If faster cooldown is wanted, increase flow of liquid nitrogen. Once the temperature has reached ca. 80 K, greatly reduce the flow, such that the nitrogen evaporates fully at the heat exchanger inside the cryostat, i.e., no liquid droplets are observed at the outlet port[79]. Once this is attained, switch the heater range on the temperature controller to high and choose an adequate setpoint (I mostly used 80 K). If the temperature displays sudden jumps > 50 mK, reduce the nitrogen flow further[80].
5. **Load sample:** Cool the mantle and the interior of the loading station with liquid nitrogen until the boil-off decreases drastically. Place the shuttle in the receptacle piece[81] (make sure it is rotated downwards) using the transfer rod. Cover the loading station with the pertinent lid for sample handling, with a removable inner part (not the lid containing a flange adapter for the transfer rod). Place an autogrid box in the designated recess and open it. Load autogrids to the shuttle: First, make sure that the screws on the shuttle are tightened enough to move the clamps to the side, then place the grids in position on the shuttle, and finally loosen the screws just enough to fix the grids in place. Gently touch the side of the grids with tweezers to confirm that they are fastened on the shuttle, and rotate the shuttle by 180°. In order to minimize ice contamination, it is recommended to wear a face-shield throughout the entire procedure, lift the lid only as much as is required to insert the instruments, and perform loading as quickly as possible. Place the lid with the flange adapter for the transfer rod on the chamber. Place the transfer rod on the flange[82], pick up the shuttle and pull it up into the vacuum chamber of the transfer rod. Close the slider on the lid and evacuate the transfer rod immediately. After ca. 30 s, close the vacuum-tight lid

[78] The software is currently located on the Desktop of the microscope control PC. Start logging by executing “main.py” in a pertinent Python environment. So far, it was tested exclusively using Visual Studio Code.

[79] Liquid droplets often arrive in irregular bursts, so make sure to monitor the outlet for at least one minute.

[80] On some days, it was hard to find a flow level that provided sufficient nitrogen to cool the sample, but at the same time did not lead to temperature spikes associated with liquid bursts. Further investigation is necessary to find the source of this behavior.

[81] When the chamber was cooled down with the shuttle already in place, the shuttle sometimes got stuck to the holder. Therefore, it is recommended to insert it after cooldown.

[82] To reduce the risk of ice contamination, I personally like to pump the air out of the transfer rod before opening the slider in the lid and picking up the shuttle. However, I never checked if this is really necessary.

of the transfer rod, vent, and attach it to the airlock. Evacuate the airlock while checking the vacuum gauge connected to the airlock (VG1). Once the pressure has dropped below ~1-2 mbar, close the ball valve[83] and open the gate valve connected to the cryostat. Vent, and remove the transfer rod. Insert the shuttle into the cryostat, retract the transfer rod, and close the gate valve. Warm up the loading station[84].

Attention! To reduce the risk of vacuum breaks in the cryostat which may destroy the turbomolecular pump, fasten the transfer rod via two nylon-tipped screws to the airlock.

6. **Imaging:** As depicted in Figure B.2C, the cryostat is mounted on a vertical translation stage. Horizontal translation and focusing is performed by moving the objective. Use these three translation stages to position the objective on one of the grids in the shuttle, identify an ROI and start imaging. The correction collar on the objective should be set to 0.5 mm to compensate for the refractive index of the cryostat viewing window.
7. **Unload sample:** Evacuate the airlock with the transfer rod attached (the lid of the transfer rod being open), open the gate valve and retrieve the shuttle to the vacuum chamber of the transfer rod. Close the lid of the transfer rod as well as the gate valve, vent, and move the transfer rod to the pre-cooled loading station. Unload the samples analogous to loading.
8. **Warm up cryostat:** Once imaging is finished, warm the cryostat back up. It is recommended to leave the vacuum pumps running until the interior has reached room temperature to avoid ice condensation on the viewing window[85] and inside the cryostat. Turn off the flow of liquid nitrogen at the transfer line and de-pressurize the dewar by closing the valve for pressure building and opening the gas exhaust valve. Select a setpoint slightly above RT (I mostly used 305 K) at the temperature controller to increase the warm-up speed. Mind that due to the positioning of the temperature sensor, the controller shows that the setpoint is reached before all parts have actually warmed up to RT. Hence, leave the heater running for ~1 h after the setpoint has been reached.
9. **Break vacuum:** After all parts have reached RT, switch off the turbomolecular pump. It will take roughly half an hour to wind down. Once the pump controller shows that the rotation speed has reached 0 Hz, switch off the backing pump and vent the cryostat with RT nitrogen gas.
10. **(optional) Remove transfer line:** This step is only necessary if the dewar is (close to) empty, i.e., if the weight displayed on the scale falls below a value that is still to be experimentally determined. Analogous to the insertion of the transfer line, this is best performed by two people in a part of the laboratory where the ceiling is unobstructed.

    Attention! The transfer line may still be cold, so wear a cryo-protective glove while handling it.

[83] Closing the valve sometimes reduced increased the pressure in the airlock, potentially due to air inside the valve. To prevent this, it is recommended to open and close it 1-2 times while the airlock is pumping down.

[84] To reduce the risk of ice contamination, always warm up the loading station between loading and unloading of samples. Warming can be sped up by disposing the remaining liquid nitrogen, and purging the base with warm nitrogen gas.

[85] Due to convective heat transfer, the cold trap in proximity to the viewing window can cool it enough for a layer of ice to form on the outside of the cryostat.

C. Sample preparation protocols

C.1 DNA-origami nanorulers (Figure 2.4A)

Protocol adapted from Gattaquant:
https://www.gattaquant.com/files/information_for_immobilization.pdf

1. Clean #1.5H coverslips (18 mm round, 0117580, Paul Marienfeld, Lauda-Königshofen, Germany) in 70 % ethanol bath overnight or longer.
2. Wash coverslip with 700 µl 1xPBS for 3x2 min.
3. Incubate with 700 µl of bovine serum albumin-biotin (29130, Thermo Fisher; 1 mg/ml in 1xPBS) for 5 min.
4. Wash for 3x2 min with 700 µl of 1xPBS.
5. Incubate with 700 µl of AF488-streptavidin (S32354, Thermo Fisher; 20 ug/ml in 1xPBS) for 5 min.
6. Wash 3x with 10 mM $MgCl_2$ (M2670, Merck) in 1xPBS (referred to as immobilization buffer 1xIB).
7. Incubate with 150 nm gold beads for 5 min (A11-150-CIT-DIH-1-50, Nanopartz, Loveland, Colorado, US; diluted 1:3 (200 µl in 400 µl of 1xIB), vortexed, then sonicated for 10 min).
8. Wash again for 3x2min in 1xIB.
9. Incubate with DNA-origami nanorulers for 5 min (GATTA-PAINT 40R, Gattaquant GmbH, Gräfelfing, Germany; 2 µl (after spinning down) in 100 µl of 1xIB, pipetted directly on coverslip after removing 1xIB from previous step thoroughly).
10. Wash 3x with 700 µl of 1xIB.
11. Prepare buffer B+ following Schnitzbauer *et al.* (2017): 5 mM of Tris-HCl (T1503, Merck), 10 mM of $MgCl_2$ (M2670, Merck), 1 mM of EDTA (E6635, Merck) and 0.05 % (vol/vol) of Tween-20 (BP337-500, Thermo Fisher; using 1 % pre-dilution in 1xPBS) in 1xPBS.
12. Dilute imager solution provided by Gattaquant (after spinning down) 1:1000 in buffer B+ to a concentration of imager strands of 5 nM.
13. Mount coverslip on cavity slides in PAINT imaging buffer and seal with twinsil extra-hart (Picodent, Wipperfürth, Germany).

C.2 Nup96 anti-GFP nanobody staining of cells (Figure 2.4B)

Stainings were performed closely following the protocol of Thevathasan *et al.* (2019), who followed Pleiner *et al.* (2015). Our protocol is described in the Materials and methods section of (Vorlaufer et al., 2025), see Section A.4.3.2 of this thesis. In the version reproduced here, formatting was adapted.

1. Wash #1.5H coverslips (18 mm round, 0117580, Paul Marienfeld, Lauda-Königshofen, Germany) with Hellmanex III (Z805939, Merck, Darmstadt, Germany; 2% in Milli-Q water; sonicated for 2x15 min, then washed with Milli-Q water).
2. Dry coverslips with nitrogen gas.
3. Coat with 0.01% poly-L lysine (P4707, Merck) for > 10 min.
4. Wash for 3x2 min in Milli-Q water.
5. Dry coverslips with nitrogen gas.
6. Incubate with 150 nm gold beads (A11-150-CIT-DIH-1-50, Nanopartz; diluted 1:5 in milli-Q water, vortexed, sonicated for 10 min) for 10 min.

7. Wash for 3x2 min in 1xPBS.
8. Place coverslips in new, sterile 12-well plates, and sterilized with UV in a cell-culture hood for 1 h before seeding cells.
9. We used U-2 OS cells stably expressing a Nup96-GFP fusion protein (U-2 OS-CRISPR-NUP96-mEGFP clone no.195, 300174, CLS Cell Lines Service, Eppelheim, Germany) from Thevathasan *et al.* (2019) and followed their protocol for nanobody staining against GFP (Pleiner et al., 2015; Thevathasan et al., 2019).
10. Prefix U-2 OS cells (U-2 OS-CRISPR-NUP96-mEGFP clone no.195, 300174, CLS Cell Lines Service, Eppelheim, Germany) for 30 s in transport buffer (TRB: 20 mM HEPES pH 7.5 (H3375, Merck), 110 mM potassium acetate (4986.1, Carl Roth), 1 mM EGTA (E3889, Merck), 250 mM sucrose (84097, Merck) in Milli-Q water) supplemented with 2.5% (w/v) formaldehyde (prepared from stock F8775, Merck).
11. Wash with TRB for 2x5 min.
12. Permeabilize with TRB supplemented with 25 µg/mL digitonin (D141, Merck) for 8 min on ice.
13. Wash for 2x5 min with TBA buffer (1% w/v bovine serum albumin (A1391, AppliChem, Darmstadt, Germany) added to TRB).
14. Stain with FluoTag-X4 anti-GFP nanobodies conjugated to Alexa Fluor 647 dyes (N0304-AF647-L, NanoTag Biotechnologies, Göttingen, Germany) diluted 1:250 in TBA.
15. Wash in TBA for 2x5 min.
16. Fix in TBA supplemented with 2.5% formaldehyde for 10 min.
17. Wash in for TBA 2x5 min.
18. Apply 0.4% (v/v) Triton (X100, Merck) in 1xPBS for 3 min to permeabilize the nuclear envelope.
19. Wash in 1xPBS for 2x5 min.
20. Again, stain with FluoTag-X4 anti-GFP nanobodies conjugated to Alexa Fluor 647 dyes (N0304-AF647-L, NanoTag Biotechnologies, Göttingen, Germany) diluted 1:250 in TBA.
21. Wash for 3x10 min in 1xPBS.
22. Mount coverslip in dSTORM buffer (500 mM TRIS (T1503, Merck), 10 mM NaCl (S7653, Merck), 10% (w/v) glucose (G8270, Merck), 0.4 mg/mL glucose oxidase (G2133, Merck), 64 µg/ml catalase (C30, Merck) in 1xPBS) on cavity slides (1320002, Marienfeld).
23. Seal with twinsil extra-hart (Picodent, Wipperfürth, Germany).

C.3 Phalloidin staining of cells (Figure 2.4C-D; Figure 3.3A, E; Figure 3.8B-E)

Here, I describe our protocol for staining cells with fluorophore-conjugated phalloidin. Specific steps were adapted for different experiments as indicated.

1. Seed cells on #1.5H coverslips (RT-experiments) or glow-discharged, fibronectin-coated EM-grids (cryo-experiments).
2. Wash cells with 1xPBS and fix with 4% PFA (in 1xPBS) for 20 min.
3. Immediately quench for 5 min in 1xPBS supplemented with 100 mM glycine (50046-50G, Merck).
4. Wash in 1xPBS for 3x3 min.
5. Permeabilize cells with 0.1% Triton (X100, Merck) in 1xPBS for 40-60 s.

6. Wash immediately in 1xPBS for 3x3 min.
7. Block in 1% bovine serum albumin (A1391, AppliChem) diluted in 1xPBS (filtered together) for 30 min.
8. Wash in 1xPBS for 2x5 min.
9. If PaX560 is used: Perform following steps using pertinent darkroom-safe red lamps (B09B557MDS, Etone, Dong Guang City, China) for illumination, switch off all other light sources and work in room without windows.
10. Incubate with filtered 1% bovine serum albumin in 1xPBS supplemented with either fluorophore-conjugated phalloidin diluted 1:2000 (all except Figure 3.3A), or fluorophore-conjugated phalloidin + DAPI (32670-5MG-F, Merck) diluted 1:500 (Figure 3.3A), for 1h at RT.
    a. If PaX560 is used: Apply 50 µl of the dilution to parafilm and place the coverslip on the drop inside a custom humified chamber covered by aluminum foil (to protect from light exposure when opening the door).
    b. Fluorophore-conjugated phalloidins used: PaX560-phalloidin (kindly provided by Richard Lincoln), AFP647-phalloidin (A30107, Thermo Fisher), AF488-phalloidin (A12379, Thermo Fisher).
11. Wash coverslips in 1xPBS for 3x5 min.
12. For RT-experiments: Mount coverslip on imaging chamber (Figure 2.4C), or epoxy-sealed cavity slides (Figure 2.4C), using 1xPBS as imaging buffer.
13. For cryo-experiments: Plunge-freeze EM-grids using the GP2 device (Leica Microsystems) with 3-5 s blotting time.

C.4 DNA-origami grids (Figure 2.5)

We prepared the sample closely following the protocol described by Balzarotti *et al.* (2017) in Section 6.6.6 of their Supplementary Information[86].

1. Wash #1.5H coverslips (18 mm square, BB01800180A123MNZ0, Portsmouth, New Hampshire, USA) with Hellmanex III (Z805939, Merck, Darmstadt, Germany; 2% in Milli-Q water; sonicated for 2x15 min, then washed with Milli-Q water).
2. Repeat for microscopy slides (Superfrost Plus, J1800AMNZ, Epredia) but sonicate only once[87].
3. Dry slide and coverslip with nitrogen gas, and form a flow channel with two stripes of double-sided Scotch tape.
4. Incubate with 15 µl of 150 nm gold beads (A11-150-CIT-DIH-1-50, Nanopartz; undiluted, vortexed, sonicated for 10 min) for 5 min.
5. Flush[88] flow channel with 15 µl milli-Q water, dry with nitrogen gas.
6. Incubate with 15 µl of bovine serum albumin-biotin (29130, Thermo Fisher; 2 mg/ml in 1xPBS) for 15 min.
7. Flush flow channel with 400 µl of 1xPBS.

[86] We had previously tried the Gattaquant protocol described in Section C.1, but reconstructions did not reproduce the expected grid-like arrangements.

[87] We were concern that the Superfrost-coating might be affected by washing. Nothing suspicious was noted during experiments, but after ca. 1.5 months, cloudy patches were observed in the milli-Q water storing the slides. No indication of bacterial or fungal contamination was observed by imaging a drop of the solution in brightfield (on the cell culture microscope). For future experiments, using uncoated microscopy slides may be advisable.

[88] When flushing, always place Kimwipe on other end to soak up excess liquid.

8. Incubate with 15 µl of streptavidin (SA101, Merck; 0.5 mg/ml in 1xPBS) for 15 min.
9. Flush flow channel with 400 µl of 1xPBS.
10. Flush flow channel with 200 µl of folding buffer (FB; 1xTAE buffer supplemented with 10 mM $MgCl_2$ (M2670, Merck)).
11. Incubate with 15 µl of DNA-origami structures (GATTA-PAINT Grid 20R, Gattaquant; diluted 1:25 in FB) for 15 min.
12. Flush flow channel with 200 µl of FB.
13. Flush flow channel with 200 µl of imaging buffer (IB), consisting of B+ from Schnitzbauer *et al.* (2017) (5 mM of Tris-HCl (T1503, Merck), 10 mM of $MgCl_2$ (M2670, Merck), 1 mM of EDTA (E6635, Merck) and 0.05 % (vol/vol) of Tween-20 (BP337-500, Thermo Fisher; using 1 % pre-dilution in 1xPBS)), supplemented with 5 nM PAINT imager strands, in 1xTAE buffer
14. Seal flow channel with twinsil extra-hart (Picodent).

C.5 Transient expression of fluorescent proteins in cells (Figure 3.3)

1. Seed rattus norvegicus wildtype embryo fibroblasts [89] (RRID:CVCL_0513; kindly provided by Klemens Rottner (Helmholtz Centre for Infection Research, Braunschweig)) in the morning into 6-well plate to be at a confluence of ~80% in the afternoon for transfection.
2. Leave to settle for 4 h prior to transfection.
3. In 200 µl DMEM for each transfection, mix 3 µl of Lipofectamin Plus reagent (15338100, Thermo Fisher) and 500 ng of the respective plasmid (PAGFP-utrophin: PaGFP-UtrCH, 26738, Addgene, Watertown, Massachusetts, USA; mEmerald-ER3: mEmerald-ER-3, 54082, Addgene).
4. Incubate for 10 min at RT.
5. Add 2.5 µl of Lipofectamin LTX reagent (15338100, Thermo Fisher) and mix.
6. Incubate for 10 min at RT.
7. Mix in droplets to cells and swirl.
8. Incubate at 37 °C and 5% CO_2 overnight.
9. Detach transfected cells with 0.25 % trypsin (25200-056, Thermo Fisher), then seed cells on glow-discharged holey carbon 2/2 200 mesh gold EM-grids (Quantifoil Micro Tools, Großlöbichau, Germany), wait until settled (assess by checking on a stereo-microscope).
10. Plunge-freeze on GP2 device (Leica Microsystems), using 3 s blotting time.

C.6 In vitro *polymerized actin (Figure 3.3)*

1. Let 1.25 µM G-actin (kindly provided by the Loose lab at ISTA[90]) polymerize in 100 µl F-actin buffer (50 mM KCl (60130, Merck), 1 mM $MgCl_2$ (CAS7791-18-6, Merck), 0.5 mM ATP (5122-01, Hypermol EK, Bielefeld, Germany), 1 mM EGTA (E3889, Merck), and 10 mM Imidazole pH 7.5 (56750, Merck)) in an Eppendorf tube at RT for 1h.
2. Add 1.25 µM of PAGFP-utrophin (PaGFP-UtrCH, 26738, Addgene; from 22 µM stock), and incubate on ice for 40 min.

[89] Cultured in Dulbecco's modified Eagle's medium, supplemented with 10% (v/v) fetal bovine serum, 1% (v/v) penicillin–streptomycin, and 1% (v/v) non-essential amino acids (MEM NEAA (100x), Gibco, #11140035).

[90] G-actin is also commercially available: AKL99-A, Cytoskeleton Inc., Denver, Colorado, USA.

3. Split the reaction volume into 2 ultracentrifuge tubes with 50 µl/tube and ultracentrifuge at 100000g at 4 °C using a TLA-100 rotor for 45 min.
4. For each tube, discard the supernatant in both tubes, and resuspend the pellet with 125 µl F-actin buffer supplemented with AFP647-phalloidin (A30107, Thermo Fisher) at dilution 1:1500.
5. Apply 3 µl of solution to glow-discharged holey carbon 2/2 200 mesh copper EM-grids (Quantifoil), discard the rest.
6. Plunge-freeze on GP2 device (Leica Microsystems), using 3 s blotting time.